UCLouvain

epl

École polytechnique de Louvain

Design of a mechanical system for the experimental study of the collapse of a granular column in water at rest – validation and flow measurements using imaging techniques

Authors: **Victor ANCIAUX, Benoît SCHOEPS**
Supervisors: **Miltiadis PAPALEXANDRIS, Sandra SOARES FRAZAO**
Readers: **Benoît HERMAN, Anouk RIFFARD**
Academic year 2022–2023
Master [120] in Mechanical Engineering

Abstract

This thesis focuses on the study of granular media behaviors in water, aiming to contribute to their numerical modeling research. To achieve this, experiments are conducted on a commonly studied configuration known as the collapse of a granular column in water. The purpose of these experiments is to obtain analyzable recordings of the collapse.

The paper is divided into two main parts. The first part focuses on designing a mechanical system specifically made for studying the aforementioned configuration. The limitations of former designs are identified, and new system requirements are established. Through testing, the final design is validated, providing a reliable mechanism for investigating granular collapse.

The second part is dedicated to experiments and starts with a comprehensive description of the experimental setup including its limits and boundaries, providing insights for future research. The laboratory experiments are conducted at the LEMSC in UCLouvain, using a high-speed camera to capture videos. The resulting images are then analyzed using image processing methods with PYTHON and DAVIS 8 software. A theoretical model based on Monsorno *et al* is presented to understand the physical behavior of granular material in two-phase flows. Key parameters influencing the collapse are summarized. A parametric analysis of the collapse is conducted through five different aspect ratios, two types of sand, two initial volume fractions and whether or not the presence of a sand bed downstream. The results yield significant findings regarding the influence of these parameters.

Comparisons are made between the experimental results and numerical simulations based on the proposed model. While there are good agreements in the final shapes of the deposits, differences in the temporal characteristics of the collapse are observed.

The thesis concludes by highlighting the progress made in understanding granular media, while also emphasizing the need for further explorations and comprehension. The complex behavior of granular media still holds many unknowns. This thesis contributed to the existing knowledge by providing a range of experimental recordings that can serve as a foundation for future investigations in the field of granular collapse in water.

This page is intentionally left blank.

Acknowledgements

Voila près d'an que nous travaillons sur ce mémoire. Lorsqu'on y regarde dans sa globalité, de nombreuses personnes nous ont accompagnés. Sans leur aide, rien de tout ceci n'aurait été possible. C'est pourquoi nous tenions à consacrer cette page à toutes les personnes ayant apporté leur aide à la réalisation de ce mémoire, de près ou de loin.

Tout d'abord, nous souhaitions remercier notre promotrice, Madame Sandra Soares Frazão, pour sa disponibilité, ses relectures attentives, ses critiques constructives et surtout sa bienveillance. Nous remercions également notre promoteur, Monsieur Militiadis Papalexandris.

Ensuite, nous remercions grandement Monsieur Benoît Herman pour son aide indispensable dans la réalisation du mécanisme. Son temps précieux et sa capacité à nous pousser continuellement aux limites de nos réflexions ont façonné chaque aspect de celui-ci.

Nous remercions de tout coeur Anouk Riffard pour son soutien, ses relectures et son aide à la compréhension du modèle théorique.

Ce mécanisme n'aurait également jamais pu voir le jour sans l'aide précieuse et la patience des techniciens du CREDEM envers les bons novices que nous étions. Sans les conseils et les compétences techniques de Julien, Vincent, Hervé, Simon, Frank et Arnaud, nous serions peut-être toujours en train de tenter de limer une barre en acier à main.

Nous aimerions également remercier l'équipe du LEMSC et en particulier Pierre

Mertens de Wilmars pour ses nombreux conseils, sa confiance accordée et son temps passé à travailler sur le canal.

Ecrire un mémoire dans une langue qui n'est pas notre langue maternelle était un réel défi, nous remercions fortement Michael Kennedy pour sa relecture et sa correction attentive de l'anglais de notre mémoire.

Nous remercions également Robin Meurice pour ses idées et sa gestion de détails administratifs pour nous procurer le matériel.

Nous n'étions pas les seuls à travailler sur ce canal et partager un espace de travail commun peut s'avérer compliqué. C'est pourquoi nous remercions Guillaume et Brieuc pour avoir rendu cette collaboration agréable et respectueuse. Nous les remercions également pour leur aide dans l'utilisation des sondes BAUMER.

Merci également à Thibault et Thomas pour leur bonne ambiance et encouragements lors des dernières semaines d'intense écriture.

Et finalement, rien de tout ceci n'aurait été possible sans le soutien indéfectible de nos familles respectives durant toutes ces années. C'est pourquoi nous tenions à leur adresser le plus grand de tous les mercis.

Contents

Introduction

> *"One can scoop up poppy seeds with a ladle as easily as if they were water and, when dipping the ladle, the seeds flow in a continuous stream."*[1]
>
> *Lucretius (ca. 98-55 B.C)*

Around two millennia ago, Lucretius, the Roman poet and philosopher, observed and documented an intriguing characteristic of granular media. Situated between liquids and solids, they have special properties that have interested mankind for centuries. From Coulomb to Einstein, passing through Reynolds, many famous scientists have dedicated some of their works to these media. In order to provide a more contemporary understanding of Lucretius' observations, it is essential to first clarify how granular media are defined.

Some definitions roughly describe granular media as a material composed of a large number of distinct particles that are not linked by covalent bonds. Others describe them as a conglomeration of discrete solid, macroscopic particles characterized by a loss of energy whenever the particles interact[2]. More specifically, covalent bonds appear for materials where the grain diameter is less than 100 μm (actually, such materials are commonly referred to powders or colloids)[3]. Consequently, the term "granular media" covers all materials composed of macroscopic solid particles larger than 100 μm. And these, we come across every day of our lives! From sugar to asteroid belts, not forgetting sand, rice or pebbles. In their definition, we are told that these particles don't interact by covalent bonds, but they actually still interact. Indeed, these interactions between individual particles, mainly by contact, friction and collision, shape the collective behavior and dynamics of granular media.

Figure 1: Some exemples of granular materials. From left to right : Sand, rice, asteroids, rocks and wood pellets

Men's interest in granular media is not without reason. The study of granular materials plays a key role in two major domains:

The first one is industrial applications, where granular materials are the second most used material in terms of quantity, the first being water. Man has sought to take advantage of their special properties to solve a whole range of problems. For instance, the ability of a solid materials to behave like fluids simplifies transportation and storage processes, providing an energy-efficient mechanism. This led to the development of initial designs for chutes and hoppers. It was also thanks to studies on granular materials that construction materials technologies were revolutionized[3]. The second application area covers the understanding of geophysical phenomena such as rockfalls, avalanches, and landslides. The primary objective of studying these granular materials is to comprehend, forecast, respond to, or simulate such events.

Another reason why granular media are so fascinating is simply fundamental physics. Because they lie between two worlds, those of fluid mechanics and solid mechanics, we still have not managed to describe their behavior perfectly.

The attentive reader will notice that we have been talking about granular flows from the outset, but the subject of this thesis refers to granular collapse in water. In fact, there are some significant differences in the behavior of granular materials in dry or liquid environments. The interest in studying such flows lies mainly in

Figure 2: Submarine landslide ©Ifremer

geophysics. We mentioned landslides above, but they also happen underwater. Landslides are much larger under the sea than on land, and can travel for thousands of kilometers, causing major damage or disruption to marine life, and even tsunamis in the case of the largest. One of the best-known examples is the collapse of Nice airport in 1979 [4]. A large volume of sediment broke loose and began to fall beneath the sea, triggering a tsunami which in turn triggered a landslide on land, destroying part of the airport.

To find out more about these granular flows in aqueous media, several numerical simulation models are being developed. In this thesis, our role will be to carry out experiments, with very precise configurations, so that we can compare our results with numerical simulations using the model developed by Monsorno *et al.* [5]. These simulations represent the collapse of a sand column in an aqueous medium in 2D. To reproduce these conditions, we will work in a water-filled channel in which we will place a column of sand that will have to collapse. To achieve this, the column will be placed between two plates, one of which will be removed to allow the collapse to take place. Previous UCLouvain thesis had already explored the experimental study of the collapse of a sand column in water [6], but due to a too constraining experimental setup, the experiments and results were impacted. Our objective is to design and explore a new setup, define its strengths and weaknesses, and then carry out experiments that are comparable with numerical simulations.

This thesis is divided into two distinct parts. The first one will focus on the design of a system enabling a door to be opened instantaneously. It will allow the sand column to collapse into the channel. It will start with the specifications, go through the various stages of the design process and the assembly, right up to the final validation of the system.

The second part will involve an experimental study of the collapse of a granular column in water at rest. Using the system designed in the first part, series of experiments will be conducted. It will start with a brief description of the theoretical model used in the simulations. A comprehensive analysis of the key parameters that influence the collapse will be carried out. Subsequently, the experimental set-up will be presented including the characterization of the channel, the sand used and the image processing methods employed. The experimental results will be introduced through a parametric study. The results will be analyzed using Python image processing techniques and Davis 8, a PIV software.

Finally, a comparison will be made between these experimental results and the ones obtained from the former setup. Moreover, a comprehensive comparison between our experiments and numerical simulations will be carried out.

1

State of the art

Since granular media are handled by both specialists and non-specialists, their properties have been known empirically since ancient times. Indeed, the learning about the behavior of granular materials began long before the birth of the scientific method. In ancient Egypt, for instance, Egyptians used the properties of sand to build their traditional monuments.

We can also mention the famous Barchan dunes with their typical crescent-shaped dunes. People living in desert regions, such as the Sahara, had already estimated the time it would take for this kind of dune to cover its own length. They were then used as a means of storage by these people to protect their goods from looting. The dune was chosen according to its size and the desire to recover more or less quickly, at the back, the goods previously buried at the front [7].

Figure 1.1: Barchan dunes in Paracas national park [8]. Credits `@George Steinmetz`

This chapter describes non-exhaustively the advances in this research area in chronological order. It was with the considerable development of science and technology in the 17th century that we began to explain, and above all understand, phenomena observed for so many years.

However, it was not until several hundred years later that the first scientists took an interest in this particular medium. The earliest example of granular flow modeling began in 1773 with the Coulomb's paper [9] who first described the yielding of granular materials as a frictional process. In 1852, granular flows were also studied with the sand in an hourglass by Hagen [10]. Reynolds, in 1885, presented the granular media as a particular media. He pointed out the existence of a fundamental property of granular media that is not possessed by fluids or solids. He named this fundamental property "*dilatancy*", also known nowadays as the "*The Reynolds dilatancy*". One observes that it was really the beginning of the research on granular media as he wrote, while describing their dilatancy :"*On perceiving something which resembles nothing within the limits of* ***one's knowledge****, a name is a matter of great difficulty*" [11] Reynolds continued to study these media and in particular the phenomenon of dilatancy [12].

It was then, Einstein's turn, between 1900 and 1911, to make his contribution with his seminal works [13] [14]. Einstein computed the increase in viscosity resulting from the addition of a few particles to a viscous Newtonian fluid. He computed this first linear correction in volume fraction to the viscosity based on the perturbation caused by a single particle immersed in a shear flow[15].

Brown and Hawksley (1945-1947) have analyzed the packing of regular (i.e. spherical), and irregular particles [16] and the effects of container walls on the packing density of particles [17]. They have shown that a loosely-packed granular media will not have the same behavior as a dense packing. It is this difference in the notion of loose or dense that can be complicated to estimate. Indeed, it remains difficult to evaluate and to measure the packing of a sand column, whereas it is an essential parameter in numerical models.

It may also be important to note the work of Terzaghi (1950) [18]. Although he pioneered a great range of methods and procedures for geotechnical engineering, his works on soil mechanics have been the basis for many works on granular flows.

From 1950, the number of scientists and engineers who dedicated their talents to the question of granular media has grown steadily. Unfortunately, they were limited by the available technologies at that time and performed a lot of observations and experiments. Among them, we can cite Ralph A. Bagnold. He developed the `Bagnold formula` [19] in 1941 and the dimensionless `Bagnold number`[1] [20] in 1954 for characterizing sand flows. Within the same year, he also developed a constitutive relation for a suspension of neutrally buoyant particles in a Newtonian fluid[20].

Pre-kinetic-theory experimentations primarily focused on engineering applications of chute flows of granular material. While these studies, summarized in reviews by Savage et al. (1983) [21], laid a qualitative foundation for theoretical

---

[1] The Bagnold number (Ba) is the ratio of grain collision stresses to viscous fluid stresses in a granular flow with interstitial Newtonian fluid

development, they provided limited quantitative data for testing theories. In this context, a lot of physical experiments were properly designed and performed by Thomas G. Drake in 1991 to link the computer simulations with theory.

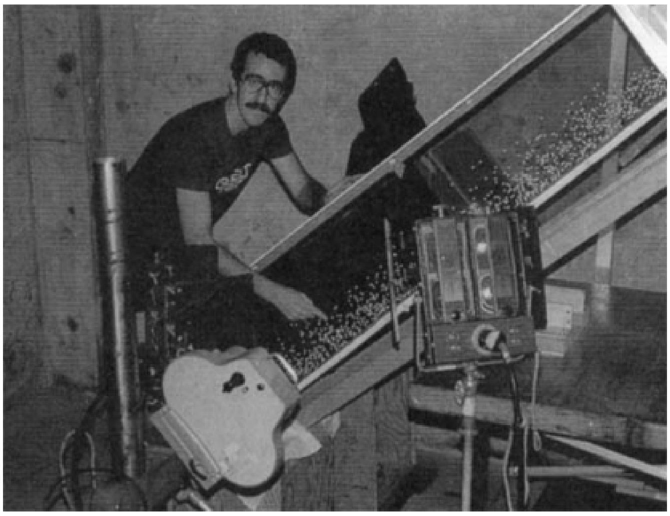

Figure 1.2: Drake performing his experiments in 1991 with an experimental chute, measuring 3.7 m in length, 0.5 m in depth, and 6.7 mm in width, where a typical dispersal flow occurs. Plastic spheres with a diameter of 6 mm are fed from a hopper located above and behind the upper end of the chute. A high-speed camera, operating at approximately 1440 frames per second, captures particle motion. From [22]

From the 1990s, researchers developed several models in an attempt to match the same efficiency as existing models in fluid mechanics and soil mechanics. Both experimental work and theoretical models have progressed simultaneously, and by being interconnected, they enabled researchers to enhance their predictions and comprehension of granular media. We can highlight the model of Savage *et al* (1991) [23] with their model to predict the flow on an initially stationary mass of cohesionless granular material down rough curved beds. Their researches are particularly relevant in relation to the movement of rock and ice avalanches, as well as dense flow snow avalanches. Campbell (1990) also provided a model to predict the rapid granular flows [1], based on the granular temperature. This granular temperature[2] was initially suggested by Ogawa in 1978 [24]. Campbell concludes in his paper that available experimental data primarily focus on global properties, such

---

[2] The granular temperature is used to characterize the disorders of particle system. There are two mechanisms for its generation: the random movement of particles and the collisions between particles

as the stress/strain rate behavior of the system but there are limited measurements of microscopic properties, such as granular temperatures. Indeed, at that time, the study of granular media relied heavily on continuum mechanics, which treats the material as a continuous medium. However, this approach did not allow the examination of each individual grain and its interactions with the others and the fluid.

During the 2000s, researchers made significant progress in understanding the behavior of granular media at the microscopic scale. This was made possible due to the accumulation of previous experimental data and the development of discrete modeling techniques [6]. From then, the question was whether a collection of macroscopic particles could be accurately described as a continuum, and if its constitutive relations could be appropriately incorporated into a global continuum theory. Nowadays, this question, whether the granular media should be treated in a continuous or discrete way, remains an open and ongoing debate. Both approaches, considering the problem from a continuous perspective or a discrete perspective, are still present in research. Each one has its advantages and limitations; discrete modeling is accurate but computationally expensive, whereas continuum model is computationally efficient but its accuracy is doubtful in some situations [25].

A mixture of a granular material with fluid can be treated with various approaches. These approaches generally fall under "two-phase" models. Two-phases models can further be split into three approaches[6]:

- **Eulerian-Lagrangian** models: The fluid phase is considered as a continuum and the grains of the granular medium are tracked individually.

- **Lagrangian-Lagrangian** models: Both the fluid and granular phases are treated as particles

- **Eulerien-Eulerian** models: both the fluid and granular phases are treated as continuous media.

Subsequently, we will from this point summarize the literature by categorizing the research into three mains categories: an experimental category and two numerical categories with the discrete and the continuous approaches. The discrete approach, or discrete modeling, includes the Eulerian-Lagrangian and Lagrangian-Lagrangian approaches since they deal with particles.

Discrete point of view

From a discrete point of view, the modeling of "dry" granular media, where the fluid is considered "negligible" (e.g., air), began with the innovative work of Cundall (1971) using the Discrete Element Method (DEM). In his model the elements or grains can freely make and break contacts with their neighbors [26]. In 1979, Cundall and Strack developed another computer model based on the basic elements of grains and their interactions to describe the behavior of granular media. They concluded, after comparing their model to photo-elastically obtained vector forces, that the discrete element method was a valid tool for studying granular media behavior [27].

When particles are mixed with a fluid that is not negligible anymore, such as water, two perspectives can be taken. The first perspective considers the mixture of particles and fluid as a single-phase system with effective rheological properties. The second perspective, as previously mentioned, can be seen as a two-phase system where the fluid and particles can undergo relative motion[15]. Sitharam (2003), using a modified version of the model developed by Cundall and Strack, demonstrated that DEM can accurately simulate the macroscopic cyclic behavior of sand under drained and undrained conditions [28]. A micromechanical perspective with three dimensional discrete element modeling of granular media was performed by Soroush and Ferdowsi (2011) [29]. Since the seminal works of Cundall, other researchers have further developed discrete models, such as Zhu *et al* (2008) [30], Mutabaruka (2013) [31]. In 2021, Lacaze *et al* presented a paper to show the different regimes that can be encountered in the case of the collapse of a granular column depending on several dimensionless parameters like the Bond number Bo and the Stokes number St [32].

Continuum point of view

From a continuum point of view, the modeling of granular media is relatively recent. Jop *et al* (2006) proposed a new constitutive law for dense granular flows, inspired by recent numerical and experimental work [33]. As for discrete modeling, a continuum model as been developed for the dry case by Jiang and Liu (2008) [34]. In 2013, Henann *et al* proposed a predictive, size-dependent, continuum-level, 3D constitutive theory for well-developed dense granular flow. Their main assumption in the model was that the steady flow progresses at constant volume [35]. Additionally, notable continuum models have been developed by Weinhart *et al* (2013). Goddard conducted a survey in 2014, focusing on essential phenomenological aspects of granular flow and providing a unified mathematical synthesis of the prevailing continuum models at that time [36].

Currently, at UCLouvain, within the research conducted at the Institute of Mechanics, Materials and Civil Engineering (iMMC), both the discrete approach, led by the Migflow team [37], and the continuous approach, led by Professor Papalexandris with his research team [5][38], receive much attention. It is with the work of the latter team that we will further compare our experimental results.

Experimental point of view

In addition to the people already mentioned who have contributed with their expertise to the development of experiments on granular media, such as Reynolds (1885), Bagnold (1954), Drake (1991)... Many other experiments have been carried out, particularly since the 1990s. In 2004, the French research group "Groupement De Recherche Milieux Divisés" listed and compared many experiments already existing. They concluded that, with their knowledge of granular flows and the amount of data available at that time, "one can no longer consider a single geometry as a test for constitutive law but should consider the different geometries" [39]. Indeed, we can present a lot of different geometries of experimental setup to study the granular media either in 2D or 3D.

2D Planar flows:

- Lube *et al* (2005) in a dry case but with two opening gates[40]. (See Figure 1.3d)
- Thompson and Huppert (2007) in water with sand $d_{50} = 0.5$ mm[41] (See Figure 1.3e)
- Lacaze *et al* (2008) in a dry case [42]. (See Figure 1.3f)
- Rondon *et al* (2011) with a mixture of water and UCON oil as the fluid [43].
- Lee *et al* (2018) in water with glass beads [44].
- Nennen (2021) in water with sand $d_{50} = 1.72$ mm[6].

Surface flows:

- Grasselli and Herrmann (1997) in a dry case [45]. (See Figure 1.3b)
- Bonamy *et al* (2002) in a dry case with a rotating drum a[46].

- du Pont *et al* (2003) in a dry case with a rotating drum [47]. (See Figure 1.3c)

2D Inclined planes flows:

- Azanza (1997) in a dry case with a bottom covered with glued grains [48].
- Berton *et al* (2003) in a dry case with a bottom covered with glued grains [49].

3D Inclined flows:

- Pouliquen (1999) in a dry case [50].
- Daerr *et al* (1999) in a dry case and bottom covered in velvet clothes [51].

2D Vertical chute flows:

- Pouliquen and Gutfraind (1996) in a dry case [52]. (See Figure 1.3a)
- Chevoir *et al* (2020) in a dry case [53].

3D Vertical chute flows:

- Chevoir *et al* (2001) in a dry case [54].

As we can observe, there are many possible geometries for studying granular media and some of the experiences listed hereabove are presented in Figure 1.3. Moreover, since granular media is a fairly vast medium, we can further differentiate experiments by varying the types of particles used. One presents hereunder a non-exhaustive list of particles used in experiments:

- **glass** with Grasselli and Herrmann (1997)[45].
- **steel** with Bonamy *et al* (2002) [46].
- **sand** with Thompson and Huppert (2007) [41].
- **aluminium beads** with Azanza (1997) [48].
- **polystyrene disks** with Berton *et al* (2003)[49].
- **mustard seeds** with Chevoir *et al* (2001) [54].

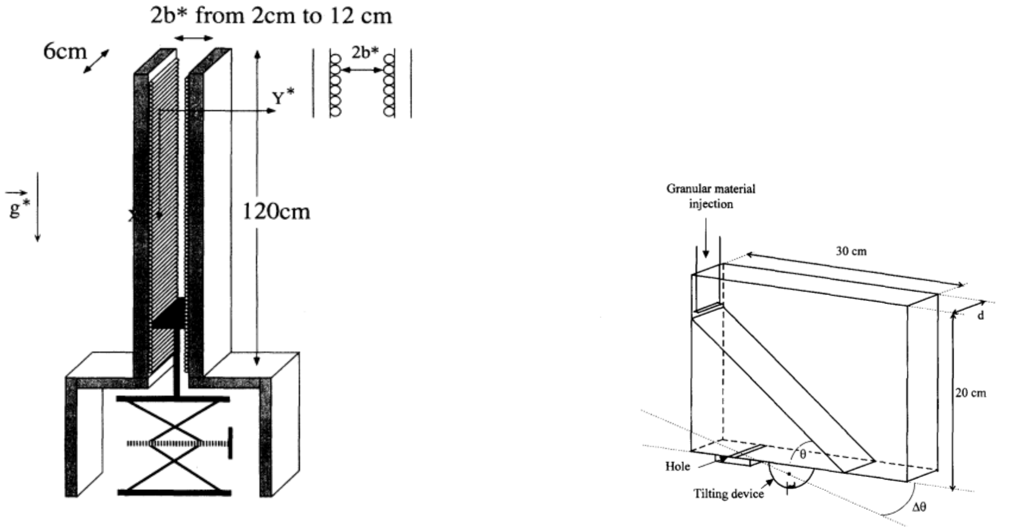

(a) Pouliquen and Gutfraind (1996) [52]

(b) Grasselli and Herrmann (1997) [45]

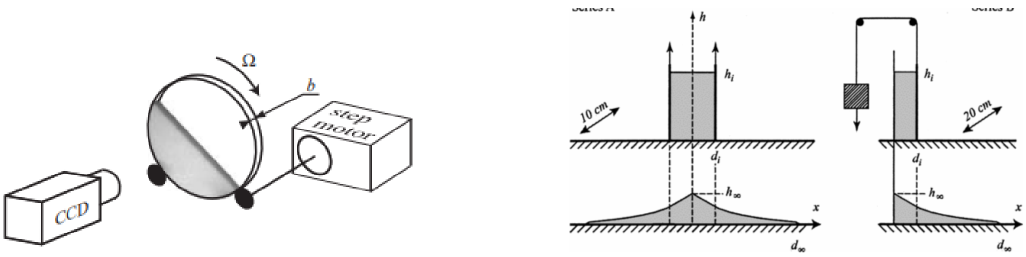

(c) du Pont *et al* (2003) [47]

(d) Lube *et al* (2005) [40]

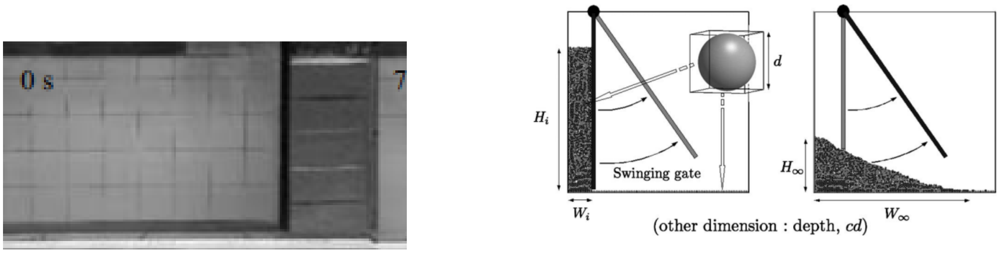

(e) Thompson and Huppert (2007) [41]

(f) Lacaze *et al* (2008) [42]

Figure 1.3: Various experimental systems

Finally, the experiments that closely align with our research objectives are the experiments conducted by Thompson and Huppert (2007). They analyzed a mixture of water and sand, exactly equivalent to our study. The main problems with this experiment were the the disturbance of the initial conditions caused by initiating the collapse using an upward-pulled door. To avoid this disturbance, Nennen (2021) conducted experiments under the same conditions but with a setup where the door was pulled downwards.

Nevertheless, it turned out that her set-up encountered other significant problems than this initial disturbance. Therefore, the aim of this thesis is to reproduce the aforementioned experiments by implementing an upward-pulled door in a different channel.

This page is intentionally left blank.

Part I

Design of an experimental mechanism

This page is intentionally left blank.

2

Conception context

In order to observe the collapse of a granular column in a body of water at rest, multiple experimental setups were investigated. In 2021, a master thesis [6] conducted by Flora Nennen used a system with a door that lowered under the channel using a pneumatic system. This chapter explains the limitations and problems encountered with this former setup and explain the objectives and requirements for a new experimental mechanical system.

2.1 Limitations of the previous design

Before describing the new designed system, we will first outline the former model and explain the limitations that have led to a complete re-design. In the former model, the experiments took place in a channel that was 6 meters long and had a rectangular cross section of 0.25 x 0.5 meters. The walls were vertical and perfectly perpendicular to the bottom of the channel. At the center of this channel there was a door. In order to form a column, the sand was put between a movable panel and the sliding door. This allowed the user to choose the length of the column in the longitudinal direction. When one wanted the column to collapse, the door was removed downward pneumatically, allowing the release of the sand. The mechanism used to pull the door was working with a pressure of 8 bars.

2.1.1 Free surface

The movement of the door caused variations in the water surface that was supposed to be at rest. This might induce some irregularities in the experiments because it could lead to undesired movement in the granular column. Moreover, the free surface motions were different each time and could therefore have had an impact on

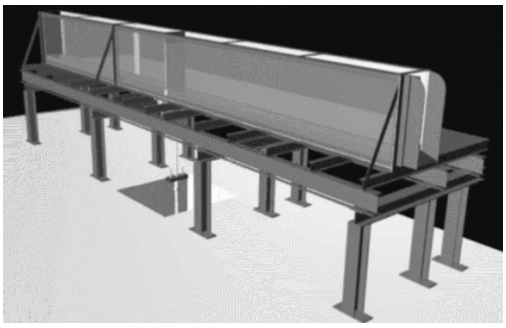

Figure 2.1: Previous system 3D model

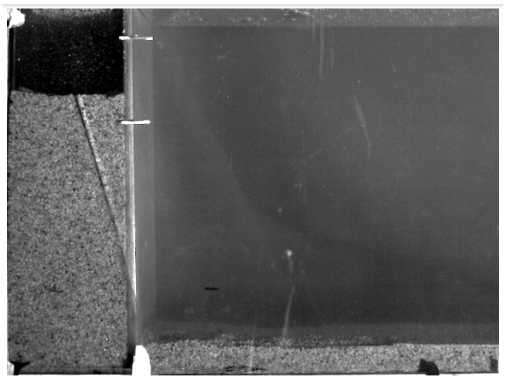

Figure 2.2: Previous system setup

the repeatability of the experiment. A solution that has been explored is putting a polystyrene panel on top of the water to reduce variations, but this did not have any significant effects. The next section shows that the sealing also had an impact on the free surface movement.

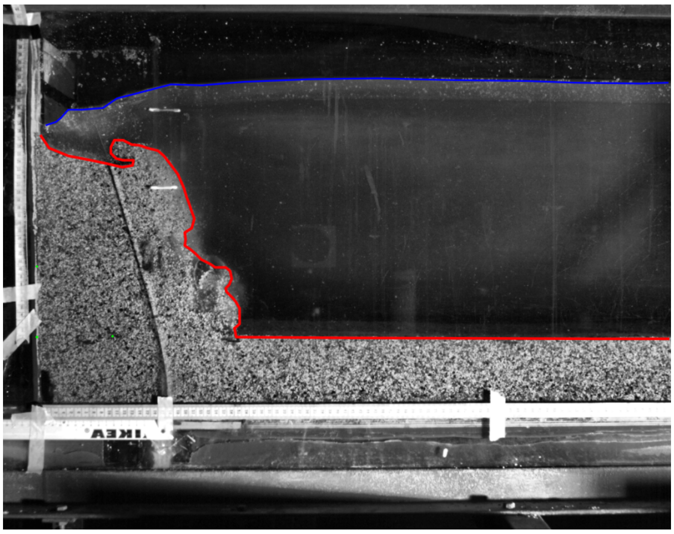

Figure 2.3: Free surface instabilities in the previous system (blue line)

2.1.2 Sealing

The former channel and door system had multiple sealing issues. First, the experiments had to be conducted quickly after filling up the channel because the sealing at the downstream end was not efficient enough. This induced some

differences in water level before and after the door, inducing free surface movement as well. In addition, the gasket of the door was quite old and hardened, leading to lack of efficiency.
In addition, the downward opening made sealing under the channel really difficult, leaks were quite important under the channel at the door's position.
The sealing of the new system is studied in section 8.5.

2.1.3 Pneumatic System

Due to the downward opening movement, frequently some sand grains got carried away with the descending door. These grains often got stuck in the door's passage leading it to be completely jammed despite the power of the pneumatic system. The researchers had then to wait for a technician to dismantle the system, clean it and reassemble it. It could take days before an experiment could be carried out again.

2.1.4 Unmovable door

The previous door system was fixed at the center of the channel. Being unmovable, the diversity of experiments that could be carried out was limited. A movable door offers even more possibilities for a multipurpose use.

2.2 System requirements

In the following sections, the main functions that are expected from the system are presented, as well as the principal constraints. In a nutshell, the goal of this system is to fix some of the former model limitations by designing a system with a rising door. It has to be removed quickly enough to allow observation of the collapse of a granular column.
The detailed specifications are available in Appendix A.

2.2.1 Functional requirements

The requirements are split in four **Main functions**, abbreviated *MF* hereunder.

- **MF 1 : Open and close the door**
  This represents the core of the project. The door should open in a certain way, with a speed that is important enough to ensure the initial conditions of the column. The opening should also be vertical. Due to the previous door's problems, we were asked to conceive a rising door instead of a lowering one.

- **MF 2 : Guiding the door**
  The door must be guided in the vertical direction when it moves.
- **MF 3 : Seal at the door**
  Due to the purpose of the door, it should be properly sealed. Meaning no water or sand particles should be able to pass from one side of the door to the other.
- **MF 4 : Move and lock the system along the channel**
  This requirement is different to the previous system. The channel we were asked to work on is 7.6-meters long and is equipped with rails. Using the latter, the system should be able to move along these rails and to be locked at any position on the channel.

2.2.2 Constraints

The specifications for the system also include the main constraints that the door system will have to respect. The detailed constraints requirements are available in Appendix A.

1. **Opening speed**
   The opening speed must respect the condition of instantaneousness, meaning that our door must be lifted up fast enough. A criterion to characterize the instantaneouness has been proposed by Lauber and Hager [55]. This criterion is described in Section 5.2.
2. **Channel dimensions**
   The channel has an internal section of 500mm wide and 400mm high. The rails have an inverted T shape and a 5mm cross-section. The total length of the channel is about 7.6 meters. See details in Figure 2.4.
3. **Pressure resistance**
   The door will be submerged either in water or sand-water mixture. It can even have water on one side and air on the other. All of this induces hydrostatic pressures that the door must resist.
4. **Water resistance**
   Since the system will be used in an environment where there is many water splashing, it must avoid rusting.
5. **Sandy environment**
   A lot of grains with different sizes and shapes will be present in the working environment. The system must keep on working correctly in this environment and avoiding the jamming and abrasion of the system by the sand grains.

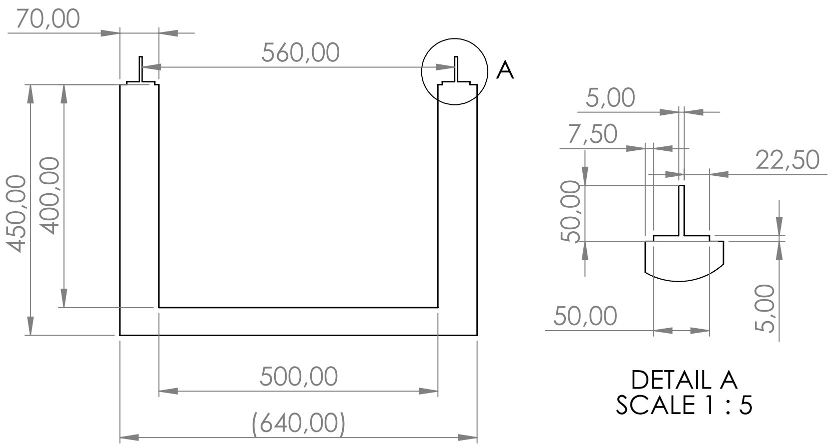

Figure 2.4: Dimensions of the channel

6. **Cost**
   The total cost of the project should not exceed 3000€ TVAC.

7. **Multi-purpose**
   The system should not only be used to study the collapse of a column of sand and should also be usable for other applications such as the simulation of a dam break.

This page is intentionally left blank.

3

Design process

The design process is complex and comprehensive in order to find the best fitting solution. Allowing to pause, look back, question and reorder what has been done when necessary. In this Chapter, the different steps are presented and their purposes as well as some difficulties encountered and things we wanted to highlight during the process.

3.1 Requirements

The initial step involved the identification of the main challenges, functions, constraints and limitations of the given problem. We had to question people involved in the former setup to gather insights in what has been done and the underlying reasons for the proposed changes. Specifications and requirements could next be elaborated and highlighted as presented in Section 2.2. To establish a clear and concise road map of the system's operations, we summarized the main functions into a functional graph, outlining the step-by-step actions that the system needs to undertake. The functional graph offers a clear visual representation, a logical structuring, and facilitates communication and process optimization [56] [57].

3.2 Determination of the solutions

For each of the main functions described in Section 2.2.1, we brainstormed to identify suitable solutions. Employing an iterative procedure, we sketched out all the potential solutions and compared them. Taking into account their respective drawbacks and advantages to determine the optimal design solution for our specific situation.

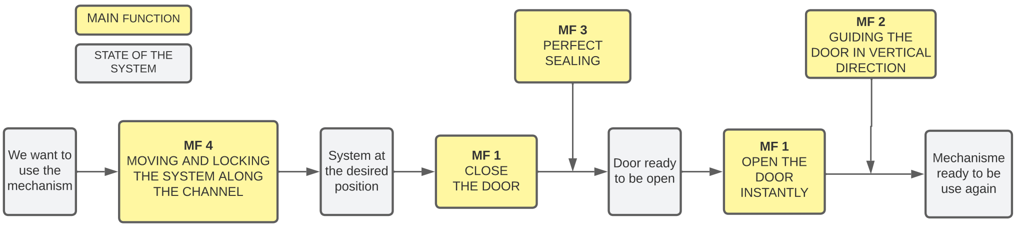

Figure 3.1: Functional graph of the required system/mechanism

To illustrate this process, let us briefly expose some solutions we explored for one of the main functions and the iterative procedure we followed to obtain the best one.

MF 1: Open the door

The first main function of the mechanism is to instantly open a door. To achieve this, we firstly considered several solutions:

- Using a counterweight system.
- Implementing a pneumatic system like the former channel.
- Employing a hydraulic system.
- Using a motorized mechanism.

When evaluating these solutions to the constraints of our situation, the counterweight system emerged as the most promising option. Indeed, this solution provides the flexibility to adjust easily the lifting load and thereby allowing control over the door's opening time. Moreover, it offers user-friendly operations and avoids big maintenance challenges associated with pneumatic, hydraulic or motorized systems.

Even with the choice of a counterweight system for raising the door, there were multiple implementation possibilities. In Figure 3.2, the reader can observe three potential ways of implementation of the counterweight considered in our situation.

After consideration, the second solution, which involves using a single weight was selected for several reasons. Firstly it allows a easier motion of the entire mechanism all along the channel. Secondly, it ensures that the two cables can be attached to the same weight, simplifying the process of having equal tension in both cables. Lastly, opting for an asymmetrical single weight would likely result in a higher usage of materials and present greater challenges in having perfectly balanced loads with the counterweight.

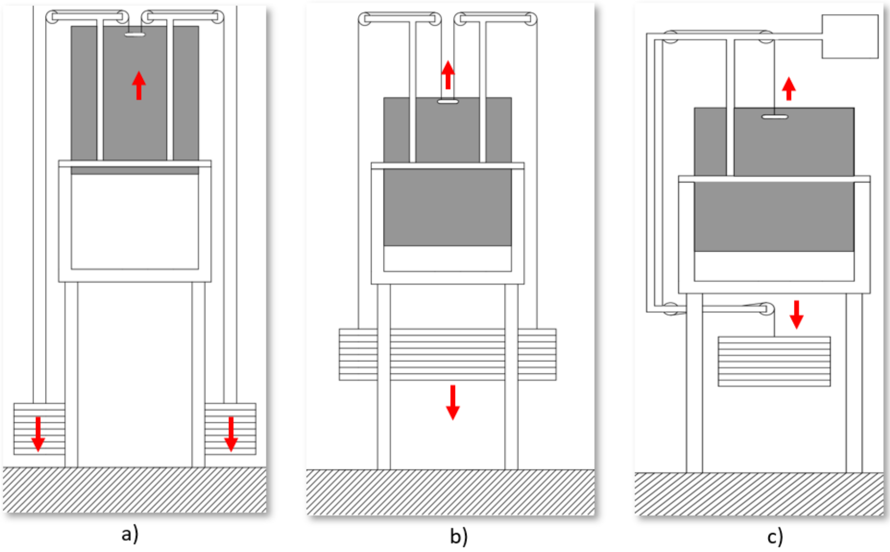

Figure 3.2: a) Dual weight b) Single weights c) Asymmetrical single weight. Several possible solutions for the counterweight system.

3.3 Dimensioning phase

Once all the solutions we found for each main functions are combined, we obtained our comprehensive final solution. The subsequent step involved to dimension the components of our design and creating preliminary drawings to facilitate modeling it in a CAD software such as SOLIDWORKS.

When dimensioning the components, we relied on various approaches outlined in `"Fundamentals of Machine Component Design"` [58] and all the dimensioning methods we employed were derived from this book.

Accurate dimensioning of components is crucial. For instance, considering the bearings carrying out the displacement of system along the channel. MISUMI offers bearings with outer ring diameters ranging from 6mm to 52mm. It may seem challenging to choose the appropriate diameter among the available ones. However, through calculations and models, we can quickly determine the required diameter for our specific application.

Let's explore the example dimensioning our bearings, where their main function is to enable smooth motion of the mechanism along the channel.

3.3.1 Bearings selection

As previously said, we used the bearing selection method from [58].
For this, a main equation is proposed by Palmgren [59], i.e:

$$L = K_R L_R \left(\frac{C}{SFF_e K_a}\right)^{\frac{10}{3}} \tag{3.1}$$

where

C is the rated capacity, which we need to determine to find an associated bore diameter of the bearings.
L_R is life corresponding to the rated capacity (i.e, 9×10^7 revolutions).
K_R is life adjustment reliability factors.
F_e is the equivalent load.
K_a is an application factor to take into account shocks loading.
L is the time life, in revolutions, required by the application.
SF is the Safety Factor corresponding to our application.

The Palmgren Equation 3.1 can be rewritten to determine C;

$$C = F_e K_a \left(\frac{L}{L_R K_r}\right)^{\frac{3}{10}} \tag{3.2}$$

In our application, as we only have pure radial load F_r, we can consider that $F_e = F_r$. To estimate the radial load, we first followed the recommendations of Vidosic (1957) [60] and chose a safety factor of $SF = 5$ considering the impact forces and the importance of human security in case of failure of the mechanism. Additionally we can roughly estimate through Solidworks the weight of the mechanism that the bearings will carry, and this is about $100kg$. Having 4 bearings and assuming that the radial load is equally distributed between them, each one will carry $25kg$. Since we have light impact, we can choose a value for K_a of 1.55. Moreover, we decided to have a 95% reliability and not 90%, and therefore chose $K_R = 0.63$
Finally, in view of the type of application and its relative design life, our mechanism is more for infrequent use. It will consequently have a design life of about 500 hours[1].

By substituting these parameters into Equation 3.2, we derived an approximate value for C of

$$C = 1.347 \ \mathbf{kN}$$

---

[1] Since the Palmgren equation required a design life in revolution, we assumed a 600 RPM speed when in motion

Based on the calculated value of bearing rated capacity, the book [58] suggests using Radial Ball bearings with a bore diameter between 17 and 20 mm. According to this dimensioning recommendation, we have decided to select bearings with an inner ring diameter (bore) of 20 mm and with an outer ring diameter of 37 mm.

3.3.2 Counterweight selection

As explained in Section 3.2, we will use a single mass counterweight system to raise the door instantly. Therefore, we will need to approximate the weight needed to successfully instantly lift the door. Hence, we need to calculate the forces acting on the door itself that we will need to overcome to be able to lift the door up.
The forces that the weights will have to overcome can be divided into three components. One comes from the weight of the door, F_w. Another comes from the friction on the door due to the hydrostatic pressure, F_{fp}, and the last one comes from the friction forces at the contact surface between the gaskets of the door and the channel walls, F_f. Thus,

$$F_{tot} = F_w + F_{fp} + F_f \tag{3.3}$$

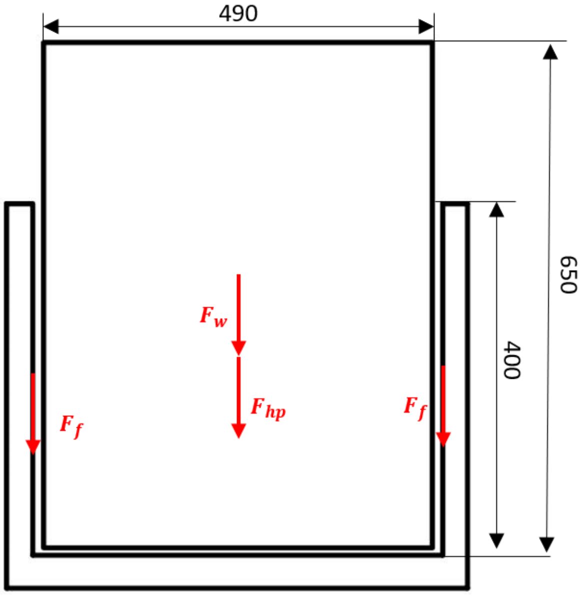

Figure 3.3: Drawing of the forces acting on the door

We can now compute and estimate all the forces acting on the door.

$\underline{F_w}$

The door is detailed in Section . To quickly summarize, it is composed with two stainless steel plates of $2mm$ and between them stands a $5mm$ plexiglas plate. All of that gives us a total mass of $m = 10.189$ [kg] meaning that

$$F_w = mg \approx 100 \text{ [N]}$$

$\underline{F_{fp}}$

To estimate friction forces on the door due to hydrostatic pressure, we will consider the worst case our system may undergo. It is when we have full sand mixed with water on one side of the door. The local horizontal force acting on one side of the door in this configuration is due to the hydrostatic pressure and is equal to

$$F_p = (\rho_{sw} g h) A \tag{3.4}$$

where $g = 9.81$ [m/s^2] is the gravitational constant,

$$A = 0.400 \times 0.490 = 0.196 \text{ [m}^2\text{]}$$

is the immersed surface of the door. $h = 0.4$ [m] is the height of the sand/water mixture, ρ_{sw} the density of the mixture.
According to `Geotechdata` [61], the minimum sand porosity is equal to $\eta = 40\%$ meaning that

$$\begin{aligned} \rho_{sw} &= \eta \rho_w + (1 - \eta)\rho_s \\ &= 1984 \text{ [kg/m}^3\text{]} \end{aligned}$$

where we consider a sand density $\rho_s = 2640$ [kg/m^3] and water density $\rho_a = 1000$ [kg/m^3] at $20°C$.

We finally computed the hydrostatic pressure on one side of the door

$$F_p \approx 1526 \text{ [N]}$$

A static friction coefficient between dry sand and steel has been estimated by Uesugi and Kishida[62] with a value of $\mu_s = 0.31$. We can now estimate the total friction forces on the door as:

$$\begin{aligned} F_{fp} &= \mu_s \times F_p \\ &= 473 \text{ [}\mathbf{N}\text{]} \end{aligned}$$

$\underline{F_f}$

The last component of the forces acting on the door to overcome is the friction force due to the contact between the door's gaskets and the walls of the channel.

If we assume a linear elastic deformation for the gasket, that it will be compressed by $\epsilon = 1.5$ mm, we can estimate the stress σ applied by the walls on the gaskets:

$$\sigma = E\epsilon \tag{3.5}$$

where $E = 0.01$ [GPa] is the Young's Modulus of the rubber. Knowing the total surface in contact $A = 0.0096$ [m^2], we can easily derive the force acting on the gaskets, i.e.

$$\begin{aligned} F_f &= A\sigma = AE\epsilon \\ &= 144 \text{ [N]} \end{aligned}$$

We can now computed the total force F_{tot} to overcome to be able to lift the door:

$$\begin{aligned} F_{tot} &= F_w + F_{fp} + F_f = m_{CW}g \\ &= 717 \text{ N} \end{aligned}$$

In summary, we computed the total force acting on the door by assuming at each time the worst situation/case. That gives us an upper value of the total force to overcome. Thus, it also gives us an upper value of the mass m_{CW} needed on the counterweight system of

$$\boldsymbol{m_{CW} \approx 75 \textbf{ kg}}$$

Once we have computed the maximum weight our system will have to carry, it is interesting to estimate the pull-out speed of the door, to verify if it is fast enough to be characterized as instantaneous.

Our counterweight system will be composed of two masses: one mass will free-fall by 0.45 m and will encounter a second mass, that is attached to the door through cables. It should be noted that the second mass is only held by the cables, meaning that they are fully tensioned. We can therefore assume that the speed of the second mass on the impact with the first will be the speed at which the plate is lifted up. The situation is resumed in Figure 3.4.

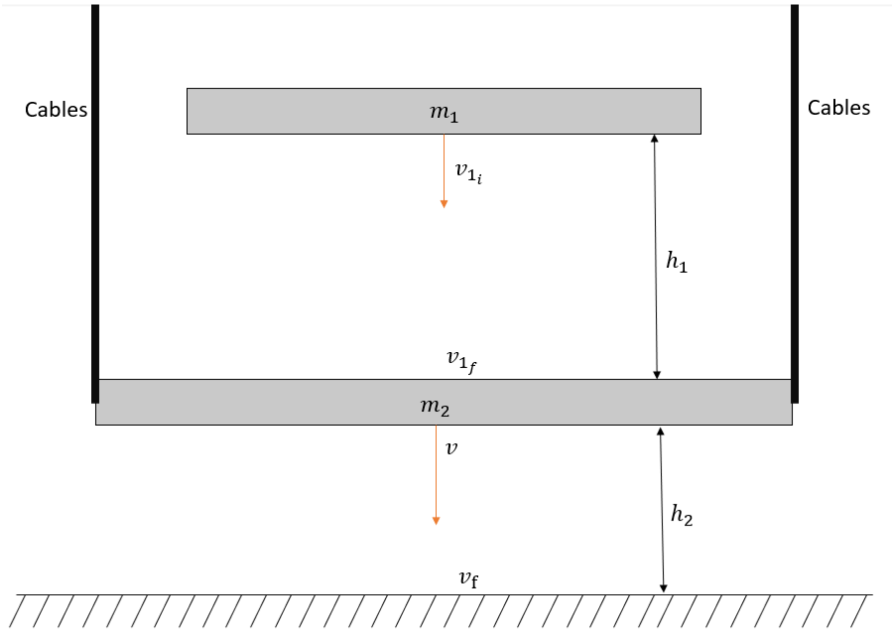

Figure 3.4: Situation summary to estimate the speed at which one the door is lifted up

Since the maximal mass for the counterweight is 75 kg, taking account of a SF of 2, we will compute the speed as we only have one half of the mass, i.e. 37.5kg. These 37.5 kg are distributed as follows: $m_1 = 25kg$ and $m_2 = 12.5kg$. The calculation of the speed is straightforward, since we are in free-fall for the first mass ($v_{1_i} = 0$), the second mass is attached and has no speed ($v_{2_i} = 0$), $h_1 = 0.45$m, $h_2 = 0.40$m and if we assumed a perfectly inelastic collision, we directly obtain the desired speed:

$$v = \frac{m_1\sqrt{2gh_1}}{m_1 + m_2} \approx 1.98\text{m/s} \tag{3.6}$$

If we assume that the door is constantly lifted up by this speed, the door will be completely lifted up in approximately 0.201 seconds. If we rise the total weight up to 75 kg and assuming the same mass for m_2, we obtain a speed of 2.48 m/s and so a lifting time of approximately 0.161 seconds. It seems relatively instantaneous, but the instantenousness is validated in Section 5.2. We will consider this dimensioning for the counterweight.

3.3.3 Door design

When designing the door, two parameters were primordial. The door needed to be as light as possible in order to have a light counterweight for practical and security reasons. It also has to be the most rigid possible to avoid significant deflection when submitted to the hydrostatic pressure. Moreover, it should be resistant to abrasion to avoid the sand grains to damage the material. The door has, of course, to be waterproof.

For the waterproofness and resistance, stainless steel was the ideal candidate and, moreover, it was available in the UCLouvain lab reserve. But it has a very high density ($\sim 7750kg/m^3$). To lighten the piece, a Plexiglas sheet ($\sim 1200kg/m^3$) is placed between two stainless steel plates. This Plexiglas sheet has been cut on the inside to lighten it even more.
The two stainless steel plates are 2 mm thick each and the Plexiglas sheet is 5 mm thick giving a total thickness of 9 mm. The 3D model is presented in Section 4.4. To verify the deflection, a Solidworks static simulation has been performed and results are available in Figure 3.5. The four blue circles in the upper part of the door are the guiding rollers, considered fixed. We simulated the hydrostatic pressure using :

$$\begin{cases} F(x,y,z) = \rho_{sw} \cdot g \cdot (0.4 - y), & \text{if } y \in [0, 0.4] \\ F(x,y,z) = 0, & \text{if } y > 0.4 \end{cases} \tag{3.7}$$

With ρ_{sw} is the density of the sand-water mixture, g the gravitational acceleration and y the height (0.4 m being the height of the water surface $\Leftrightarrow y_{max}$).
We can see on Figure 3.5 that the maximum displacement shouldn't exceed 1.9 mm.

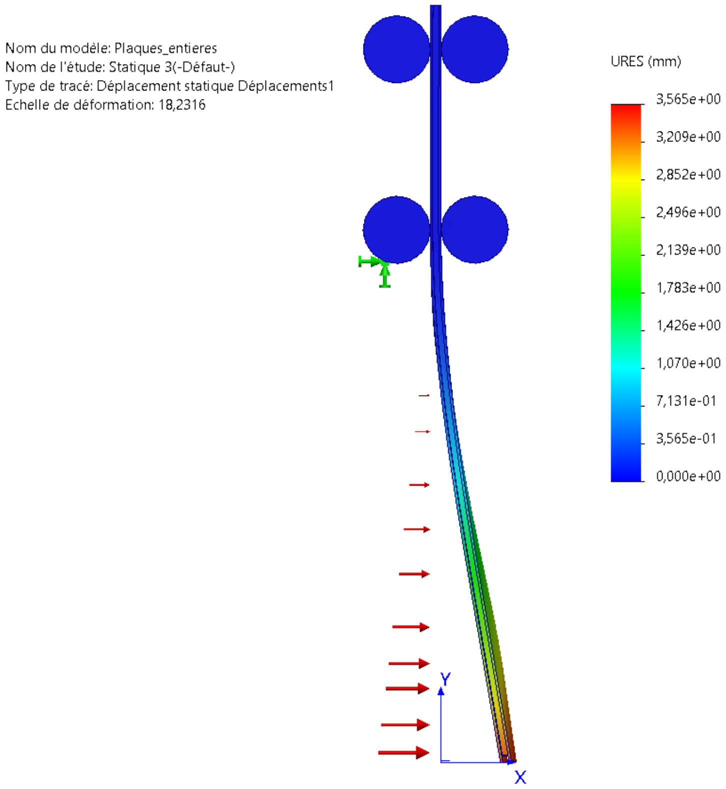

Figure 3.5: Numerical study of the door deflection. Scale of the deformation: 18.2316

4

Final design overview

This chapter describes the whole system as it currently stands on the channel. It should be noted that to achieve this final version of the system, we had to follow an iterative process. In fact, the final design of the mechanism varies slightly from the final 3D version. Indeed, when the system was being assembled, some modifications were made on it. We adjusted the 3D model to fit with the present one on the channel.

After the global overview of the entire system, the mechanism is split into its three main parts to go deeper inside the explanation of all of them and to better understand the mechanical functionalities of the system. The chapter concludes by talking about the slight modifications that were made on the prototype while its assembly.

All dimensions are expressed in millimeters.

4.1 The entire system

In Figure 4.1, the final version of the design of our mechanical system is presented. To explain more specifically the functions of the mechanism, the entire system will be divided in its three main subsystems.

- The railway cart subsystem
- The counterweight subsystem
- The door subsystem

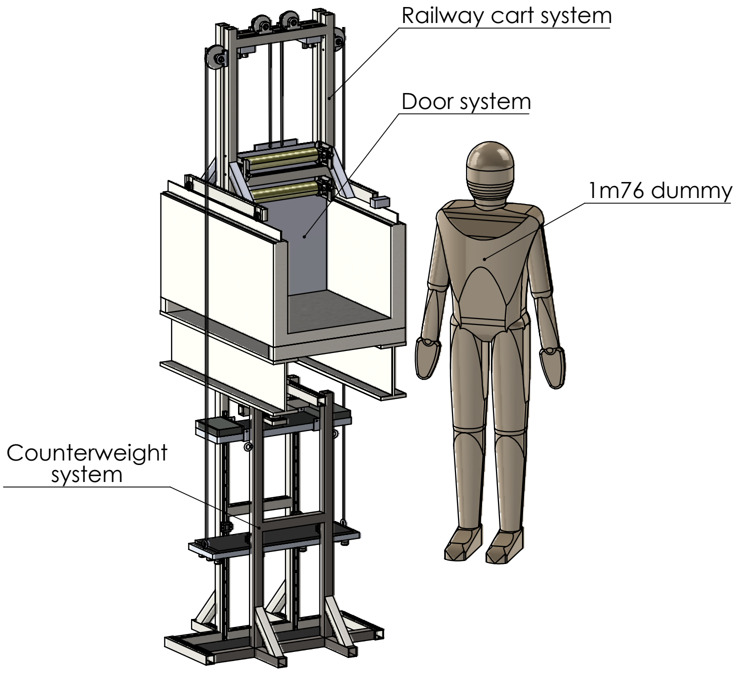

Figure 4.1: Isometric view of the CAD Design. A dummy is presented next to the mechanism to give the reader an quick idea of the dimensions

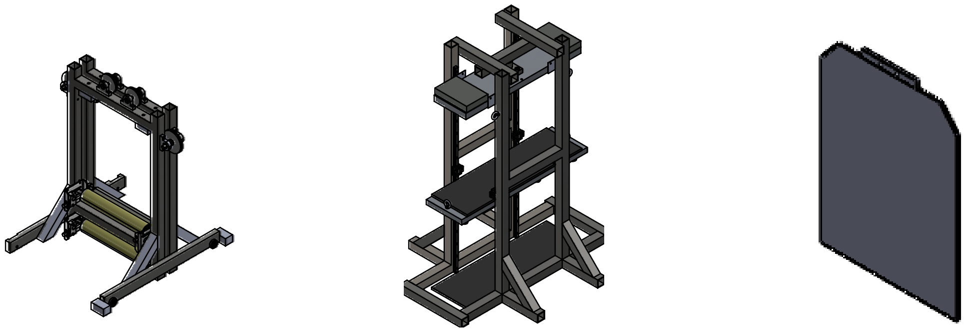

(a) The railway cart subsystem

(b) The counterweight subsystem

(c) The door subsystem

Figure 4.2: The global system is split into three subsystems

What links these 3 subsystems are two 3 mm steel cables of 5 meters each, coated with 2mm of PVC. As the system works in an environment where water projections are frequent, it seemed essential to have a coating around our steel cable to avoid rusting but also to avoid damaging the mechanism pulleys.

Figure 4.3 allows us to have a better comprehension of the main dimensions of the entire design.

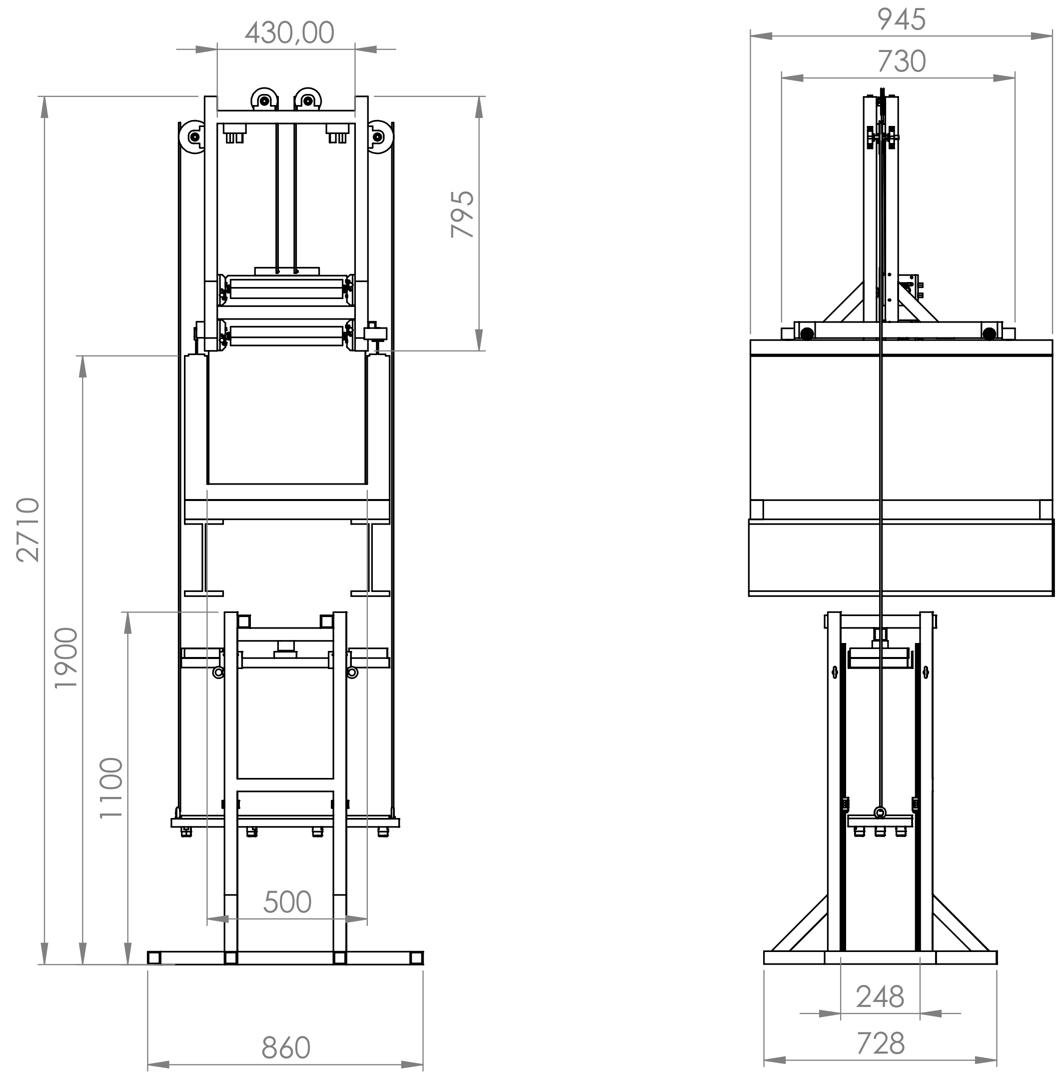

(a) Side view (b) Front view

Figure 4.3: Main views of the design with its main dimensions

The next sections describe each main subsystem with their mains components. For more detailed information on components as their supplier, their supplier references or associated costs, the reader is invited to refer to Appendix D.

4.2 The railway cart subsystem

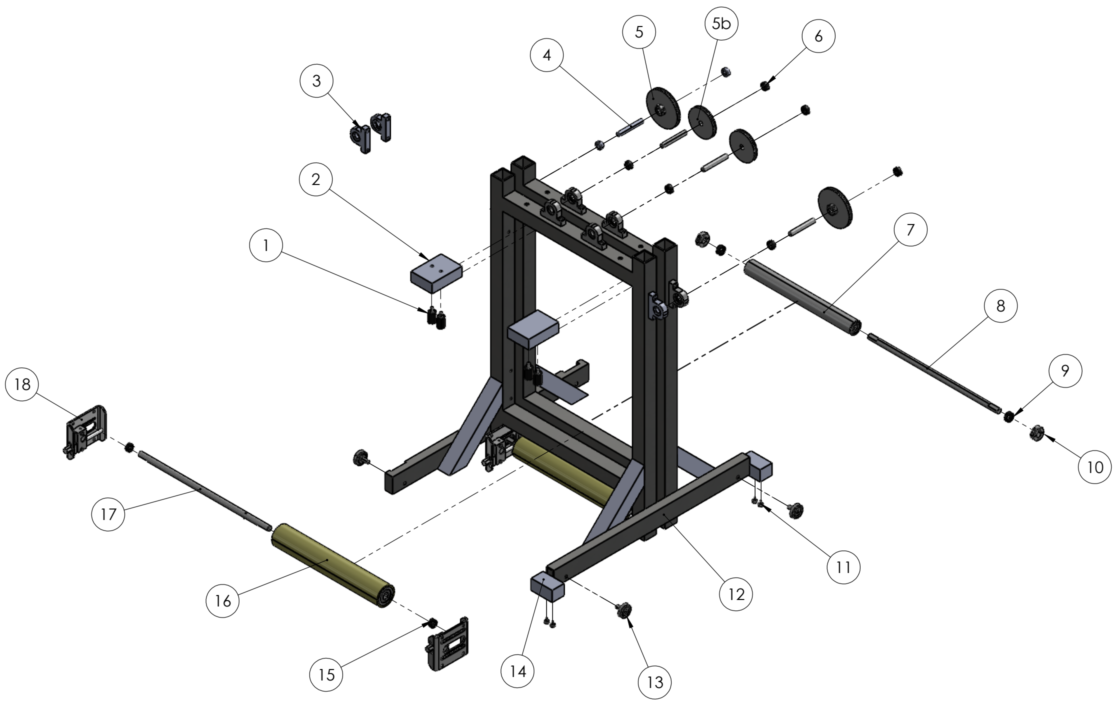

Figure 4.4: Exploded view of the railway subsystem

The structure of the railway cart (12) is made of square hollow section (SHS) steel beams supported by two longitudinal full beams. These beams are painted to make them rust resistant. The cart have several purposes such as guiding the door while it is opening and stopping it when it has reached the top. Then, the cables pulling out the door have also to be guided. Finally, the railway cart should also be able to move along the channel rails.

In order to guide the door, the railway cart is equipped with 4 rollers, two on each side :
The two that are placed upstream have a urethane coating (16) which is a compliant material. This is to avoid jamming or abrasion in the case where some grains would pass between the roller and the door. These rollers are mounted on shafts (17) that are embedded in belt tensioners (18). These are used to tune the advance of the rollers. This adjustability allows a precise positioning of the rollers and ensure tangential contact with the door, thereby achieving effective guidance.
The two rollers that are placed downstream (7) are made of stainless steel and are

held in fixed positions using set collars (10) bolted to the structure.

Once guided, since the door is rising at high speed (see Section 3.6), there is a lot of momentum to dampen. Therefore, polyurethane rubber bumpers (1) are placed in the upper part of the door run. These are screwed in aluminum blocks (2) fixed to the structure.

Guiding the cables from the upper part of the door down to the counterweight placed under the channel is made through pulleys. A cable passes on each side of the channel. Each cable is going through two pulleys with trapezoidal throat, one fixed on the upper part of the structure (5b) and the other one on the side (5). The side pulleys are large enough, allowing the cables to reach the counterweight below.

Finally to move along the channel, the railway cart is equipped with 4 bearings (13) used as wheels. To avoid the railway cart from shifting away from the rails and thus falling down, 4 smaller bearings (11) are screwed vertically in steel blocks (14) placed along one of the rails. These 4 bearings are placed so that the rail passes between them, ensuring a effective guiding of the cart along the whole channel.

4.3 The counterweight subsystem

Firstly, the counterweight structure (24) is entirely made of the same steel beam than the railway cart. The manufacturing drawing of the structure, which includes welding and assembly details, that had been provided to the technicians is available in Appendix E for the reader's reference.

The counterweight system is connected to the other subsystems with the cables being attached to lifting rings (21) which are situated on an aluminum plate (26). This aluminum plate is held only by cables, so it allows the cables to be equally tensioned before being pulled out. The weight of this plate is 9.5 [kg], slightly less the door. Consequently, it ensures that the door cannot be lifted up by weight of the plate alone.

A second aluminum plate, measuring 650x180x30 mm (30) is held in position by an electromagnet (31). The electromagnet was chosen for maintaining and dropping a weight, while remaining at a safe distance from the weights. The latter, being powered by electricity and located under a water channel, is therefore at high risk of being splashed by water. Consequently, an electromagnet meeting IP54[1]

---

[1] An IP54 rating guarantees protection against limited amounts of dust and water sprays from

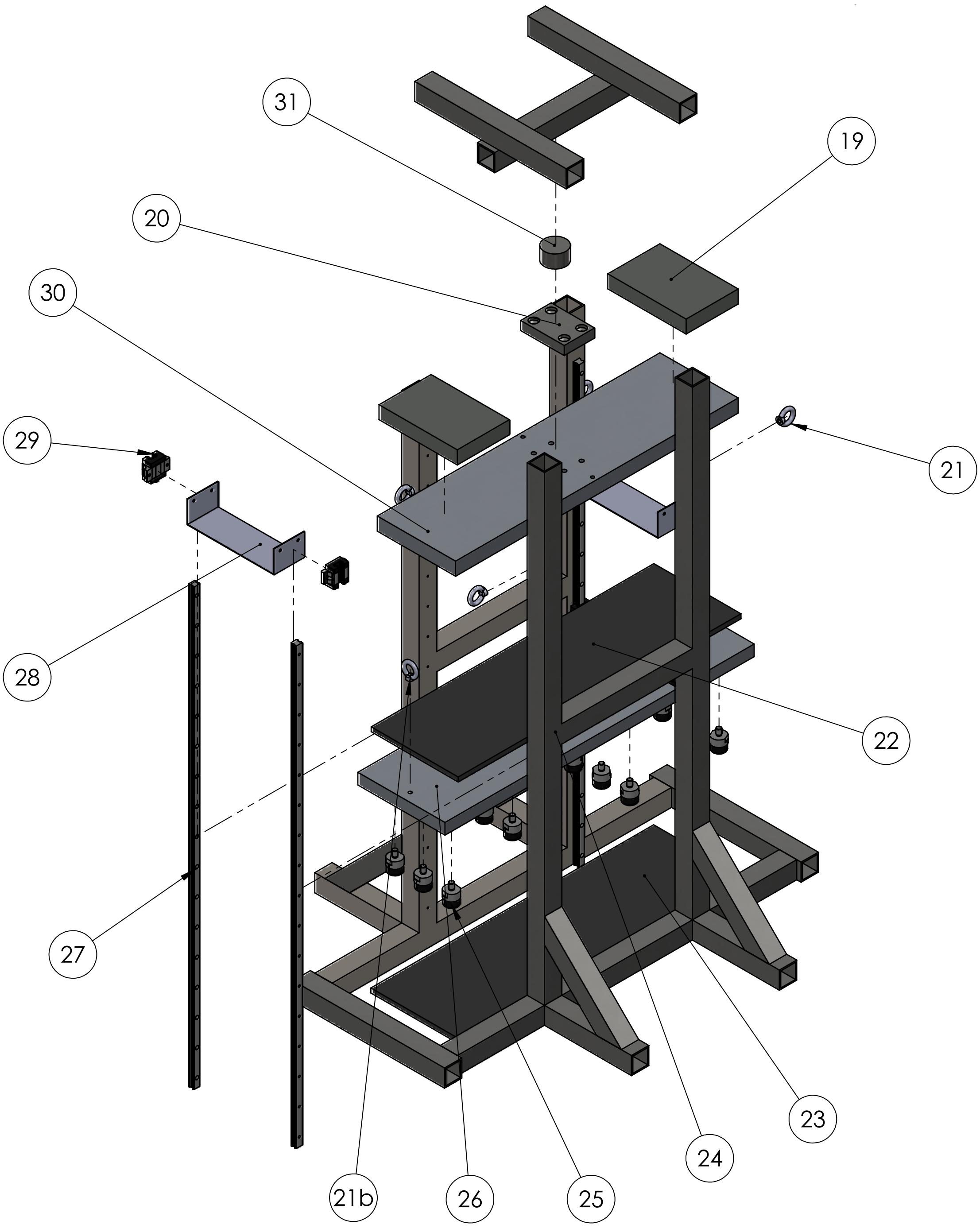

Figure 4.5: Exploded view of the counterweight subsystem

---

all directions.

standards was selected. The plate was also made of aluminum to make it lighter, weighing only about $9.4kg$. A pure steel plate of the same size would have weighed close to 30 kg. Opting for a lighter plate with the ability to add desired weights was preferable over a heavier plate that would limit weights adjustments.

When the electromagnet is deactivated, the plate undergoes free fall and is guided by four vertical carbon steel slides (27). Directly fixing the plate to the skids (29) would have made our system overly constrained. Proper functioning of the slides requires perfect parallel alignment of the latter; otherwise, there is a risk of damage or even breakage, especially during free fall when control of the fall is limited. To provide some flexibility while guiding the weight and to make our system a little more compliant during free fall of this weight, thin 2mm thick stainless steel plates (28) were added. These plates are attached to the skids (29), and it is the skids themselves that are attached to the vertical slides.

After a fall of approximately 45cm, the plate (30) makes contact with the second plate (26) and carries the latter along. A thin rubber sheet (22) is used between the two to avoid excessive noises when the two plates meet.

As the second plate is connected directly to the door with the cables already tensioned, the door can be lifted up directly with the speed acquired during the falling process. The fall is then damped by 12 shock-absorbing and noise-absorbing bumpers (25) and an second rubber sheet (23). The bumpers where selected to carry out the upper limit mass of our system found in Section 3.3.2 and its compression ratio/exerted force graph and its technical data sheet can be found in Figure E.1.

Retaining a plate weighing up to 60kg and dedicated to free-fall solely by means of an electromagnet poses significant risks... Indeed, a power outage or malfunction could unintentionally deactivate the electromagnet, leading to an unplanned plate drop. For this reason, the system includes a safety system using rings (21) to insert steel bars to hold the weights in place if the electromagnet should fail unexpectedly. The safety bars are removed just before turning off the electromagnet.

4.4 The door subsystem

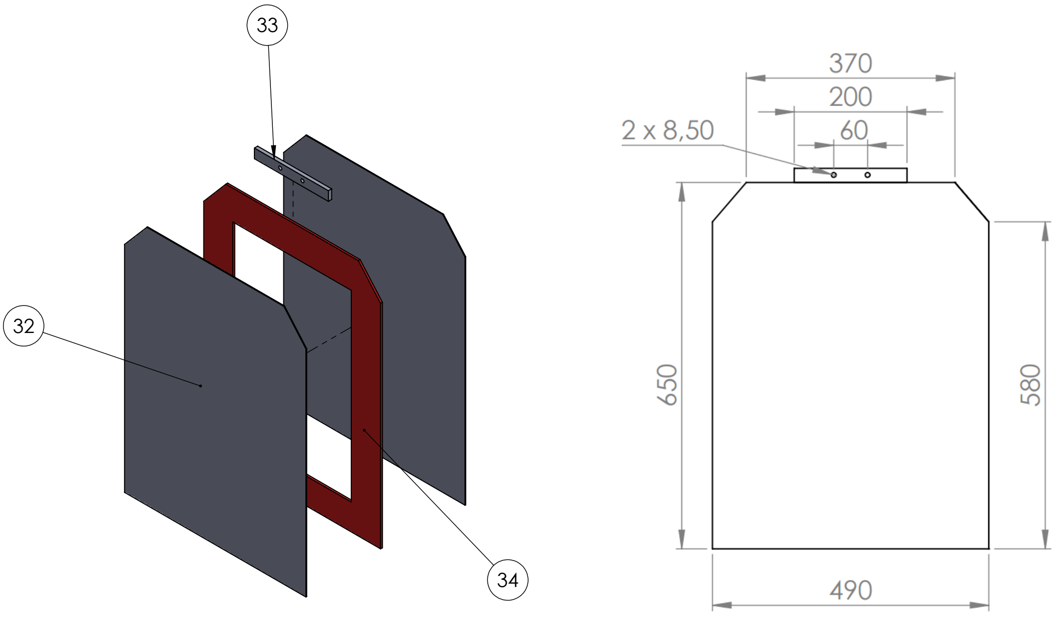

(a) Exploded view (b) Main dimensions

Figure 4.6: Some significant views of the door subsystem

The functioning of the door is quite simple. Its design incorporates features that enable it to withstand the pressure exerted by the water/sand mixture, as illustrated in the earlier figure, while maintaining a relatively high level of water tightness.

The door is made up of two 2mm-thick stainless steel plates (32) and separated with a 5mm-thick Plexiglas plate (34). The addition of the Plexiglas plate increases the overall thickness of the door, and strengthens its resistance to pressure without significantly increasing its weight. The keen reader will have noticed that the width of the channel is 500mm, yet the door is only 490mm wide. Indeed, another crucial component of the door subsystem is the gasket used all around its perimeter to prevent water from passing through. This seal, depicted in Figure 4.7, is made of TPE (Thermoplastic elastomers) and has a hardness of 60 Shore A. Being 6.5mm wide and having a space of 5mm between the door and the wall of the channel, the gasket will have to be compressed by 1.5mm. This is this value that was used for calculations in Section 3.3.2.

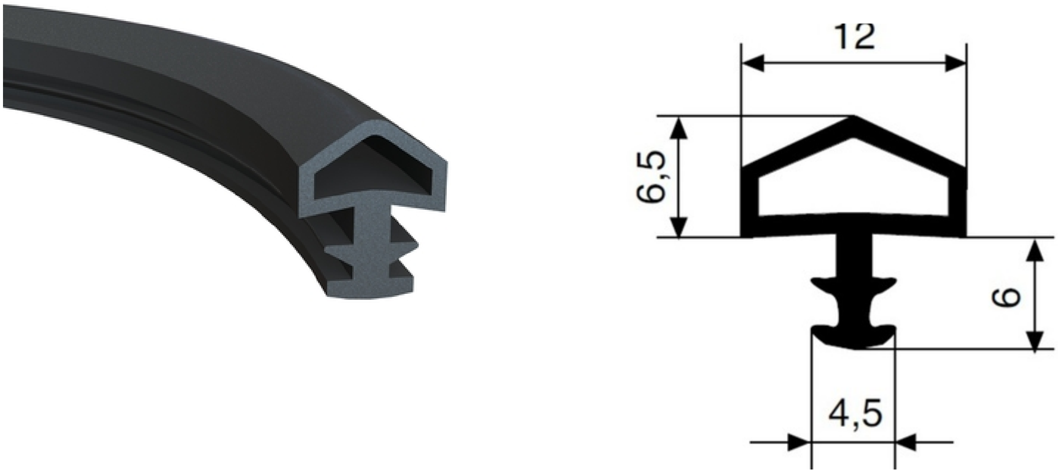

(a) 3D view (b) Main dimensions

Figure 4.7: Gaskets used for sealing the door, from © 2023 ERIKS Belgium

Although the subsystem appears simple at first glance, it has undergone several modifications during the assembly process. One modification involved the inclusion of part (33), which slightly elevates the shackles going into the 8.5mm diameter holes. It allows to prevent them from getting caught with rollers (7) and (16). Furthermore, the corners of the door were trimmed to accommodate the pulleys (5). These adjustments were necessitated by issues encountered during assembly and are deeper detailed in the next section.

4.5 System assembly

Once the design was complete, orders could be placed. A few weeks later, the assembly of the system could begin. The main structures of the railway cart (12) and the counterweight (24) were produced by technicians from the CREDEM laboratory at UCLouvain. The drawings sent to the technicians are available in the Appendix E and the finished structures received can be seen in Figure 4.8. They also made smaller parts such as (28), (30), (20) and (26).


(a) Structure of the railway cart (b) Structure of the counterweight

Figure 4.8: Structures of the system manufactured by the CREDEM technicians.

Once we had received the structures, we personally assembled the various components onto them. During assembly, we had to deal with a few unforeseen problems implying some little adjustments on our design.

For example, we had planned to place the bearings for the external pulleys as shown in Figure 4.9. However, we had not taken into account the thickness of the welds between the two bars, so it was quite complicated to drill holes for the bearing screws at this point.

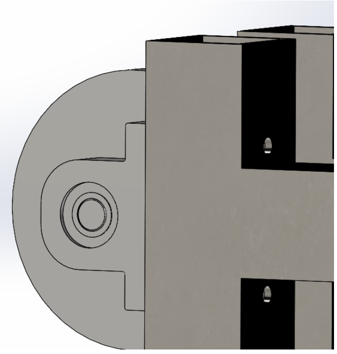
Figure 4.9: Pulley's bearings initial position

We therefore decided to slightly lower the bearings supports, so as not to be bothered by the welds anymore. Since the side pulley's bearings supports were lowered, and therefore the pulleys themselves too, the top corners of the door met the pulleys when the door was raised. We decided to trim them off, as explained in Section 4.4.

A major problem that arose during the assembly and installation of the system was that the rails on which the railway cart was supposed to move were not perfectly straight. We had only measured the spacing between the two rails at 460 [mm]. It turned out that the spacing between the two rails was 460 ± 3 [mm]. In addition, during the manufacture of the railway structure, one of the longitudinal steel spar became slightly deformed due to the excessive concentration of heat during welding, as can be seen in Figure 4.10a. As the longitudinal bars of our cart were supposed to be retracted between the rails, our cart didn't fit onto the rails. The solution was to rework the steel spar, by milling a rectangle on each side of the spar of different thickness due to buckling and re-drill a hole lower down for the bearings. This new configuration will allow the cart to be above the rails rather than between them. This was quite challenging given that the structure was now larger than the milling machine. The reader can refer to Figure F.6 to see the installation made on the milling machine to rework the steel spar. In addition, detailed drawings of the adjustments are also available in Appendix E.

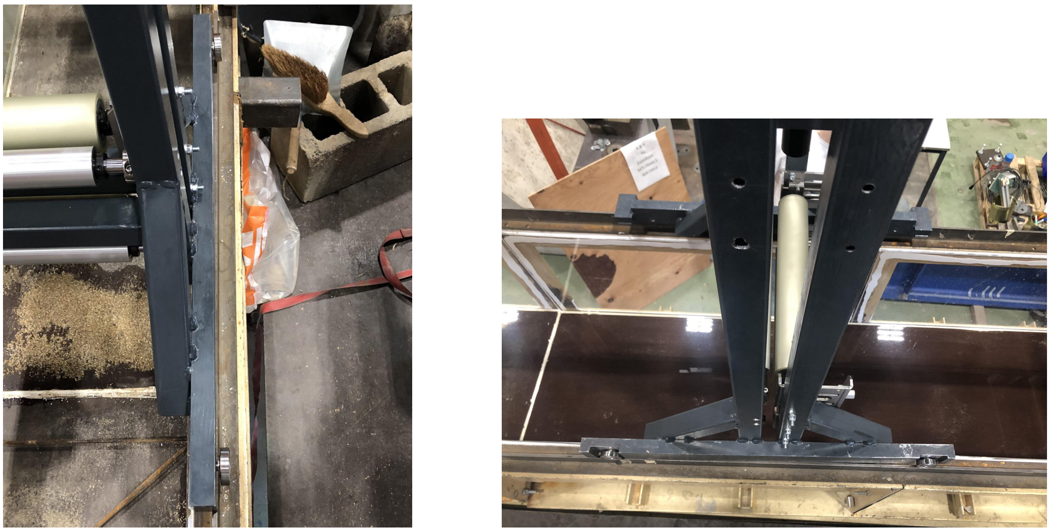

(a) Before adjustments (b) After adjustments

Figure 4.10: Adjustments of the railway cart

The last issue encountered was due to the solution of the rails problems. In fact, as we raised all the trolleys by around 10mm so that they could pass over the rails, the rollers were also raised by 10mm. As a result, the door was not high enough to let the shackles go through. We therefore had to extend the door by adding a part (33). This extension of the door caused a slight buckling of the entire door, again due to the high concentration of heat due to welding.

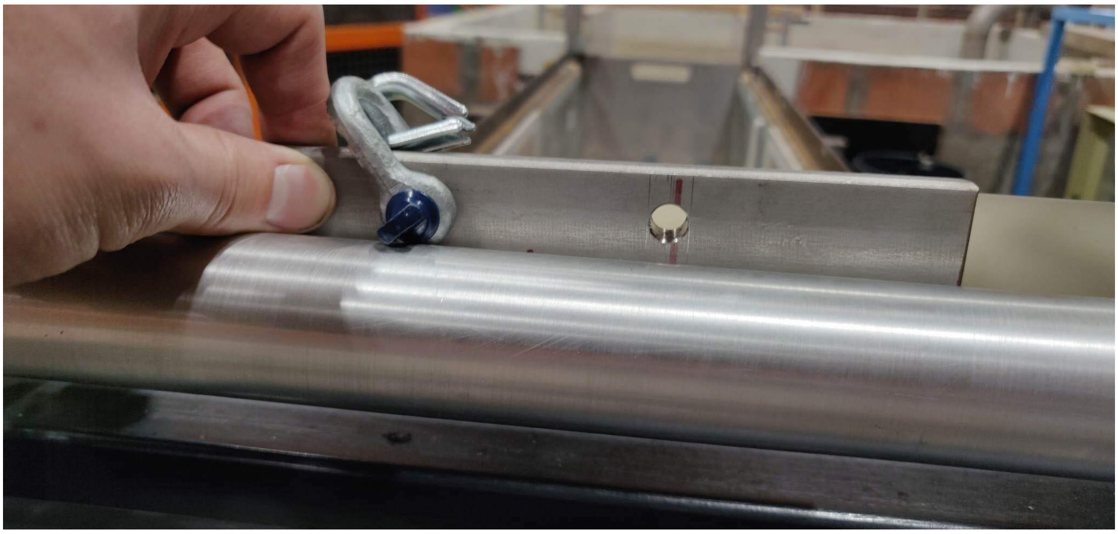

Figure 4.11: Extension of the door to allow the shackles to pass

Finally, all our system was assembled (see Figure 4.12) and ready to be used for experiments on the channel (see Figure 4.13).

(a) The railway cart fully assembled

(b) Bearings of the railway cart

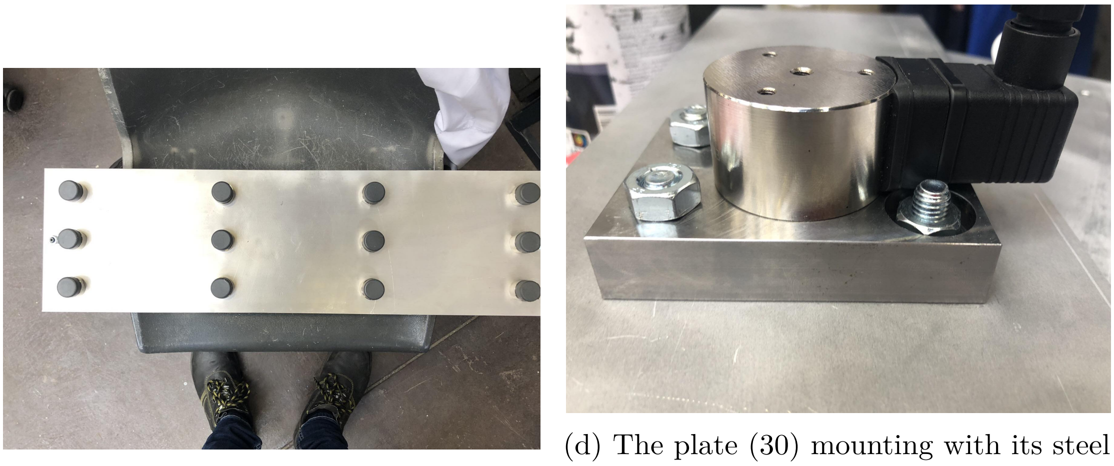

(c) Plate (26) with its 12 dampers

(d) The plate (30) mounting with its steel part (20) for the electromagnet (31)

Figure 4.12: Some parts assembly of the system

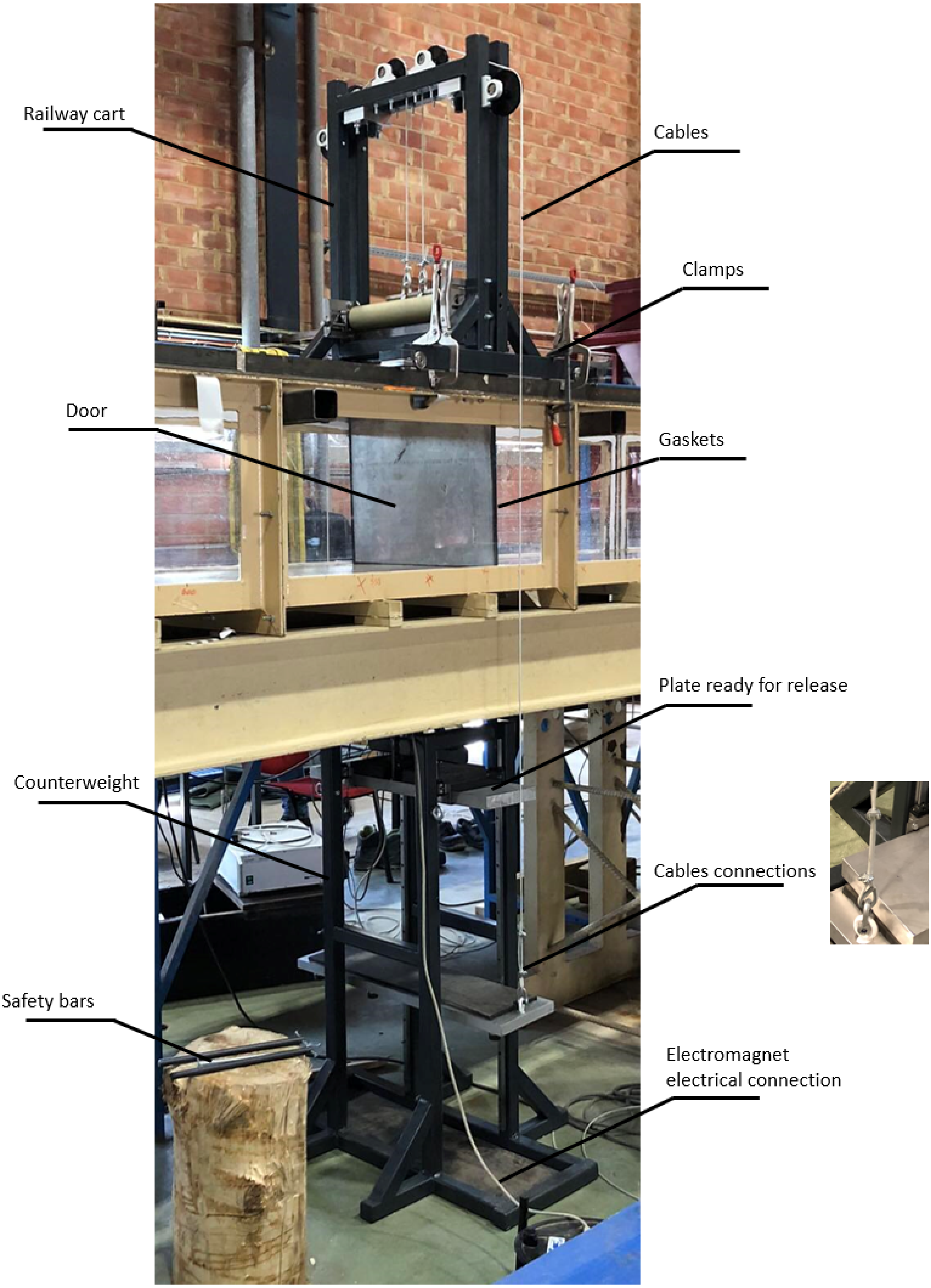

Figure 4.13: Final system on the channel

(a) $t = 0s$, electromagnet disconnected

(b) $t = 0.13s$, free-fall

(c) $t = 0.26s$, free-fall

(d) $t = 0.36s$, collision and door lifts up

(e) $t = 0.45s$, door lifting up

(f) $t = 0.53s$, door lifting up

(g) $t = 0.67s$, slight bump

(h) $t = 0.89s$, system at rest

Figure 4.14: Time evolution of the system in use

4.6 System enhancements

Although our system is currently operational for conducting experiments on the channel, the following section outlines potential improvements. These enhancements are not essential for the functionality of the mechanism but aim to improve the overall user experience.

4.6.1 Counterweight subsystem improvements

Currently, the railway cart moves along the channel. However, as the cables are connected directly to the counterweight, we have to move the counterweight by hand at the same time as the cart. That requires the work of two people and it might be interesting to consider integrating some kinds of retractable wheels to the counterweight structure. This would enable simultaneous movement of the counterweight and the cart by a single person.

In addition, the incorporation of adjustable feet on the counterweights could enable the system to be leveled everywhere.

For instance, the *MPlate Type Castors with Adjuster TCALZ Series* from MISUMI could be a potential solution. Indeed, it may serve as a suitable solution that addresses both enhancements in a single component.

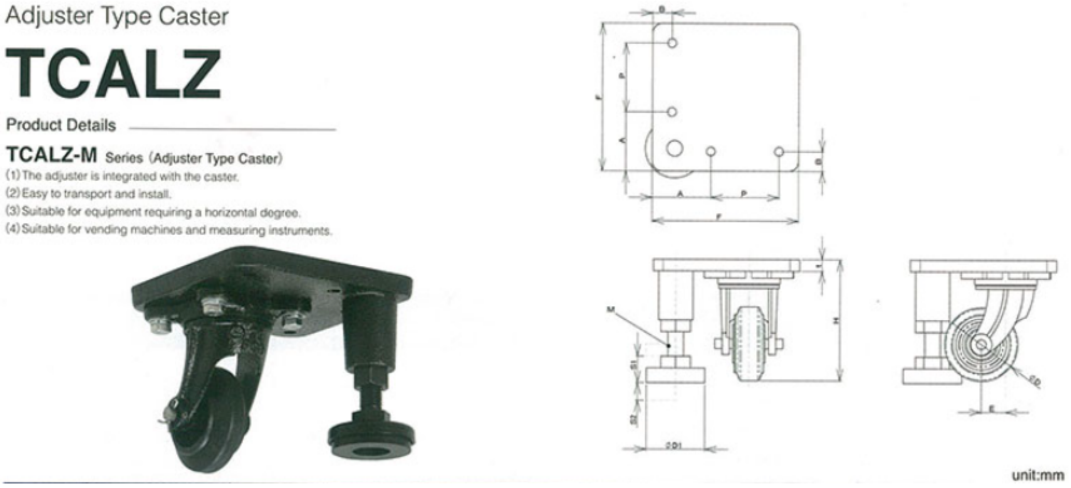
Adjuster Type Caster

TCALZ

Product Details

TCALZ-M Series (Adjuster Type Caster)
(1) The adjuster is integrated with the caster.
(2) Easy to transport and install.
(3) Suitable for equipment requiring a horizontal degree.
(4) Suitable for vending machines and measuring instruments.

Figure 4.15: Plate Type Castors with Adjuster TCALZ Series @MISUMI

4.6.2 Guiding improvements

When using our system to conduct experiments which required the use of sand, we realized that a small amount of sand can occasionally adhere to the door and potentially pass through the rollers. Although the rollers are designed to withstand such deformations caused by grains of sand, it might be worth considering the installation of a brush just below the rollers. This brush would serve to clean the door by removing any unintended grains of sand.

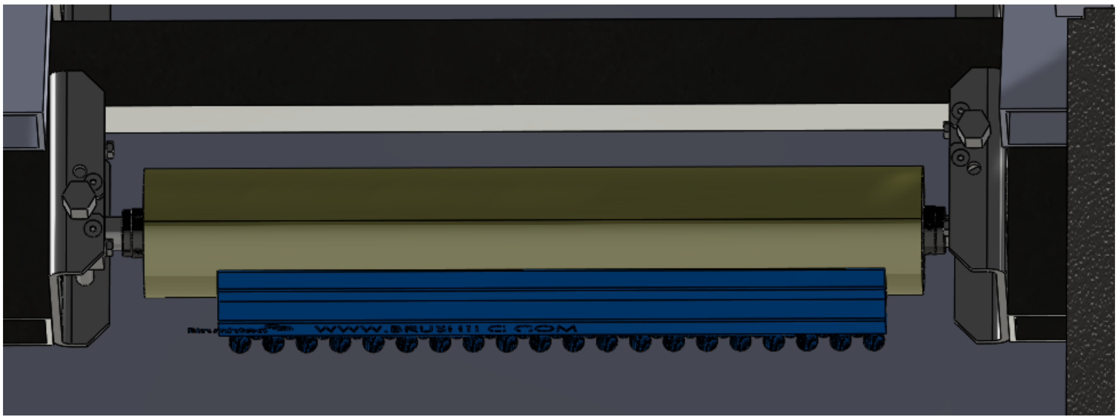

Figure 4.16: Example of brush below the rollers, brush from @BRUSHTEC

4.6.3 Integrated Clamping system

As can be seen in Figure 4.13, the railway cart is currently maintained on the canal with external clamps. It would be a great improvement to include a fixing system directly on the railway cart.

5

Validation of the mechanism

In this chapter, the focus is on validating our mechanism by taking a close look at its characteristics in relation to its initial specifications. Our approach involves an assessment of its main functionalities to ensure they align with the intended ones. Additionally, its compliance with the imposed constraints is evaluated.

5.1 Overall verification

To briefly recall, our system had to open and close a door on a channel and this door had to be properly guided. It also had to be able to move along the channel and ensure a certain degree of watertightness.

Firstly, to open and close the door, a vertical lifting mechanism was implemented using cables and pulleys connected to a counterweight located beneath the channel.

Secondly, to ensure proper guidance, the door is equipped with a pair of stainless steel rollers and a pair of adjustable urethane rollers. The adjustability of the latter pair allows for the precise positioning of the rollers and thus to ensure tangential contact with the door, thereby achieving effective guidance.

Regarding watertightness, the door exhibits satisfactory sealing along its perimeter. However, there are identified weak points at the bottom corners, which can be easily addressed by incorporating tape or suitable plugs to enhance the door's water resistance.

The system is mounted on a set of bearings that enable longitudinal movement along the channel rails. This allows the system to move along the channel and to position the door with a certain degree of mobility.

Furthermore, the system adheres to the constraints imposed. In fact, our system fits perfectly with the dimensions of the channel and demonstrated the ability to withstand water pressure during the experimental tests that were performed in Section 5.4. To prevent rusting, the pure steel components of the mechanism have been adequately coated with paint. Despite operating in a sandy environment, the selection of parts such as of urethane rollers has been specifically chose to avoid interference from sand particles.

In terms of budget, the overall cost of the mechanism, including VAT, amounted to approximately 2200€. The majority (almost 85%) was allocated to orders from the supplier MISUMI. It provided us with a significant proportion of the mechanical components required for the system, including rollers, shafts, slides, and more. Approximately 10% of the budget was attributed to orders from ERIKS and RS-Component. ERIKS supplied the seals, while RS-Component provided the electromagnet. The remaining 5% of the budget was dedicated to orders placed with Lemmens for all the necessary wiring such as shackles, lugs, cables and cable ties. Note that it does not include the time taken by CREDEM technicians to manufacture the parts. Manufacturing such parts in private companies would considerably increase the costs.

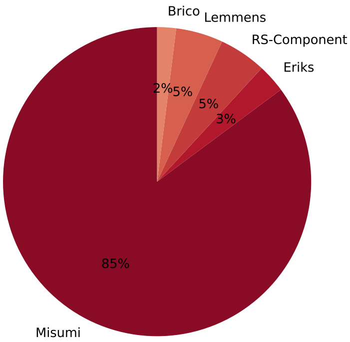

Figure 5.1: Cost distribution

Moreover, it is important to notice that the entire mechanism passed a risk analysis by the "Service de sécurité et de radioprotection" (SERP) of UCLouvain. The result is that the latter conforms to current prototype safety standards.

In the subsequent sections, a series of tests were conducted to thoroughly validate the functionalities and performances of our system.

5.2 Opening time

In order to respect the initial condition of the column, the door opening should be considered instantaneous. To do so, Lauber and Hager [55] defined a criterion that defines the maximal opening time in order to preserve the instantaneousness condition for water column.

$$t_{op} < \sqrt{\frac{2h_0}{g}} \tag{5.1}$$

with g = gravitational acceleration, h_0 = reservoir depth and t_{op} = opening time. During our experiments, the lowest water depth we used was : $h_0 = 330$ [mm] (height of the sand column + water), then

$$t_{op} < 0.259[s]$$

Using 15 videos we computed a mean value for the opening time :

$$\bar{t}_{op} = 0.200335 \pm 0.014[s]$$

Which means that for any configurations, the door opening time respect the condition of instantaneousness.

5.3 Free surface

As we said in Section 2.1.1, one significant drawback of the lowering system was the free surface. In order to investigate the impact of the door opening on the water level, a specific experiment was conducted. In the study conducted by Flora [6], the analysis focused on observing the water level variation across the entire channel but only for a limited duration of 7 time steps.
In our case, we aimed to put a strong focus on the time variation of the water level. To achieve this, we examined the water level variations in range between 45 seconds before the door opening and 100 seconds thereafter to observe any stabilization of the water surface.

For this purpose, we worked with BAUMER probes. These probes, when they are properly calibrated, allow us to measure the height of the water level. However, our primary interest lies in the variation of the water level rather than its absolute height.
For our experiment, we used three BAUMER probes strategically placed at locations within the channel where we anticipated significant variations. The following table provides the sensor labels and their corresponding positions in the channel.

Label	Distance of the sensor w.r.t the door [m]
SONDE 1	$x = -0.12$
SONDE 2	$x = 0.12$
SONDE 3	$x = 1.20$

Table 5.1: Labels of the BAUMER sensors with their distance w.r.t the door. x is the axis along the length of the channel, pointing downstream of the water flow.

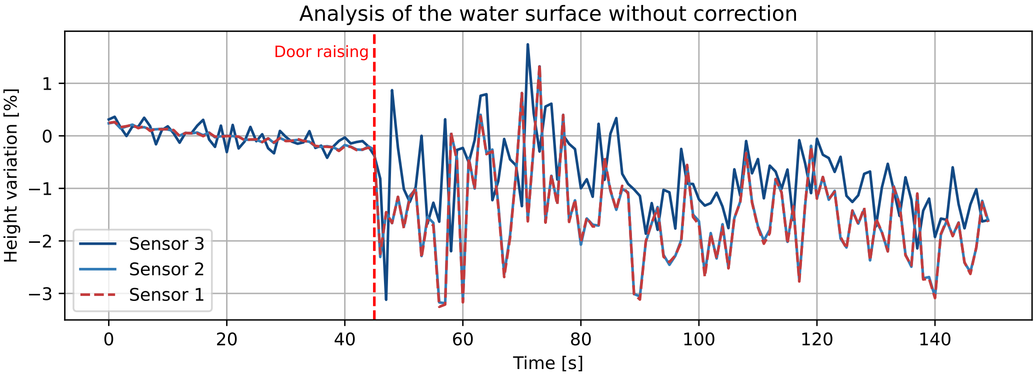

Figure 5.2: Time height variation of the water level due to the door opening

That means that the "Sonde 1" is located over the sand column before the door, the "Sonde 2" is located just after the door and the last "Sonde 3" is far downstream.

In Figure 5.2, we can firstly observe that the variations of the water level near the door are identical. Moreover, the water level is nearly constant before the door opening. The variation of the water height of the surface is between 1.7% and −3.1%.
Although we assume that the mean water level was constant all over the channel, we clearly observe the decrease of the mean water level due to a outgoing flow. The latter can be measured through the BAUMER probe and we measured approximately a out mass flow rate of $\dot{m}_{out} \approx 0.8[l/s]$. Knowing the volume of the water after the door, we can approximate the variation of height of the water due to this outgoing flow:

$$\Delta h = \frac{\dot{m}_{out}}{L \times l} \tag{5.2}$$

Where $L = 3.15[m]$ is the length of the channel after the door and $l = 0.5[m]$ its width. We finally compute a $\Delta h \approx 0.5[mm/s]$.
We can now used this value to estimate the variation of the water level taking into account the water flow going out of the channel. The results can be observe in Figure 5.3.
Using the corrected level of water, we clearly observe that the mean water level stays constant. The variation of the water height of the surface is now between ±2.5%.

To have a better understanding of the data obtained in the experiment, a bode diagram of the data obtained by the SONDE 3 is presented in Figure 5.4.

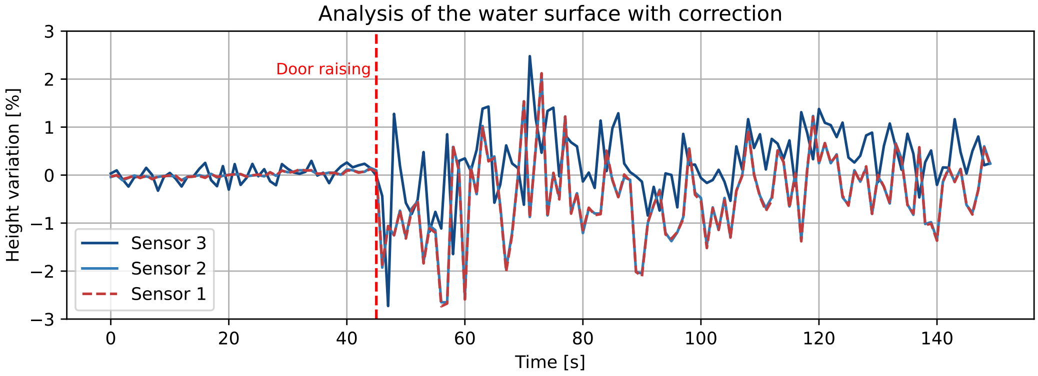

Figure 5.3: Time height variation of the water level due to the door opening, corrected with the water flow rate

It will allow us to highlight the most important frequencies through their amplitudes.

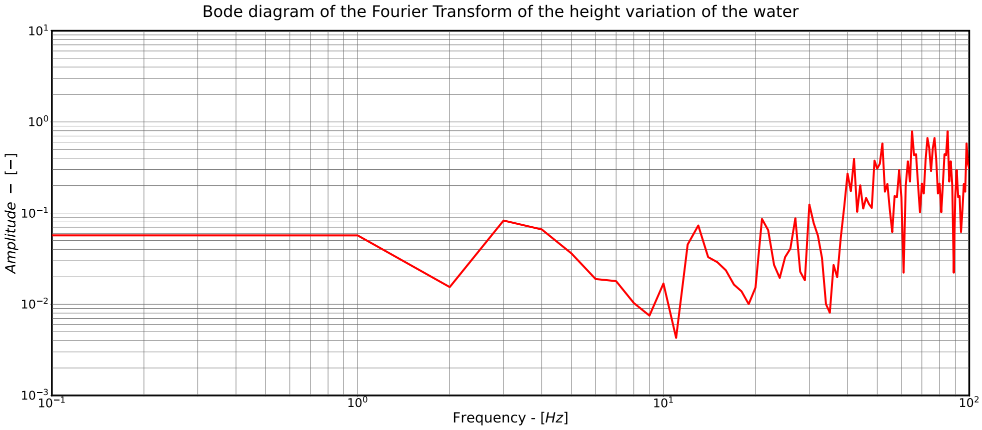

Figure 5.4: Bode diagram of the height variation of the water level due to the door opening, corrected with the water flow rate

We observe that higher frequencies are well observed in the data, meaning that we have a lot of small waves with little period, and the data do not indicate a lot of "big waves".

5.4 Door deflection

Simulations were performed on the door to estimate its deformation depending on the hydrostatic pressure that will be exerted on it in Section 3.3.3. To confirm this, we decided to performed some tests to experimentally estimate this deflection. Results are available in Figure 5.5.

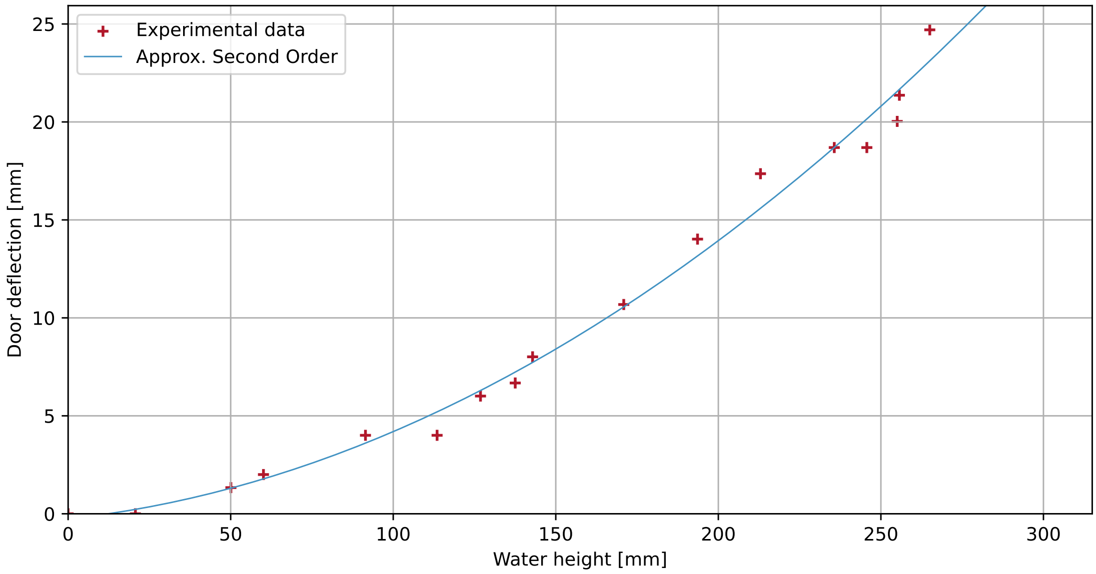

Figure 5.5: Experimental data of the deflection of the door

We directly observe that the deflection is far greater than the one expected with the simulation. We can assume that these differences are due to the fact that the door's integrity has been compromised due to deformations resulting from the welding of its extension. The result is an initial deflection and also a reduction in its resistance to water pressure. However, the system has been designed to facilitate the easy interchangeability of the door with another unit. We can also assume that the waves coming from the quick filling of the channel during the tests exerted additional forces on the door.

We observe that the relation between the deflection and the water height can be approximated with a second degree function. That comes from the fact that the deflection seems to be linearly proportional to the force, as shown with Figure F.7 and that the force is proportional to the square of the water height.

The first part of this master's thesis has been successfully accomplished. Having designed a mechanical system for the experimental study of the collapse of a granular column in water at rest and validate it, our focus will now shift to use this system for conducting the experiments.

This page is intentionally left blank.

Part II

Experimental analysis of the collapse of a granular column in water at rest

6

Theoretical model

To further compare our experimental results, we use a numerical simulation model developed by the Institute of Mechanics, Materials and Civil Engineering, which is described in detail in Monsorno et al. [63]. Although the model has already been validated by comparing it to theoretical and experimental cases [64] [38], this thesis aims to provide a new testing configuration for the model and contributes to the validation and the evaluation of the reliability and accuracy of the model by providing experimental data.

6.1 Description

Since this thesis is focused on testing the model by providing and expanding the experimental database and not on the numerical implementation of the model, the focus is not on detailed explanations of the latter. Its description and operation will be quite concise and brief.

All symbols used within the theoretical model are listed in Table 6.1, by order of apparition.

Firstly, we consider a two-phase mixture (liquid and solid) consisting of a granular material and a carrier fluid, like water in our experiments. The Figure 6.1 shows briefly the context situation of the mixture of these two phases.

ϕ_α	Volume fraction of the phase $\alpha(\alpha = f, s)$
$\boldsymbol{u}_\alpha$	Velocity field of the phase $\alpha(\alpha = f, s)$
ρ_α	Density of the phase $\alpha(\alpha = f, s)$
$\boldsymbol{f}$	Interphasial momentum exchange
δ	Drag coefficient
$\boldsymbol{g}$	Constant of gravitational acceleration
$\mathbf{\Pi}_\alpha$	Stress tensor of the phase $\alpha(\alpha = f, s)$
p_α	Pressure field of the phase $\alpha(\alpha = f, s)$
$\boldsymbol{I}$	Identity tensor
$\boldsymbol{T}_\alpha$	Viscous-stress tensor of the phase $\alpha(\alpha = f, s)$
ζ_α	Bulk viscosity of the phase $\alpha(\alpha = f, s)$
$\mathbf{V}_\alpha$	Strain rate tensor of the phase $\alpha(\alpha = f, s)$
$\mathbf{V}^{\mathrm{d}}_\alpha$	Deviatoric component of $mathbfV_\alpha$
$\boldsymbol{C}_s$	Elastic stress due to the microstructure of the system
χs	nonlinear parameters describing the non-Newtonian rheology of the solid phase
Re	Reynolds number of the flow
μ_c	Transport coeffficient
β_s	Inter-granular stress

Table 6.1: List of symbols used within the theoretical model

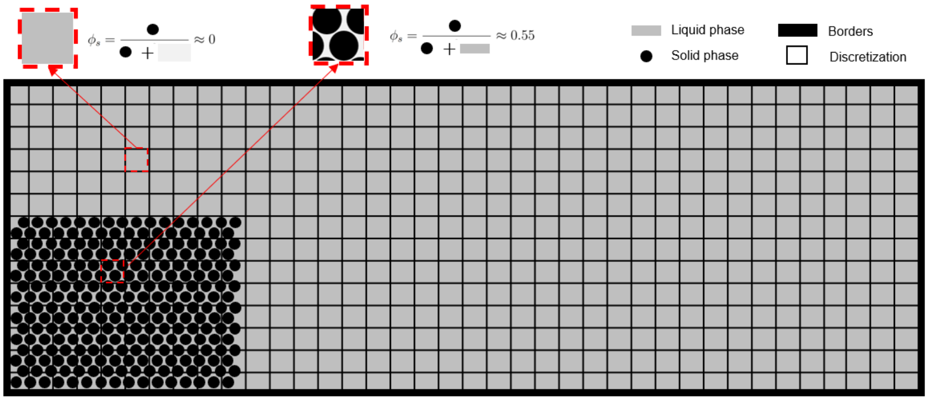

Figure 6.1: Example of the two phases, the channel has been discretized in squares for a better understanding

The main assumptions are listed hereunder:

1. Each phase is treated as a thermodynamic continuum with its own set of governing equations;
2. The two continua are immiscible but the mixture is saturated, meaning that

we have a saturation condition

$$\phi_s + \phi_f = 1 \tag{6.1}$$

3. The granular material is isotropic and the fluid is Newtonian;
4. The two continua are open to each other and not in equilibrium;
5. Both phases have constant density

Bold characters represent tensor of first order and uppercase bold characters represent tensor of second order. $\boldsymbol{u}_\alpha$ represents the velocity field of the α-phase. Each phase must satisfy the NAVIER-STOKES equations, i,e the time-dependent continuity equations for conservation of mass, momentum and energy.

Fluid phase

$$\frac{\partial \phi_f}{\partial t} + \phi_f \nabla \cdot \boldsymbol{u}_f = 0 \tag{6.2}$$

$$\rho_f \frac{\partial \phi_f \boldsymbol{u}_f}{\partial t} + \rho_f \phi_f \nabla \cdot (\boldsymbol{u}_f \otimes \boldsymbol{u}_f) = \nabla \cdot \boldsymbol{\Pi}_f - \boldsymbol{f} + \rho_f \phi_f \boldsymbol{g} \tag{6.3}$$

As mentioned before, the fluid is supposed to be Newtonian, meaning that the viscous stresses arising from its flow are at each point linearly correlated to the local strain rate. Hence the stress tensor of the fluid phase can be writen as the sum of only two contributions; the static pressure p_f and the viscous stresses, i.e.

$$\boldsymbol{\Pi}_\mathrm{f} = -p_\mathrm{f}\phi_\mathrm{f}\boldsymbol{I} + \boldsymbol{T}_\mathrm{f} \tag{6.4}$$

For isotropic fluids, the viscous-stress tensor $\boldsymbol{T}_\mathrm{f}$ can be decomposed as the sum of a diagonal and a deviatoric component, i.e:

$$\mathbf{T}_f = \phi_f \zeta_f \left(\nabla \cdot \boldsymbol{u}_f\right) \mathbf{I} + 2\phi_f \mu_f \mathbf{V}_f^\mathrm{d} \tag{6.5}$$

where $\mathbf{V}_f^\mathrm{d}$ is the deviatoric component of the strain rate tensor $\mathbf{V}_f = \frac{1}{2}\left(\nabla \boldsymbol{u}_\mathrm{f} + (\nabla \boldsymbol{u}_\mathrm{f})^\top\right)$. The deviatoric part can also be expressed as $\mathbf{V}_f^\mathrm{d} = \mathbf{V}_f - \frac{2}{3}\left(\nabla \cdot \boldsymbol{u}_f\right)\mathbf{I}$.

Furthermore, in Equation 6.3, $\boldsymbol{f} = \boldsymbol{f}_f = -\boldsymbol{f}_s$ represents the interphasial momentum exchange. It is composed of a non-dissipative and a dissipative component:

$$\boldsymbol{f} = p_f \nabla \phi_s + \delta(\mathbf{u}_f - \mathbf{u}_s) \tag{6.6}$$

where δ is the drag coefficient. A correlation for this term has been proposed in Benyahia *et al.* (2006)[65]

$$\delta = 12 \frac{(1-\phi_s)^2}{Re} F \tag{6.7}$$

where F is the dimensionless drag force.

Solid phase

$$\frac{\partial \phi_s}{\partial t} + \phi_s \nabla \cdot \boldsymbol{u}_s = 0 \tag{6.8}$$

$$\rho_s \frac{\partial \phi_s \boldsymbol{u}_s}{\partial t} + \rho_f \phi_s \nabla \cdot (\boldsymbol{u}_s \otimes \boldsymbol{u}_s) = \nabla \cdot \boldsymbol{\Pi}_s + \boldsymbol{f} + \rho_s \phi_s \boldsymbol{g} \tag{6.9}$$

Unlike the fluid phase, the stress tensor of the solid (or granular) phase can be modeled as the sum of three contributions: the static pressure p_s, an additional elastic stress due to the microstructure of the system $\boldsymbol{C}_\mathrm{s}$ and finally the viscous-stress tensor $\boldsymbol{T}_\mathrm{s}$, to restate:

$$\boldsymbol{\Pi}_\mathrm{s} = -\phi_\mathrm{s} p_\mathrm{s} I + C_\mathrm{s} + \boldsymbol{T}_\mathrm{s} \tag{6.10}$$

C_s is defined, according to Monsorno *et al* (2017)[63] and Papalexandris (2004) [66], as

$$\mathbf{C}_s = \gamma_s \nabla \phi_s \otimes \nabla \phi_s, \tag{6.11}$$

This term describes the stresses due to variations in the density of the contact area between grains. Since it depends on the distribution of grains in space, it is also sometimes referred to in the literature as the "configuration stress tensor".
The coefficient γ_s accounts for the spatial distribution of the grains and is thus dependant on ϕ_s. We notice that relevant discussions about these parameters can be found in various sources [66] [67] [68] [69]. Compared to the viscous stresses of the liquid phase, the solid phase is characterized by non-Newtonian rheology. Its viscous stresses are nonlinear with respect to the deformation tensor. Monsorno *et al* (2017)[63] proposed the following equation to model these stresses:

$$\mathbf{T}_s = \left(\left(\zeta_{s1} + \zeta_{s2}\right) \nabla \cdot \boldsymbol{u}_s + \chi_1\right) \phi_s \mathbf{I} + 2\left(\mu_{s1} + \mu_{s2}\right) \phi_s \mathbf{V}_s^\mathrm{d} + \chi_2 \phi_s \mathbf{V}_s \cdot \mathbf{V}_s \tag{6.12}$$

In the previous relation, we can dissociate the coefficients that are independent of the strain rate and the dependent ones. Firstly we have for the independent ones the coefficients μ_{s1} and ζ_{s1}. Those are respectively equivalent to the shear and bulk viscosity similarly as μ_f and ζ_f expressed in the fluid phase.
For those that depend on the strain rate, i.e. $\mu_{s2}, \zeta_{s2}, \chi_1$ and χ_2. All these parameters describe the non-Newtonian rheology of the solid phase, are nonlinear and are given by

$$\mu_\mathrm{s2} = \frac{\mu_\mathrm{n}}{\sqrt{2}} \frac{\det \mathbf{V}_s}{\left(\mathbf{V}_s : \mathbf{V}_s\right)^{\frac{3}{2}}}, \quad \zeta_\mathrm{s2} = \frac{\mu_\mathrm{n}\sqrt{2}}{3} \frac{\det \mathbf{V}_s}{\left(\mathbf{V}_s : \mathbf{V}_s\right)^{\frac{3}{2}}} \tag{6.13}$$

and

$$\chi_1 = -\sqrt{2}\mu_\mathrm{n}\left(2\sqrt{\mathbf{V}_s^\mathrm{d} : \mathbf{V}_s^\mathrm{d}} - \frac{3}{2}\frac{\mathbf{V}_s^\mathrm{d} : \mathbf{V}_s^\mathrm{d}}{\sqrt{\mathbf{V}_s : \mathbf{V}_s}}\right), \quad \chi_2 = -\frac{\sqrt{2}\mu_\mathrm{n}}{\sqrt{\mathbf{V}_s : \mathbf{V}_s}} \tag{6.14}$$

Compaction equation

Finally to close the system of balance laws, we need to introduce the compaction equation. According to Monsorno *et al*[63], the volume fraction ϕ_s satisfies the following temporal evolution equation, also called the compaction equation,

$$\frac{\partial \phi_s}{\partial t} + \boldsymbol{u}_s \cdot \nabla \phi_s = \mathrm{Re}\, \frac{\phi_s \phi_f}{\mu_c} \left(p_s - p_f - \beta_s + \nabla \cdot (\gamma_s \nabla \phi_s) \right). \tag{6.15}$$

In the context of the granular phase, this equation serves as the particle-migration model. The parameter μ_c acts as a transport coefficient which quantifies the dissipative relaxation resulting from compaction of the solid phase. The granular phase's microstructure is described by γ_s, which was previously mentioned, and β_s. Specifically, β_s. is known as the inter-granular stress and represents the grains' ability to resist compaction.
The correlation used for β_s is of empirical nature. An expression for this correlation has been proposed in Powers *et al.* (1989)[70] and is given by

$$\beta_s(\phi_s) = \pi \frac{\phi_s^2}{\phi_{s_0}^2} \frac{(2-\phi_{s_0})^2}{(2-\phi_s)^2} \frac{\ln\left[\frac{1}{1-\phi_s}\right]}{\ln\left[\frac{1}{1-\phi_{s_0}}\right]} \tag{6.16}$$

where ϕ_{s_0} is the initial fraction volume.

6.2 Numerical implementation

To solve the preceding equations a numerical algorithm has been developed by Professor Papalexandris with his research team [5][38]. It is based on a predictor-corrector time integration scheme. This kind of algorithm is specifically designed to integrate ordinary differential equations by finding an unknown function that satisfies a given ordinary differential equation. This integration scheme is coupled with a generalized projection method for the pressure state of each phase as we can observe in Monsorno*et al* (2018)[5]. The projection method was firstly introduced by Chorin [71].
The projection method used with the equations considered above leads to a second order elliptic equation for the pressure of each phase. Moreover, the algorithm uses a finite-volume discretization of governing equations in a collocated grid. The algorithm is implemented in a 3D parallel code written in C/C++ [38].

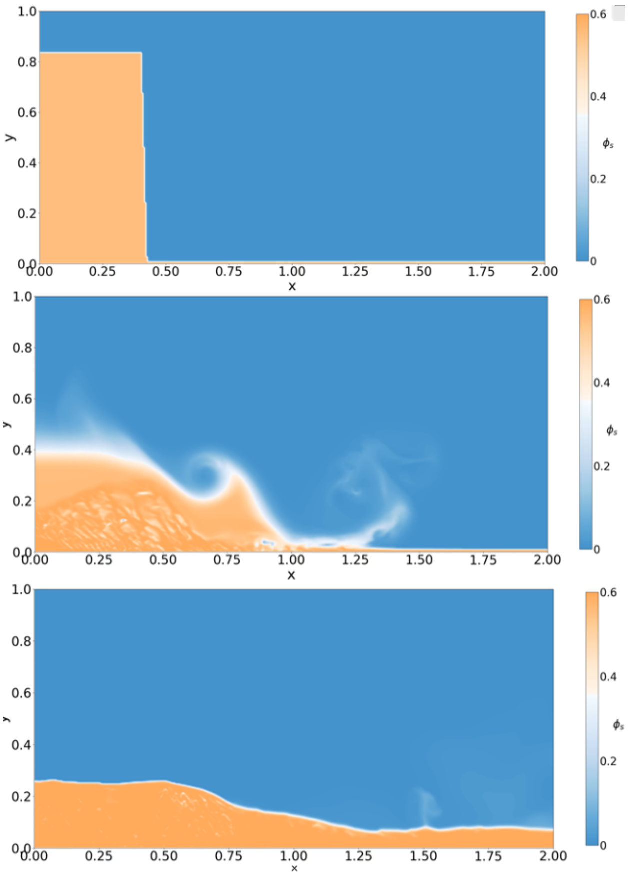

Figure 6.2: Example of results obtained using the algorithm. ϕ_s is the volume fraction.

An example of the results obtained through this numerical implementation of the model is showcased below.

The subsequent part of this thesis will be to compare the results given by the model described hereabove (and its numerical solving algorithm) with our experimental data. To achieve this, we will used the mechanism designed in Part I.

7

Relevant parameters

This chapter summaries the parameters influencing the collapse behaviors of granular media. It allows a better understanding of their behaviors and sets the scene for the parametric study of the next chapter.

7.1 Aspect Ratio

The aspect ratio of a column is defined as the ratio of its initial height divided by its initial length. This parameter is then directly linked to the column dimensions.

$$a = \frac{H_i}{L_i} \tag{7.1}$$

Lube *et al.* made some experiments on the collapse of a dry granular column [40] and they observed that the aspect ratio had an strong influence on the flow behavior.

In Figure 7.1 they observed that for low values of a, only the edges of the initial column are in motion, whereas for larger a the entire surface slips from the beginning. This means that the aspect ratio will influence the position of the initial failure surface. The grains will slip down along the latter and below the particles will remain static. The aspect ratio also has and influence on the the maximum dimensionless runout distance L_∞ and the final deposit height H_f at x=0. L_i = initial basal length, H_i = initial column height and $\delta L = L_f - L_i$

In Figure 7.2, one can observe that the higher aspect ratio is, the longer the runout distance will be. In Figure 7.3, the longer the runout distance of the column, the lower the maximum height of the final deposits.

Rondon *et al.* [43] observed that for a submerged granular column, the aspect ratio and the initial volume fraction (see Section 7.2) had an impact on the shape

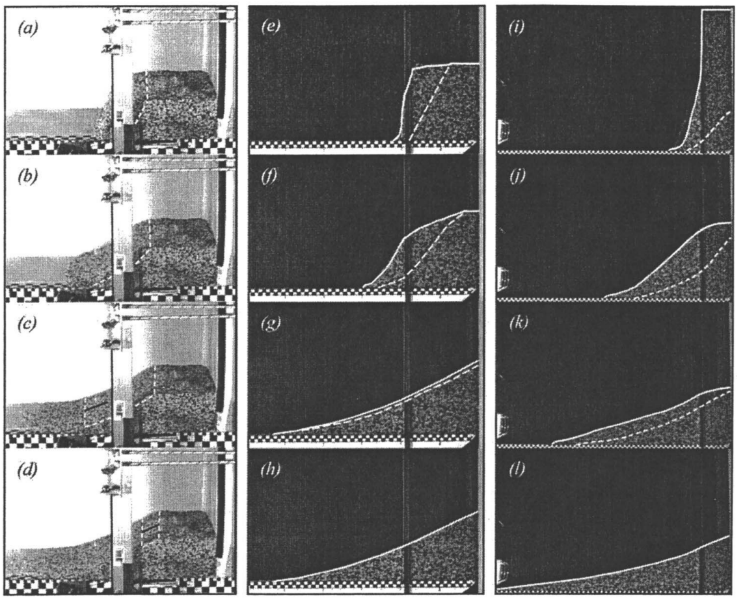

Figure 7.1: Flow evolution at different times for experiments with a= 0.5 (a)–(d), a= 1.5 (e)–(h), and a= 7 (i)–(l). The dashed curves mark the position of the interface between static and moving particles, whereas the solid curve highlights the upper free surface, from Huppert and Lube 2005 [40]

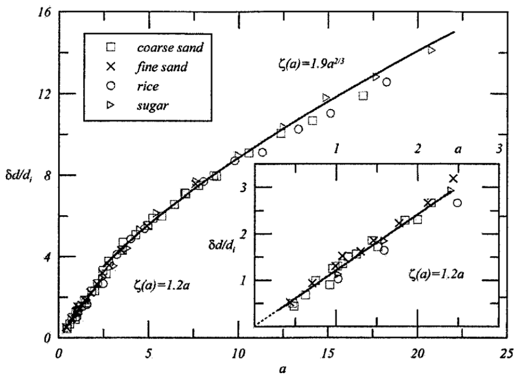

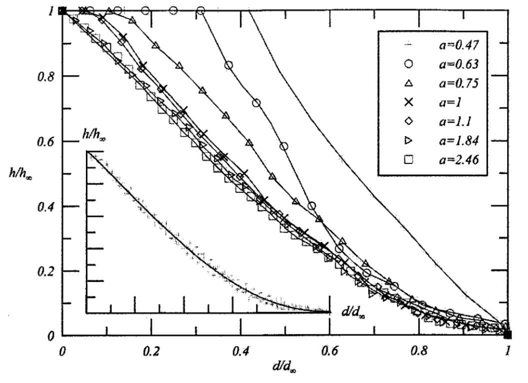

Figure 7.2: The nondimensional incremental runout distance, $\delta d/d_i$ (equivalent to $\delta L/L_i$ here), as a function of the aspect ratio [40]

Figure 7.3: The nondimensional height of the final deposits as a function of nondimensional distance for a<2.5 ($h/h_\infty = H/H_f$; $d/d_\infty = L/L_f$).[40]

of the final deposits and the dynamic of the collapse. Thompson and Huppert [41] found that the surrounding fluid did not influence significantly the final runout distance and height compared to the dry case but had an impact on flow dynamics.

In their works, Lee *et al.* [44] highlighted the existence of a critical aspect ratio a_L. From this one, the initial failure surface is so deeply buried down in the column that the entire upper portion of the column descends at the initial stage of the collapse process. This causes the granular material in the lower portion of the column to slide forward down along a smaller failure surface.

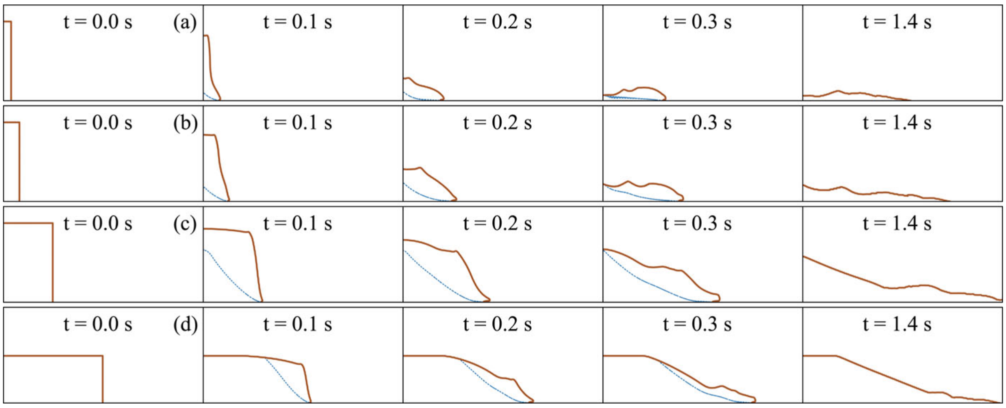

Figure 7.4: Collapses of submerged granular columns for the coarse particles with (a) $A = 10$ ($L_i = 1cm$ and $H_i = 10cm$), (b) $A = 5$ ($L_i = 2cm$ and $H_i = 10cm$), (c) $A = 1.67$ ($Li = 6cm$ and $Hi = 10cm$), and (d) $A = 0.5$ ($L_i = 12cm$ and $H_i = 6cm$). The red solid lines are the contour lines of $c = 0.5$. The blue dashed lines are the failure surface defined by $|u_1| = 5cm/s$. The final deposit morphology is a “Mexican hat” for (a), a triangle [(b) and (c)], or a trapezoid (d).[44]

In their numerical results they found that $A_L = 3$ for coarse particles (d =0.56[mm]). In Figure 7.4, we see that we have well critical aspect ratio $a \geq A_L$ for (a) and (b).

7.2 Volume fraction

The volume fraction ϕ is defined as the ratio of V_{grains}, the volume of granular matter (without interstitial spaces), divided by V_{bulk}, the total bulk volume of the immersed granular column.

$$\phi = \frac{V_{grains}}{V_{bulk}}$$

The volume fraction represents the concentration of sand in the column. Rondon *et al.*[43] used glass beads of density $\rho = 2500[kg/m^3]$ and $\overline{d} = 225[\mu m]$ in mean diameter. They determined two types of granular columns : loose and dense.
Loose columns had a volume fraction of $\phi_{s,i} = 0.55$ and dense had $\phi_{s,i} = 0.60$.
For each, they observed radically different collapse behaviors. In Figure 7.5, we can see that the loose column falls almost instantly and has a large runout distance compared to the dense one (twice longer). We can also observe that the whole column collapses at the same time. The final deposits shape have a triangle shape. The dense column, has a significantly larger collapse time and smaller runout distance. We observe a different dynamic of the collapse. Initially, only the right

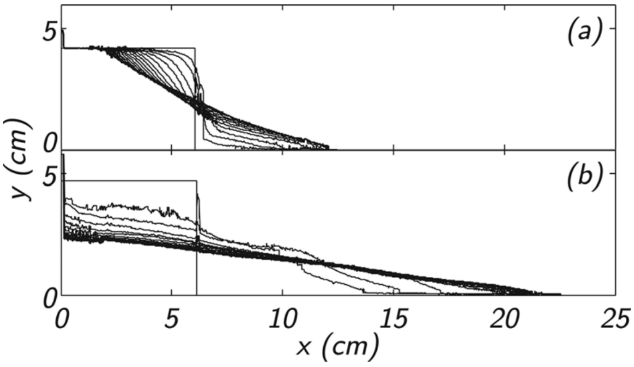

Figure 7.5: Collapse of a dense and a loose column containing the same amount of sand for an aspect ratio $A \simeq 0.67$. $(a)\phi_i = 0.60$, $L_i = 6cm$, $H_i = 4.2cm$, $3s$ between profiles; $(b)\phi_i = 0.55$, $L_i = 6cm$, $H_i = 4.8cm$, $0.66s$ between profiles.[43]

upper corner starts to collapse and, over time, the collapsing will spread to the left. The final deposit morphology has a trapezoidal shape.
The volume fraction has then an influence on the final deposits shape, the collapse time and the dynamic of the spreading.

7.3 Shape and size of the sand grains

The shape and size of the grains have an impact on the collapse of the granular column. Cabrera and Estrada[72] have shown that under a certain value of the initial length to grain mean diameter ratio $\frac{R_0}{\overline{d}}$, the runout distance depends much more on the grain size. The Figure 7.6 clearly shows this influence of the grains size compared to the system size. In other words, in order to avoid grain-size effects, the initial column's length L_i must be larger than a certain number of grains diameters. Hereunder, the runout distance L_∞ is defined as:

$$L_\infty = \frac{L_f - L_i}{L_i} \tag{7.2}$$

As shown on Figure 7.6, the threshold for tall columns is at $R_0/\overline{d} = L_i/\overline{d} = 50$ and for short or larger columns is at $R_0/\overline{d} = L_i/\overline{d} = 75$.

Lee *et al.*[44] compared the collapse of coarse particles ($d_{50} = 0.56[mm]^1$) and very fine particles ($d_{50} = 0.12[mm]$) using glass beads. They found that the spreading velocity and runout distance for the very fine particles were larger than those for coarse particles.When the final deposits shape is trapezoidal, the collapse duration for the very fine particles is the same as the one for the coarse particles. This conclusion can be also be observed in the experimental work of Bourgouin *et al.*[73]

---

[1] d_{50} stand for the media diamter whereas *overlined* stand for the mean diameter.

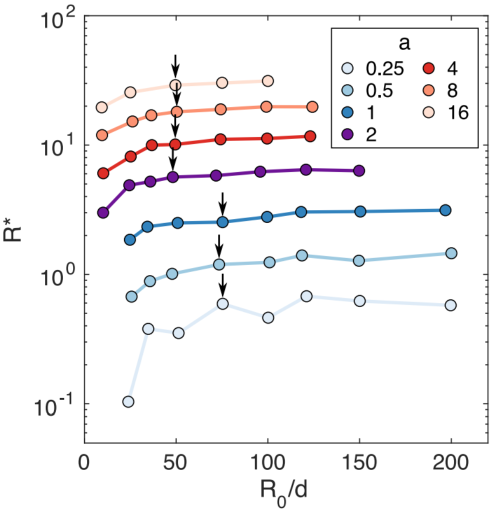

Figure 7.6: Column mobility R^* $(= L_\infty)$ as a function of the system-size to grain-size ratio $R_0/overlined$ $(= L_i/overlined)$and the initial aspect ratio a.[72]

in Figure 7.7

But all these papers use glass beads as particles. In reality, sand particles have multiple sizes and shapes. We know from Jian Chen [74] that "the strength of a granular assembly is basically a result of the competition between rolling and sliding of the particles in a granular matrix: For round particles, even large coefficients of friction will not be able to stabilize a granular structure against disintegrating by relative rolling at inter-particle contacts". Since in our case sand is used, we will observe a different behavior from the one of the glass beads that are all perfectly round and with the same size. To characterize our sand studies are conducted to determine its median and mean diameter in Section 8.4.

7.4 Flow regimes

Bourgouin and Lacaze [75] investigated effect of a surrounding fluid on the collapse feature of a granular column. They based their work on the conclusion of Courrech du Pont *et al.* [47], that the granular fluid flow can be decomposed in three different regimes (free fall, viscous, and inertial) for the case of rotating-drum configuration. These regimes were shown to depend on two dimensionless numbers, the Stokes number St and the grain-fluid density ratio r.

$$St = \frac{1}{18\sqrt{2}} \frac{(\rho_s \cdot \Delta\rho \cdot g \cdot d^3)^{1/2}}{\mu_f}, \quad r = \left(\frac{\rho_s}{\rho_f}\right)^{1/2} \tag{7.3}$$

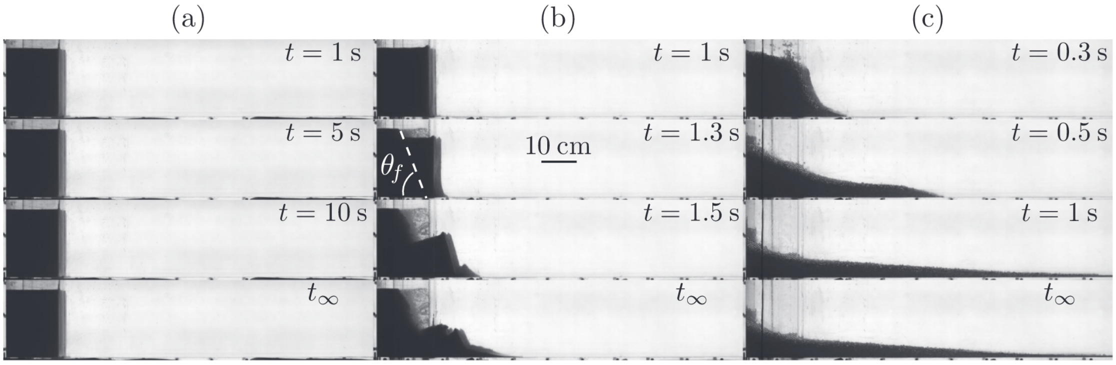

Figure 7.7: Snapshots of some water-saturated granular collapses for various grain diameters: (a) $d = 120\mu m$, (b) $d = 500\mu m$, and (c) $d = 5mm$. In Fig. 2(b), the failure angle f with respect to the horizontal plane is indicated. In all cases, the initial aspect ratio is $a \approx 1.3$ and the initial volume fraction is $\phi \approx 0.64$ (i.e., initially densely packed).[73]

with ρ_s = the solid phase (sand) density, g = gravitational acceleration, d = diameter of a particle and μ_f = the viscosity of the fluid.
Bourgouin and Lacaze [75] determined then the three regimes based on the dynamic of a single sand grain :

- **The free fall regime :** For $St \gg 1$ and $r \gg 1$, the surrounding fluid has no effect on the dynamics of the granular collapse and this is the free-fall regime, which is commonly associated with dry conditions.
- **The inertial regime :**For $St \gg 1$ and $r \ll 1$, the gravitational force acting on the grain is counteracted by the drag force from the fluid. This leads to the grain reaching its inertial limit velocity and is therefore associated with the inertial regime. It is important to note that the term "inertial regime" refers to the dominant influence of fluid inertia on the dynamics, distinct from the inertia of the grains themselves.
- **The viscous regime :** For $St \ll 1$, , the impact of viscous effects becomes significant and the grain reaches its Stokes limit velocity[2]. This regime is thus referred to the viscous regime.

In our case,

$$St = 1.18 \text{ and, } r = 1.62 \text{ for grains with } \overline{d} = 0.275\text{mm}$$

---

[2] The Stokes limit velocity or terminal velocity is the velocity a particle reaches when the drag force induced by friction with the fluid is equal to the gravity force that drives this particle.

$$St = 13.28 \text{ and, } r = 1.64 \text{ for grains with } \overline{d} = 1.363\text{mm}$$

For the thinner sand we will be in the inertial regime but, with a value close to 1, we could have some viscous effects that come into play.
For the coarser sand we will stay in the inertial regime.
One can note that the shape of the final deposits depends on both the aspect ratio a and the considered regime with St and r.

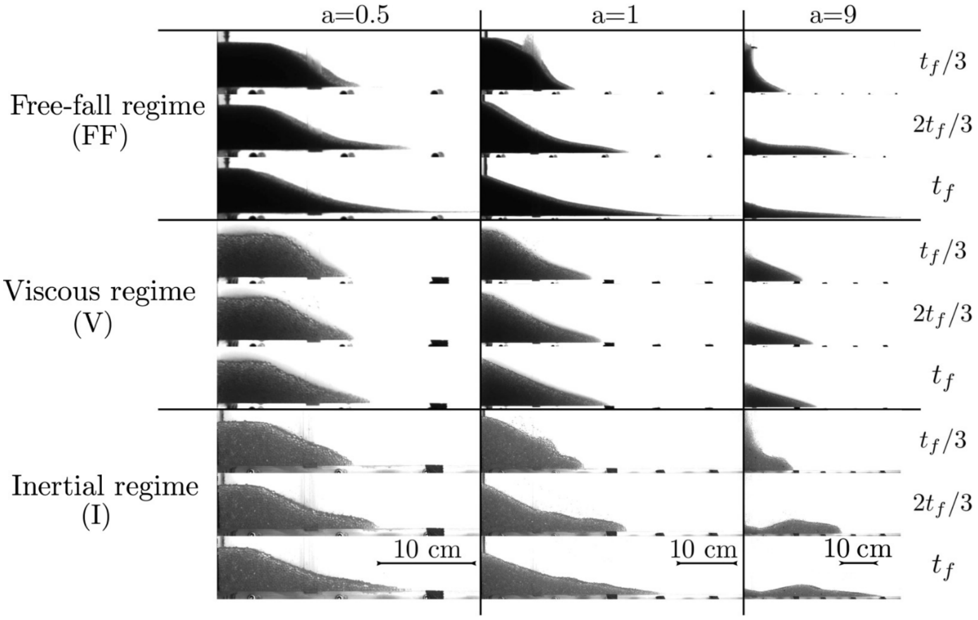

Figure 7.8: Snapshots of the granular collapse for regime FF, regime V, and regime I for three different aspect ratios and at three different times.[75]

Mutabaruka [31] demonstrated the importance of distinct analyses for the collapse and spreading phases in particle dynamics. During the collapse phase, particles gain kinetic energies, while in the spreading phase, the energy acquired in the previous phase determines their distance and stopping time. The fluid's role differs in each phase: in the first phase, it dissipates a portion of the energy, whereas in the second phase, it acts as a partial lubricant for the contacts, thereby mitigating the dissipative impact of drag forces. Topin *et al.* have made the same observations [76].

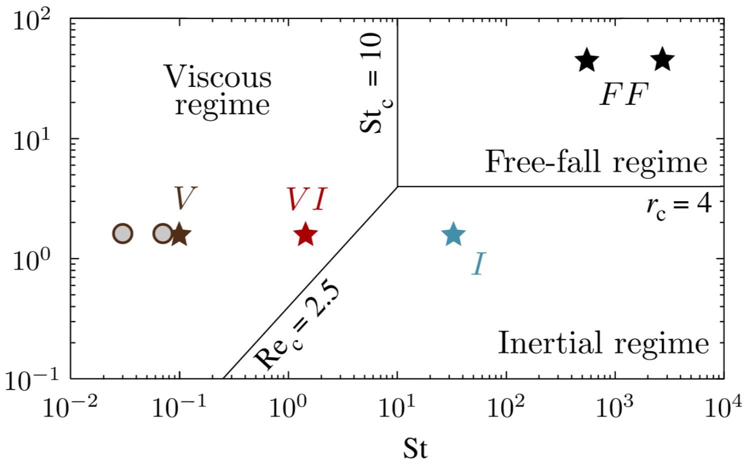

Figure 7.9: Granular-fluid flow regimes in the (St,r) plane. Stars and circles correspond to the experimental series performed in 7.8. [75]

8

Experimental setup

This chapter focuses on the comprehensive examination of the experimental system. It begins with a global overview followed by demonstrating the repeatability of the experiments. It presents the images processing methods used. Furthermore, the chapter includes a characterization of the different types of sand used through grain size analysis. Lastly, the chapter explores the limitations of the system.

8.1 Overview and General Information

8.1.1 Setup

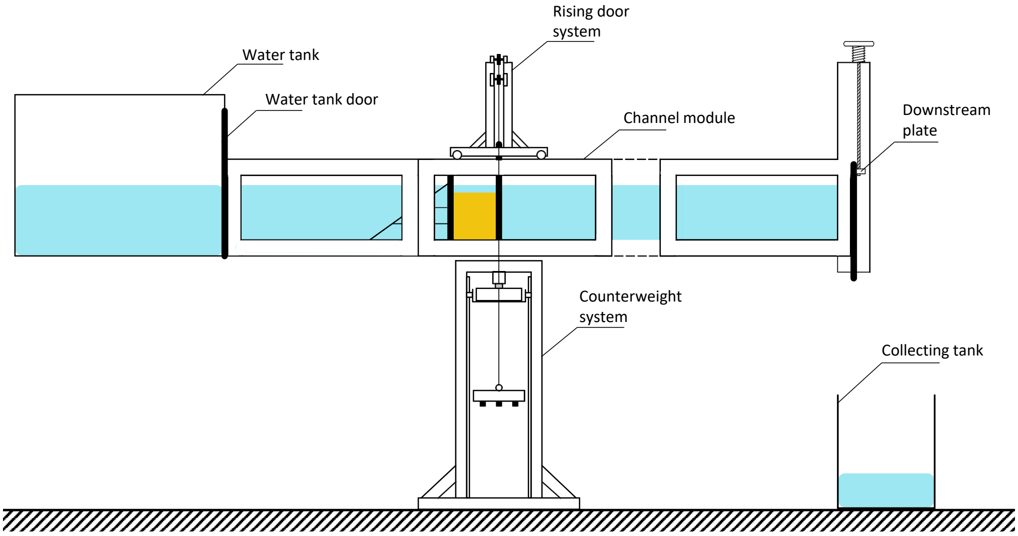

Figure 8.1: Experimental setup scheme

As shown in Figure 8.1, the experiments take place in a horizontal channel placed at 1.50 m over the ground. The channel is 7,6 m long and has a rectangular cross-section of 0.40 m high and 0.50 m wide. The x direction is along the flow , y is vertical and z is spanwise. Upstream, there is a water tank with a vertical door. Once this door is raised we can fill up the channel with water. Downstream, a plate is fixed and is only movable along the y-axis. When it is down, the channel is open and the water is free to flow and when the plate is up, the channel is closed. We use this configuration to fill up the channel and to keep the water at rest inside. The channel is composed of 8 modules that are 0.945 m long. These are made of a metal frame with an internal Plexiglas walls allowing to observe the inner part of the channel. Each transparent window is 0.33 meter high and 0.825 meter long. The opening door is placed on top of one of these module and the counterweight structure underneath. To raise the door instantly, we let the counterweight fall by turning off the electromagnet with a switch placed next to the channel. The details about the rising door system are explained in Part I.

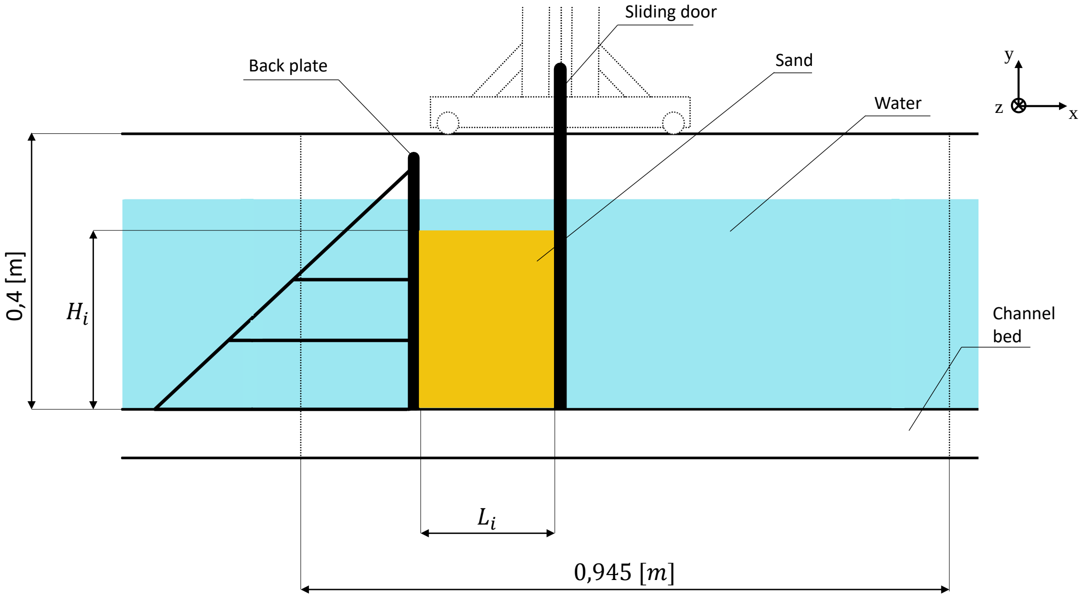

Figure 8.2: Zoom on the channel module with the sand column

Figure 8.2 shows a zoom on the inside of the channel. The sand column lies between the sliding door and a back plate (Figure 8.3) that remains vertical due to a metal structure set on the channel bed. The initial column is defined by its initial length, L_i and its initial height, H_i. The granular collapse is considered and analyzed in 2D.

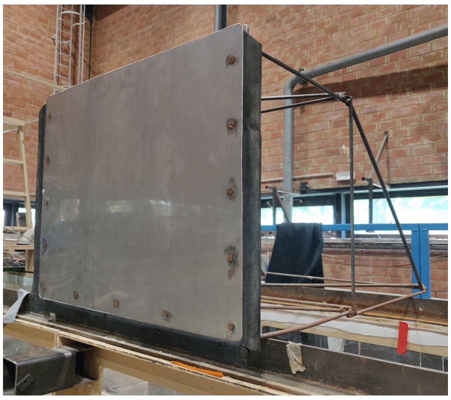

Figure 8.3: The back plate.

Figure 8.4: Camera setup

To record the experiments we used a LaVision HighSpeedStar fast camera placed at 1.10 meter from the channel wall, at 1.60 meter high over the ground and equipped with either a 50mm or 25mm lens. This camera is linked to a computer with the software PFV4 running to set parameters and to gather data (Figure 8.4). To ensure correct measurement we used a 27 cm ruler, placed under the channel wall, to calibrate the distances on the image processing software.

8.1.2 Procedure

The experimental procedure will be summarized here, for the detailed procedure see Appendix G.

Firstly, the channel is filled with water. Then we lower down the door and put the back plate in the desired place. The latter is adjusted to reach the desired L_i. The sand is next poured in between until we reach the desired H_i. When the camera is setup, he experiment is now ready to go. To launch the experiment, we simultaneously start the recording and open the door allowing us to observe the collapse and save the video recording at the end.

8.1.3 Repeatability

When conducting experimental studies, ensuring the reliability of results is crucial to verify that they are not the results of any random processes. To ensure this, it necessitates performing multiple experiments under identical conditions. However, in our case, achieving precisely the same initial conditions each time is quite challenging due to the numerous parameters that influence the collapse of the column. For example, even slight, imperceptible variations in compaction between experiments cannot currently be perfectly measured. Three experiments were conducted under initial conditions that were as similar as possible, including the same aspect ratio $a = 2$, the same compaction level with a loose column and the same type of sand (0-2mm).

For these three experiments, the final shape of the deposits is analyzed followed by an analysis the shape of the deposits three seconds after the door has been lifted up. The deposits are considered final when there are no more moving grains, excluding fine particles or dust in suspension in the water.

Figure 8.5 displays the final deposits obtained from these three identical experiments. The mean standard deviation of the deposits positions was $0.0348L_i$ [cm]. Additionally, the times taken to reach these final deposits were 16.51, 16.10, and 16.4 seconds, respectively. Meaning an average time of 16.34 seconds with a standard deviation of 0.173 seconds, corresponding to a variation of approximately $\pm 1.06\%$ of the mean collapse time of the three experiments. Considering the close similarity between the final deposits and the collapse times, it would be interesting to compare if the collapsing features are also similar.

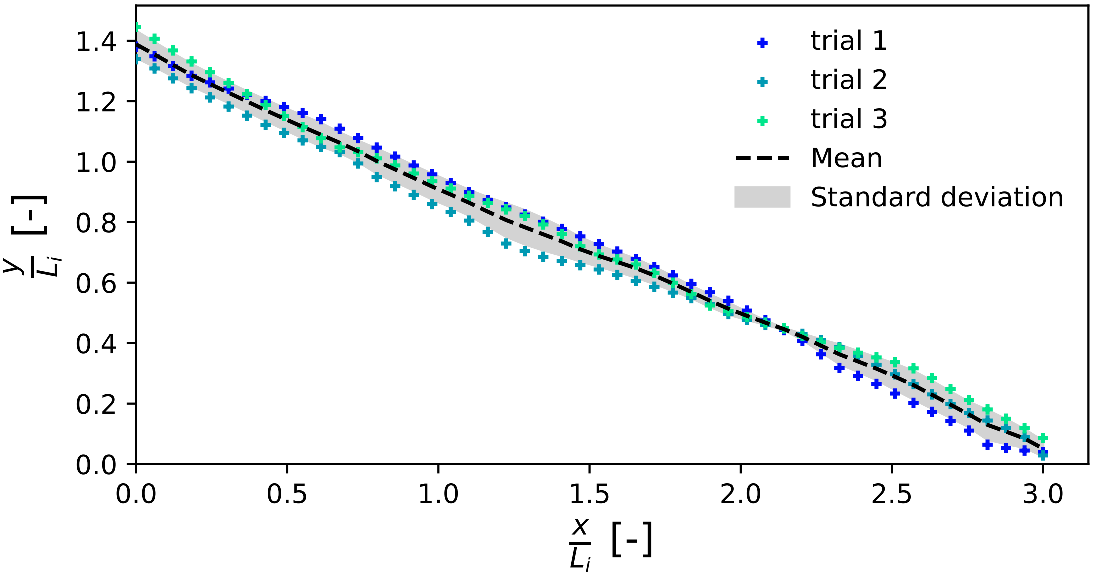

Figure 8.5: Final deposits of the three experiments to illustrate the repeatability of the latter. Initial condition of $a = 2$, loose column, 0-2mm sand. Plot of the trials are available in Appendix F, Figure F.1

Hence, Figure 8.6 provides reassurance regarding the repeatability of the experiments. This figure shows close similarity in the collapsing features of the three experiments with a mean standard deviation of the collapse shape after 3 seconds of $0.0462L_i$ [cm].

As it explained in the next section, during the image processing phase, a significant number of points is selected and then, an interpolation is made with those points to provide a more accurate representation of the interface between the sand and the water. Therefore, it is relevant to consider the influence of the interface discretization on the mean standard deviation. In previous calculations, the standard deviation was evaluated based on 50 discretized points. A study investigating the convergence of the mean standard deviation with respect to the number of discretization points was carried out and the results are available in Figures F.3 and F.4. This analysis confirms that we achieved a standard deviation close to its convergence value using only 50 discretized points.

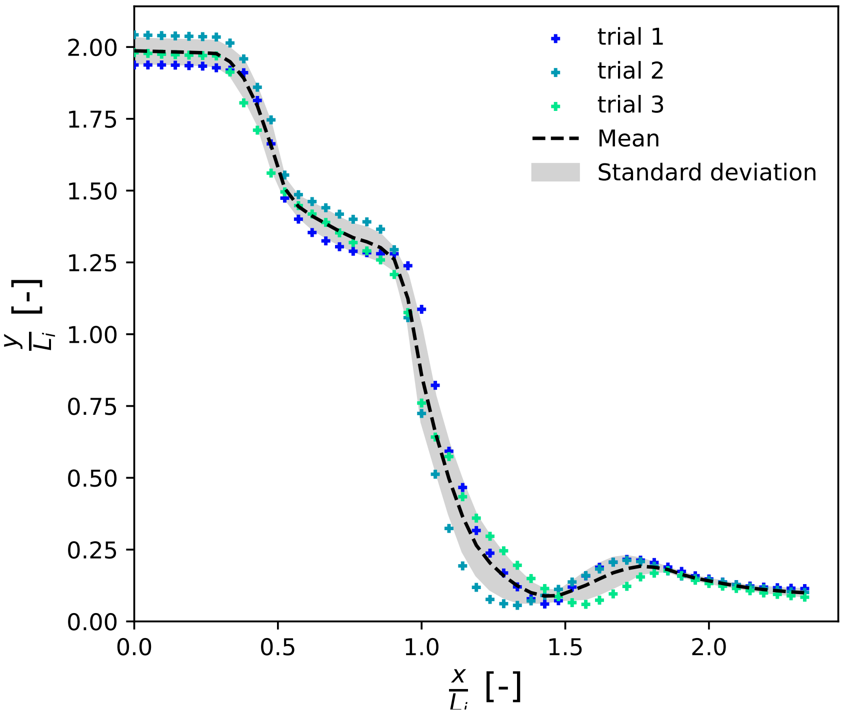

Figure 8.6: Deposits after 3 seconds of the three experiments to illustrate the repeatability of the latter. Initial condition of $a = 2$, loose column, 0-2mm sand. Plot of the trials are available in Appendix F, Figure F.2

In conclusion, we demonstrate repeatability of our experiments, indicating that the obtained results are not subject to any random processes.

8.2 Image Processing Techniques

8.2.1 Calibration

Before doing any analysis on our photographic records through any processing techniques, we must be aware of the deformation a picture can undergo when it is taken.
The first main deformation a picture can suffer is the distortion. The distortion is a deformation that depends on the lens used or directly from the water. Although Flora [6] shows that the distortion in her experiments can be neglected. Since we do not use the same camera and the same channel we can not directly take this conclusion for our pictures. Consequently it is recommended to carry out a calibration to analyze the recordings of our experiments.

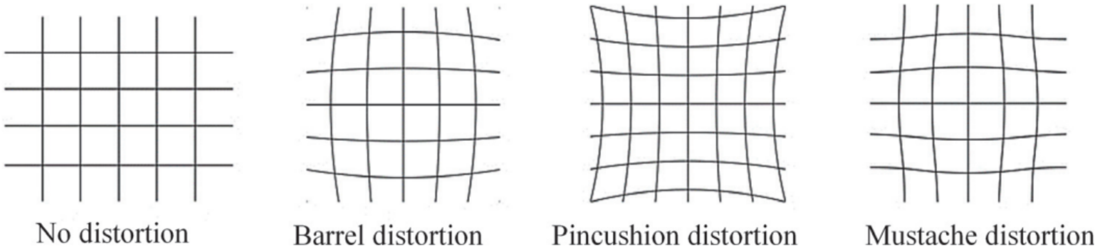

Figure 8.7: Types of distortion due to the lens of the camera [77]

The distortion is a parameter that is inherent for a lens. We can quickly determine the distortion due to this lens by applying PYTHON methods provided by `opencv`.

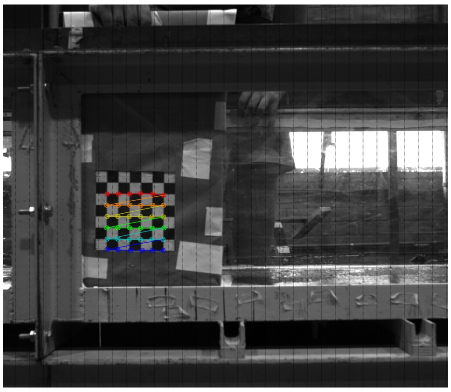

Figure 8.8: Example of the detection of the chessboard

The method to calibrate our camera involves placing a chessboard in front of it and then to start a recording. We have to move the chessboard all along the recording. The pictures are then collected and analyzed in PYTHON. We apply the function to detect the chessboard `findChessboardCorners` on small selection of pictures (about 10% of the total ones). Indeed, analyzing each of the 1361 pictures of the records will be too time consuming. An example of the application of the latter function is shown in Figure 8.8.

The intrinsic calibration matrix of the lens and the distortion coefficient is finally obtained via the function `calibrateCamera()` and are available in Appendix F.1. We can now correct the distortion caused by the camera lens. Figure 8.9 shows the difference before and after correcting the distortion (8.9a, 8.9b), as well as the difference between the two pictures 8.9c.

In Figure 8.9, we observe that the main differences between the initial image and the corrected one primarily appear around the cable. Moreover, the mean absolute difference between all the pixels of the two images is computed and we obtain 2.69%. This result was obtained through a calibration process using 100 images selected from a total of 1360 available . To explore the impact of different image samples on the calibration results, it would be interesting to examine the differences obtained by selecting alternative random sets of images. To investigate this, we conducted the calibration method on 20 randomly selected samples from the initial database of 1360 images. The mean value of the mean absolute differences between the calibrated and corrected images was found to be $3.94 \pm 1.17\%$, indicating some variability in the calibration outcomes across different image samples. The data are available in Figure F.5.

Finally, considering that we are processing the images along the interface between water and sand at the front window of the channel, it is reasonable to assume that there is no distortion caused by the water at this specific location. The distortion caused by the camera lens, which has been addressed through calibration method above, is the primary factor affecting the captured images.

8.2.2 Python

Once the calibration process is completed, one can analyze the data collected from the recorded experiments. The `matplotlib image processing` package for PYTHON proves to be highly efficient for this task. Considering that the camera captures approximately 1300 images for each experiment, our first step is to identify the most relevant images for the desired analysis. For example, we can focus on the images taken immediately after lifting the door, as they provide the initial conditions, along with images captured when the column reaches a state of rest. Additionally, we can select some images captured during the collapse of the column.

Our image processing method involves uploading the selected images to the PYTHON kernel using the `imread()` function and displaying them using the `imshow()` function.

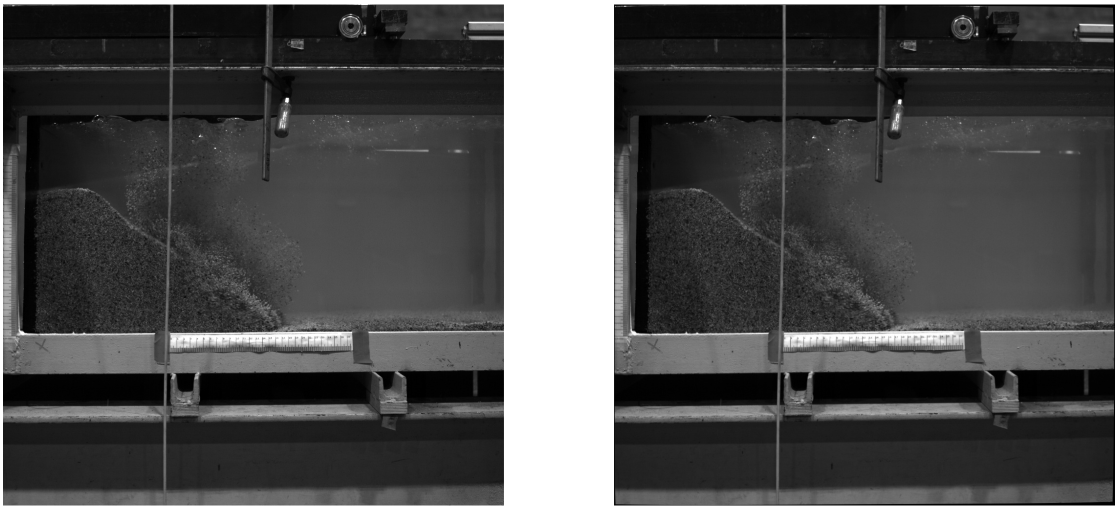

(a) Initial image, with distortion

(b) Corrected image, without distortion

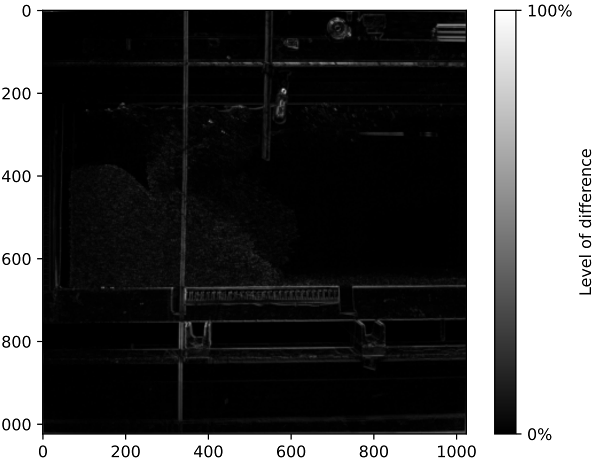

(c) Absolute difference between images (a) and (b). Pixels with a greater difference between the two images will appear lighter, while pixels with little or no difference will appear darker.

Figure 8.9: Application the calibration method on a figure and comparing the final results with the initial image.

Subsequently, we use the `ginput()` function to manually place points on the selected image. It is not necessary to select a large number of points. Indeed, as the goal is to capture the general shape of the interface, an interpolation technique is then applied to obtain a better discretization of the interface.

At this step, the obtained points are in a pixel scale. Therefore, it is necessary to convert the pixel measurements to centimeters thanks to the measurement band placed horizontally and vertically on the channel walls.

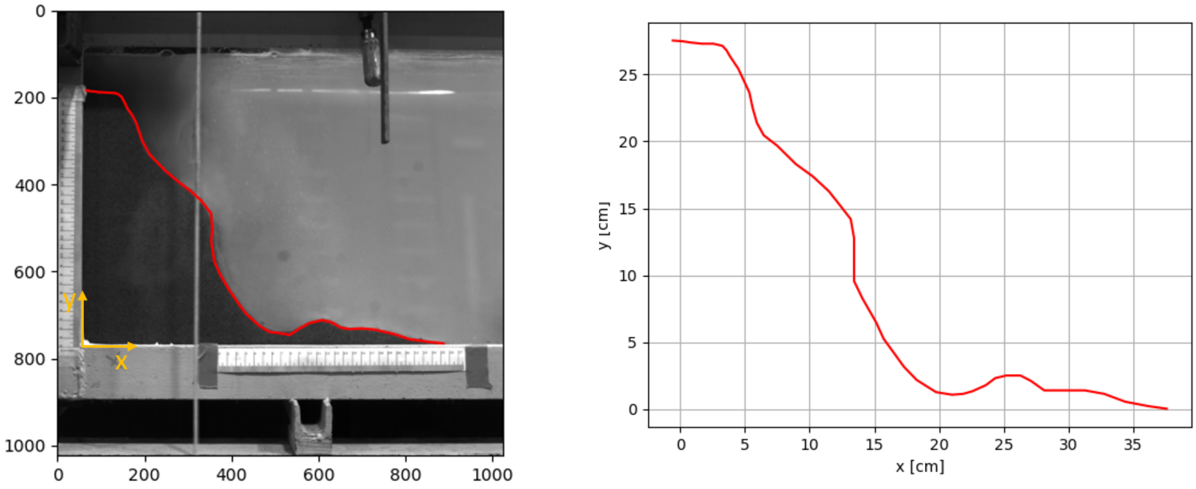

(a) Resulting image

(b) Resulting plot with the conversion pixel into centimeters

Figure 8.10: Example of image obtained with the PYTHON procedure and its resulting plot

8.2.3 Davis 8

DAVIS 8 (LaVision) is a software solution for intelligent (laser) imaging for fluid dynamics, combustion, spray applications as well as material strain and deformation. It employs a non-intrusive Particle Image Velocimetry (PIV) method to compute velocity fields from our laboratory experiment images. Usually, PIV requires the use of tracer particles and laser illumination of the studied section. However, in our experiments, the presence of fine particles in the sand, which become suspended during and after collapse, prevents us from using a laser to illuminate the entire area. Therefore, preprocessing becomes crucial.

To address this challenge, a preprocessing is performed on the images with an intensity particle normalization. A geometric masks can be applied to focus only on the desired areas of the image, reducing computational demands.

According to LaVision [78], velocity calculation involves subdividing the particles image into small interrogation windows. The average particle displacement within

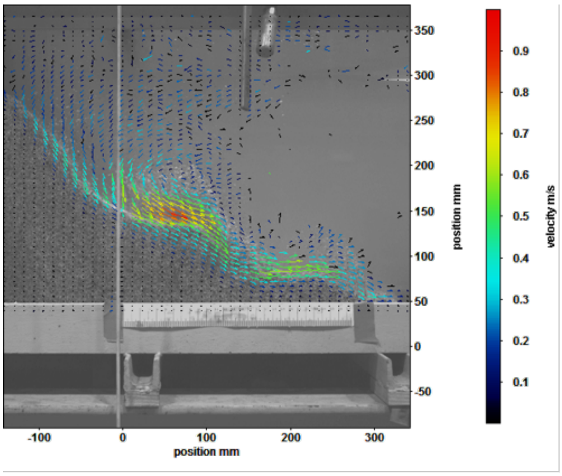

Figure 8.11: Example of vortices seen through Davis 8

an interrogation window is determined using cross-correlation followed by the localization of the correlation peak. From the known time difference dt and the measured displacement dx in each direction (longitudinal and vertical) the velocity components are calculated with $dv = \frac{dx}{dt}$.

Following the vector computation, a multi-pass post-processing step is conducted to remove outliers and vectors with insufficient correlation between different time steps. Some particles exhibit behavior that deviates significantly from others, indicating a low correlation between two interrogation windows, which is an indicator of their low probability of existence.

To complete Davis' description, it would be interesting to have an idea of the error that the software makes when computing the velocity vectors. Boomsma *et al* (2016)[79] presented a comparative experimental evaluation of uncertainty estimation methods for two-component PIV. It showed that Davis has a 98.6% Cross Correlation coefficient and a RMS (Root Mean Square) Relative Error of about 0.8%. However, it should be noted that the error committed depends strongly on the choice of many software parameters and on the choices of post-treatments.

8.3 Initial volume fraction

In this section we will try to determine the initial volume fraction of our sand column. Since in our case it is impossible to determine it directly in the channel, we are going to carry out laboratory experiments under conditions similar to those in the channel.

In our case, the sand is simply poured into the water and we wait for the suspended particles to stabilize a bit, but we don't completely stir and wait for all sand to stabilize down. By using the method described in Lee *et al.*[44], and using the same filling method as in the channel, we can have an idea of the volume fraction. This is the method :

1. A graduated cylinder is partially filled with water
2. The sand with known mass m is poured into the cylinder, the volume of the grains is known by $V_{grains} = \frac{m}{\rho_{sand}}$, where $\rho_{sand} = 2640[kg/m^3]$[1]
3. The mixture settle down after a few moments. This configuration is considered loose.
4. The bulk volume of the sand column V_{bulk} is determined by measuring the location of the interface between the water and the column of sand grains.
5. The initial volume fraction is $\phi = \frac{V_{grains}}{V_{bulk}}$.

To simulate the dense column we tap on the cylinder until the sand is compacted at step 3.

The results we computed are available in Table 8.1.

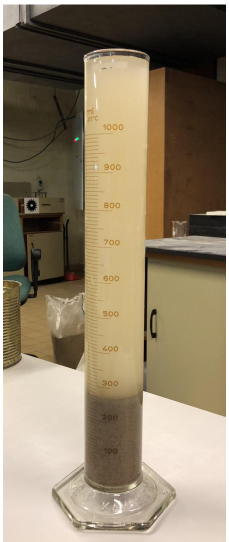

Figure 8.12: Computing initial volume faction

	Initial volume fraction (ϕ)	
	Loose column	Dense column
Thin sand ($d_{50} = 0.366$ mm)	0.569 ± 0.005	0.630 ±0.007
Coarse sand ($d_{50} = 1.73$ mm)	0.550	0.581

Table 8.1: Initial volume fractions

The volume fractions we have found correspond to those that can be found in the literature (see Section 7.2). This method tends to have the same conditions as in the channel but notice that it slightly differs from the channel setup. In fact, in the channel the sand is shoveled by heap, most of the time the sand is already wet before pouring it into the channel, the container does not have the same shape and size, the amount of sand is different, multiple parameters that can affect the volume fraction are different from the graduated cylinder to the channel. Therefore, we can not set an exact value for the volume fraction but it is a good approximation, in accordance with the literature and numerical study in Chapter 10. The sand column in the experiments is still considered to be loose and the value of the initial

---

[1] The density can be found in the sand provider DoP [80]

volume fraction should be around the one found in Table 8.1. It will probably be slightly higher because the value found is for practically the loosest case possible with our sand.

8.4 Varieties of sand used

This section aims to examine and characterize the sand used in the experiment. Indeed, as mentioned in Section 7.3, the shape and the size of the grains of the sand are significant factors that directly impact our experiments.
Therefore, it's crucial to have well characterized the type of sand we are working with in order to accurately compare the experimental results with the numerical ones.
A sand can be firstly characterized with a rough scale of the grain distribution corresponding to a range of the smallest and largest size of grains. We can be even more precise by determining the particle size distribution curve which provides information on its mean and median distribution[2], also called d_{50}.
Another criteria to characterize the sand is if its grains have a more uniform or wide distribution, characterize by the σ_G criteria **Sandra-course**.

$$\sigma_G = \sqrt{\frac{d_{84}}{d_{16}}} \tag{8.1}$$

$$\sigma_G < 1.3 : \text{ uniform distribution} \tag{8.2}$$

$$\sigma_G > 1.6 : \text{ wide distribution} \tag{8.3}$$

To achieve this goal, various sieve tests were carried out on the different sand types.

8.4.1 0-2mm

The first sand used has grains whose size is between 0 and $2mm$. Several sieve tests were performed on this sand and the resulting grains size distribution curve was obtained:

---

[2] Meaning that, 50% of the sand grains have a bigger size and 50% a smaller one

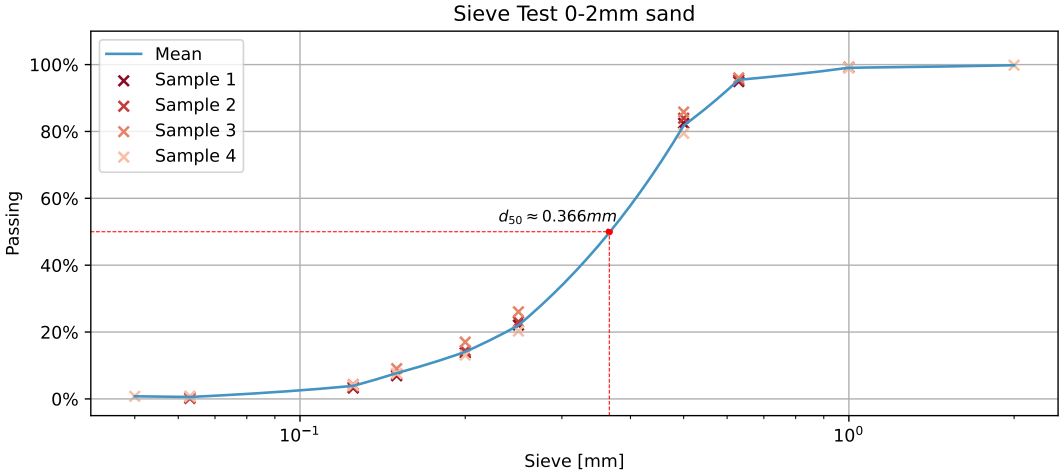

Figure 8.13: Grains size distribution curve of the 0-2mm sand, obtained by sieve tests

We can graphically observe that this first sand has a median grain size distribution of $d_{50} = 0.366$ and compute its median $\overline{d} = 0.275mm$. Moreover, we computed its σ_G criteria and obtain a value of $\sigma_G = 1.57$, meaning that this sand tends to have an wide distribution of its grains.

As we can observe in its distribution curve, the sand contains some fine particles ($< 100\mu m$). When using this sand for our experiments, it is mixed with water that is drained after each experiment and the sand is subsequently reused. As a result, it is important to acknowledge the potential impact of these multiple uses with water on the grain distribution of the sand, which could be filtered out of its finer particles.

Figure 8.14 shows the comparison between the unused sand and the same sand that has been used and mixed several times with water. We clearly observe that, as predicted hereover, the used sand has had its finer particles filtered out. This filtering leads to a shift in its median distribution, now equal to $d_{50} = 0.41$. Since we removed the finer particles of the sand, we can expect that this distribution will be more uniform than the unused sand. Indeed, its σ_G criteria is now equal to $\sigma_G = 1.44$ and is considerably lower, so the sand is more uniform, as expected.

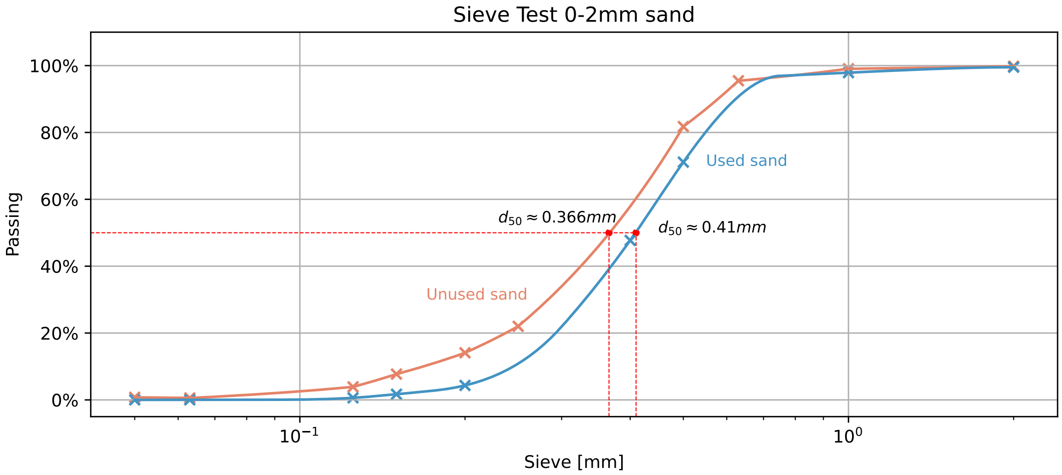

Figure 8.14: Grains size distribution curve of the 0-2mm sand used several times in water, obtained by sieve tests

8.4.2 0-3mm

In order to facilitate a more accurate comparison between our experimental results and those obtained through the former channel, we have opted to use a second type of sand that is *a priori* similar to the one used in the old experiments. This will also provide us opportunities to observe and compare the differences in the collapse of a granular column using two distinct types of sand.

The second sand that we have used has grains whose size is between 0 and 3 mm. Several sieve tests were also performed on this sand and the resulting grains size distribution curve was obtained:

By analyzing its distribution curve, we can graphically observe that the second type of sand has a median grain size of $d_{50} = 1.73$ mm and mean diameter $\overline{d} = 1.363$ mm. We computed its σ_G criteria and obtain a value of $\sigma_G = 1.28$, meaning that this sand tends to have a more uniform distribution of its grains.

Although the upper and lower grain size limits are nearly similar, the distribution of the two sands is vastly different. Indeed, the second sand is composed of mostly larger grains.

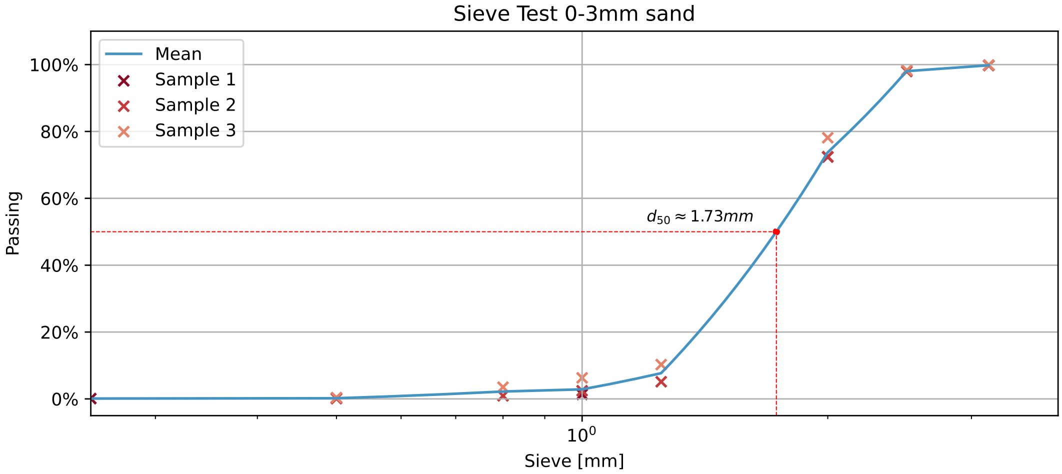

Figure 8.15: Grains size distribution curve of the 0-3mm sand, obtained by sieve tests

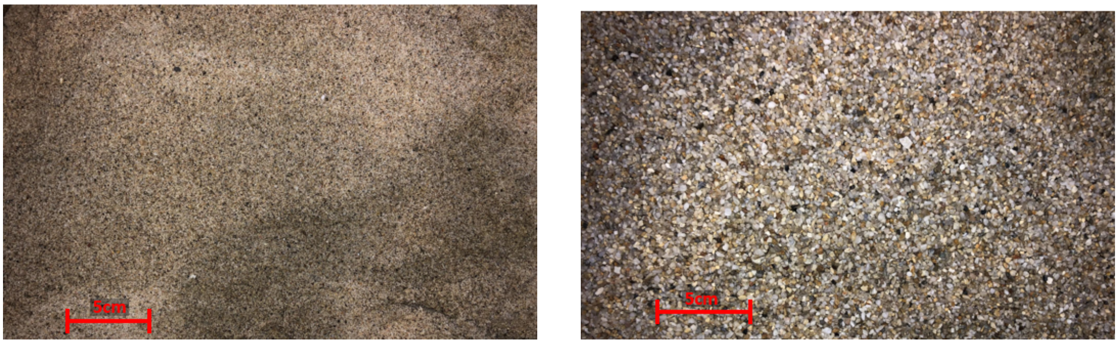

(a) 0-2mm sand

(b) 0-3mm sand

Figure 8.16: Pictures of the different types of sand used

8.5 Limitations of the setup

Unfortunately, no experimental setup is perfect. The limitations of our setup are detailed hereunder.

8.5.1 Deflection

The door that is supposed to be perfectly vertical is, in fact, curved to the right (see Figure 8.17. This is due to two reasons : the first one is that, when welding the upper part of the door (see Section 4.5), the heat has locally modified the microstructure of the door and that resulted in a slight curvature of the door. The second reason is due to the hydrostatic pressure coming from the mixture of water and sand. Although, it was supposed to support it, the initial curvature induced a greater deflection than expected.

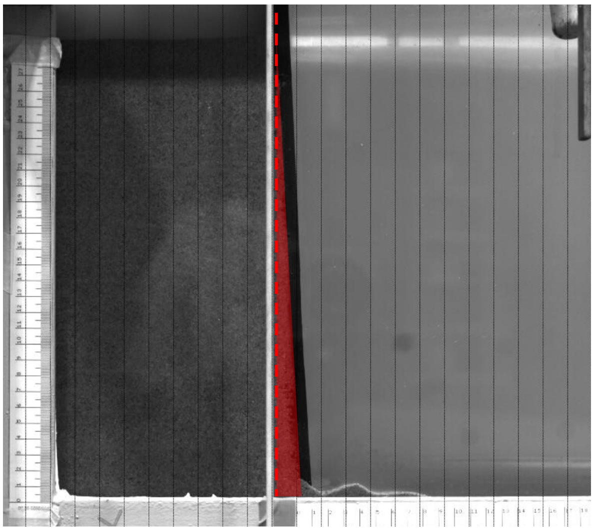

Figure 8.17: Door deflection

8.5.2 Rising door

As highlighted by Flora Nennen[6] and Benoit Spinewine[81] , a rising door can have a few drawbacks. We see on Figure 8.19 the amount of sand moved by the three different drawbacks of Figure 8.18. We can clearly observe that the most important one is the one moved by friction. This is due to the fact that, to ensure proper sealing, the gasket is wider than the plate thickness. When rising, the gasket catches thus some sand grains along the way. Moreover, due to the deflection of the plate, the run is not to perfectly vertical and the plate therefore pushes even

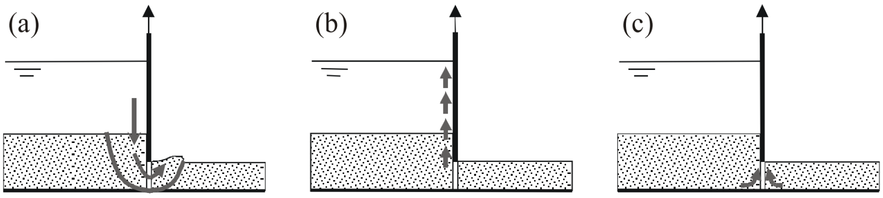

Figure 8.18: Drawbacks of a rising gate system, inducing spurious soil movements during gradual lifting as a result of (a) mass failure; (b) friction; (c) depression and suction [81].

more grains when rising. The sand displacements induced by mass failure and by depression and suction are way smaller. Therefore, we take the liberty of neglecting the latter in relation to the volume of the whole sand column.

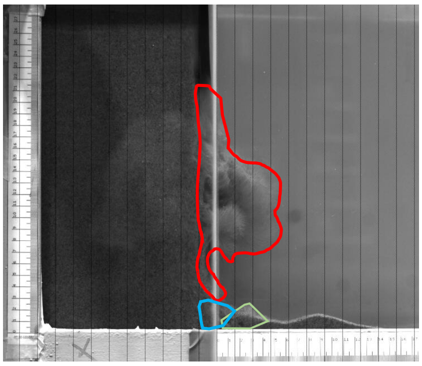

Figure 8.19: Experimental observations of drawbacks inducing soil movements during lifting as a result of (blue) mass failure; (red) friction; (green) depression and suction

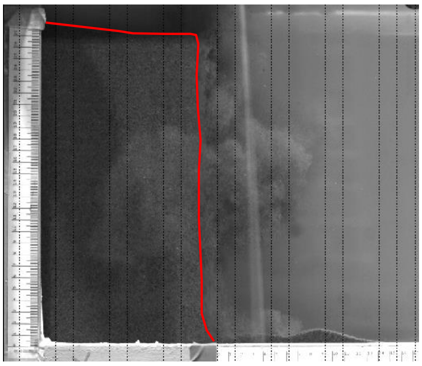

Figure 8.20: Considered column when experimenting

To solve this, we only take into account the grains that remain static after the door has been lifted. As seen in Figure 8.20, these static grains compose the studied sand column.

8.5.3 Sealing

At the door

The door is enclosed with a gasket (see Section 4.4) to ensure sealing when it is in its lower position. Residual sand grains can stay on the gasket after the door opening. To ensure proper sealing the gasket needs to be cleaned every time before re-lowering the door. But even with cleaned gasket, there are small leaks at the bottom corners due to the fact that the gasket is bent at 90 degrees to fit the shape of the door. Even if it is compliant, it cannot form a perfect angle to fill the shape of the intersection of the channel bottom and its walls. It leaves thus a slight opening in the angle. The consequence is that when pouring the sand, a small part slip on the other side of the door as seen in Figure 8.21. The sand rapidly seals the small opening and the leaked part is small enough to be neglected compared to the total volume of the sand column ($\frac{V_{leaked}}{V_{column}} \simeq 0.7\%$).

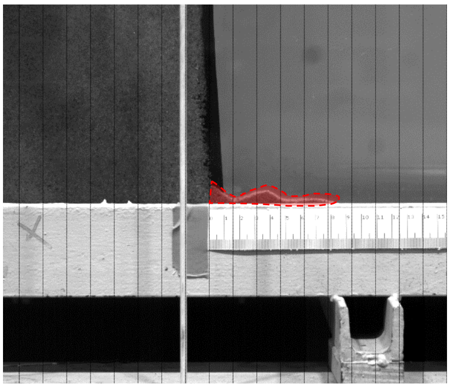

Figure 8.21: Leaked sand through the door

In the channel

The downstream plate has a very poor sealing. This problem was very constraining because the channel was emptying while we were trying to perform experiments. To solve this, we had to make a homemade sealing system using rubber strip and waterproof tape.

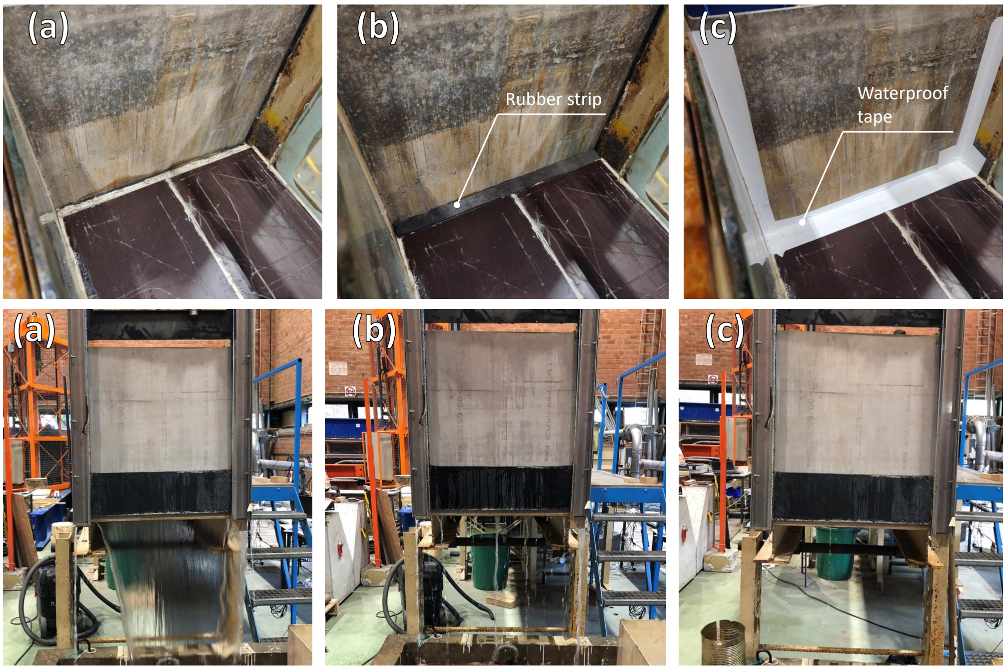

Figure 8.22: Water leak at the downstream plate of (a) 2.376 L/s (no sealing), (b) 0.41 L/s (rubber strip), (c) 0.033 L/s (rubber + tape)

We managed to reduce the leak from 2.376 L/s to 0.41 L/s using rubber strip only and to 0.033 L/s using rubber strip and waterproof tape. Respectively (a), (b) and (c) in Figure 8.22.

8.5.4 Cables

The rising door system works with a counterweight. As explained in Section 4.1, the door is linked to the counterweight with cables. Due to the configuration of the system, the cables are placed between the channel and the camera. These cables can be annoying when analyzing the video recordings because they appear in front of the sand column (Figure 8.24). Moreover, after the counterweight has fallen, the cables oscillate a lot (Figure 8.23b). This is an issue when doing the PIV analysis because the software analyze every particles movement and the cable is creating unwanted movement on the video as it can be seen on Figure 8.24.

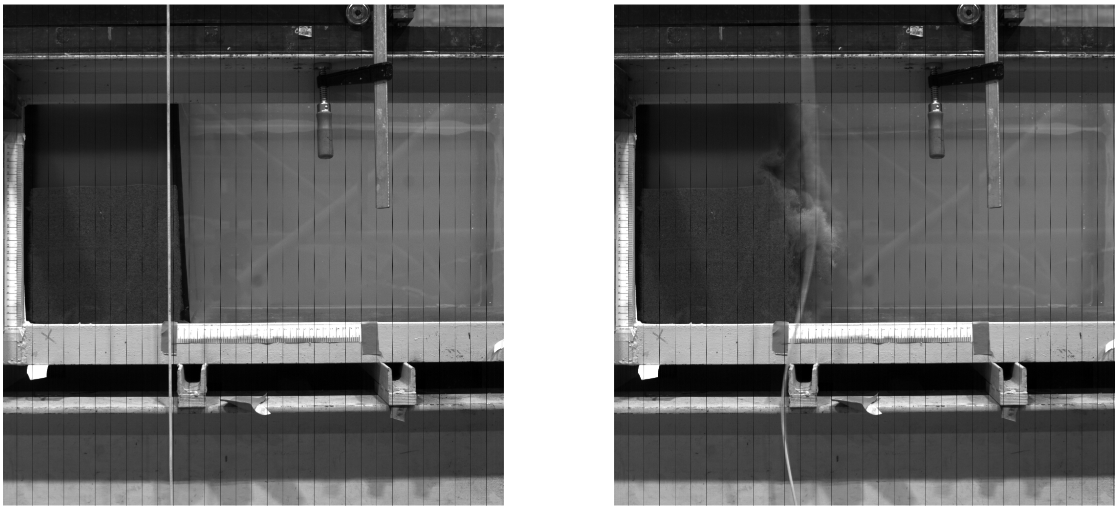

(a) Cable in the video recording

(b) Cable oscillation

Figure 8.23: Issues induced by the cables

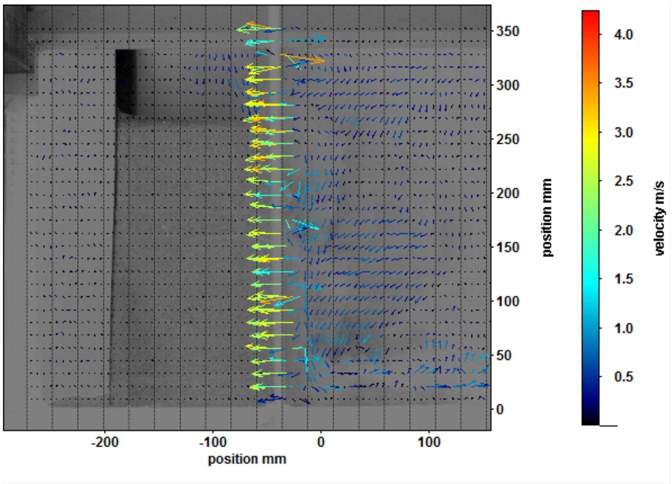

Figure 8.24: Cable oscillation detected by the PIV analysis on DaVis 8

8.5.5 Limited window

The channel is 40 cm high and 94.5cm long but the visible window is restricted to only 33 cm high and 82.5 long, because of the frame of the channel modules as seen in Figure 8.25. When collapsing, the sand column reaches a final length L_f. If this L_f is too large, it can exceed the length of the window and thus the end of the final deposit would be hidden behind the frame.
As is can be seen in Figure 8.26a, the bed of the channel is a few millimeters lower than the bottom frame. We observed that when the column collapse, there is a thin layer of sand that spreads in the continuity of the runout distance (see Figure 8.26b). This thin layer is impossible to record because of the frame slightly sticking out.

Figure 8.25: Channel module

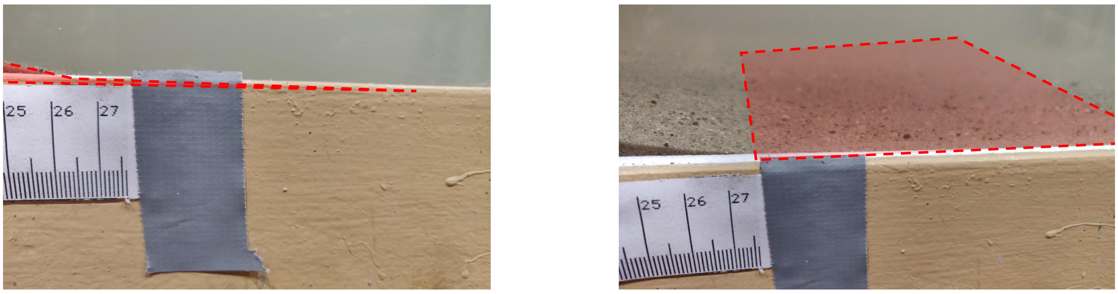

(a) View in front of the end of the column runout

(b) View from above of the end of the column runout

Figure 8.26: Thin layer of sand hidden by the frame

9

Experimental results

This chapter covers a parametric study of the collapse of the granular column. The objective is to investigate the influence of different parameters on the collapse process and to present the results obtained through the several image processing methods described in the previous chapter. Furthermore, it compares our experimental recordings with the ones of the former setup.

9.1 Parametric study

9.1.1 With respect to the aspect ratio

Firstly, the collapse behaviors and collapse features of each aspect ratio are described, based on the raw[1] recordings. Subsequently, the PYTHON procedure is employed to analyze the data. The resulting graphs are used to compare the various aspect ratios in terms of collapse duration, dimensions, repose angle, and final deposits shapes. This comparative analysis provides insights into the differences and similarities between the different aspect ratios.

Aspect Ratio $\mathbf{a} = \frac{1}{2}$

When we have an aspect ratio of $\frac{1}{2}$, a notable phenomenon occurs as the door is opened in the top right-hand corner of the column. This particular region experiences a relatively quick collapse compared to the overall duration of the column's fall, as we can observe at $t^+ = \frac{1}{5}$. We can also see that many fine particles are suspended in water all along the collapse.

---

[1] What we mean by raw is the images obtained from the camera

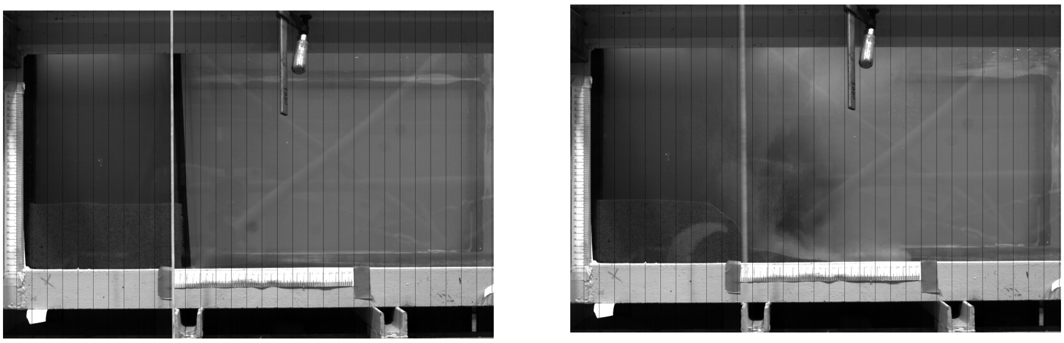

(a) Initial configuration, $t^+ = 0$ (b) $t^+ = \frac{t}{t_f} = \frac{1}{5}$

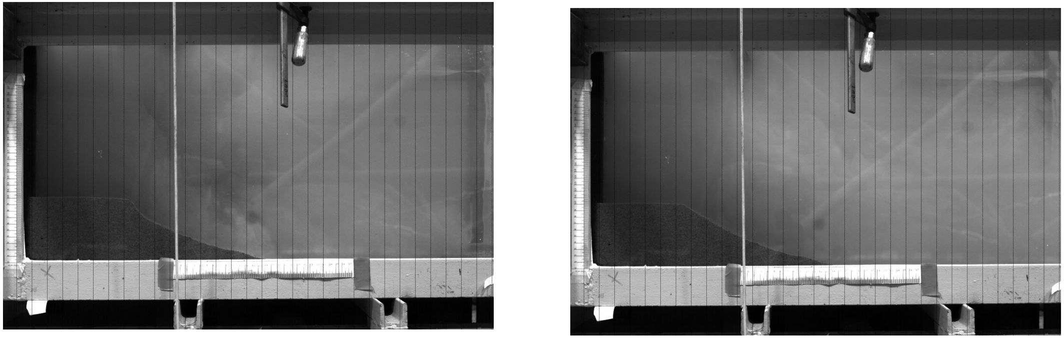

(c) $t^+ = \frac{t}{t_f} = \frac{1}{2}$ (d) Final deposits, $t^+ = 1$

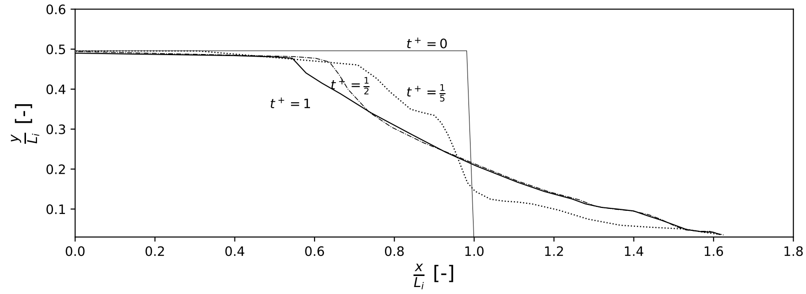

(e) Collapse features through the PYTHON procedure

Figure 9.1: Time evolution of the collapse for aspect ratio $a = \frac{1}{2}$

The suspended fine particles exhibit intriguing movements, potentially forming vortex-like shapes but it is quite difficult to see them, hence the importance the velocity analysis through DAVIS 8 software. One can also see that halfway through the collapse, we are already close to the shape of the column's final deposits. Finally, the final deposit of the column has a trapezoidal shape and the column quickly reaches its final length, already at $t^+ = \frac{1}{5}$.

Aspect Ratio a = 1

When the aspect ratio is increased to 1, a rather interesting phenomenon appears. If we observe the Figure 9.1b, when the upper right-hand corner of the column falls away along the column, the rapid falls of the sand create an hollow area, followed by a small bump. This bump and hollow are swiftly filled in once all the sand particles of the upper right-hand corner have fallen away.

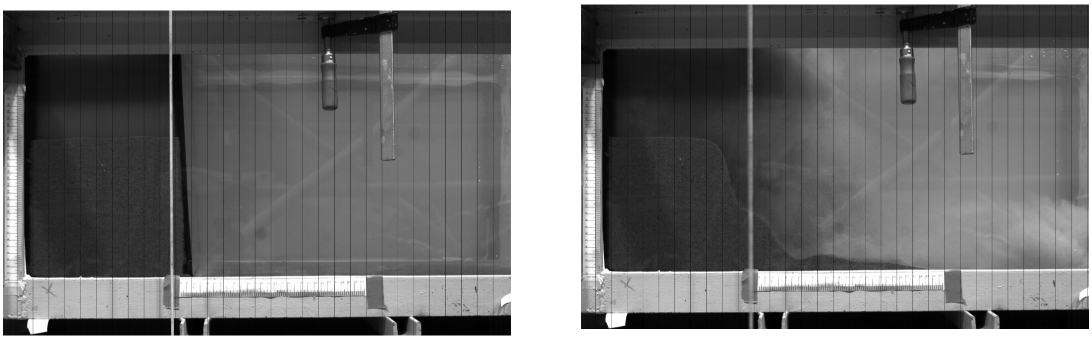

(a) Initial configuration, $t^+ = 0$ (b) $t^+ = \frac{t}{t_f} = \frac{1}{5}$

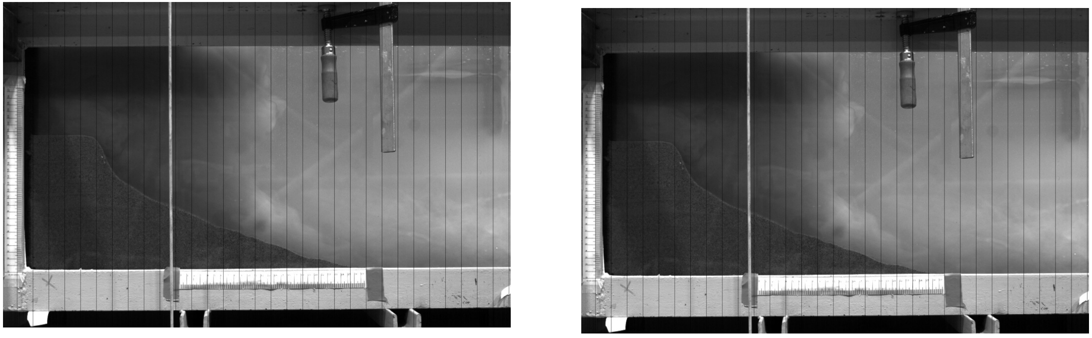

(c) $t^+ = \frac{t}{t_f} = \frac{1}{2}$ (d) Final deposits, $t^+ = 1$

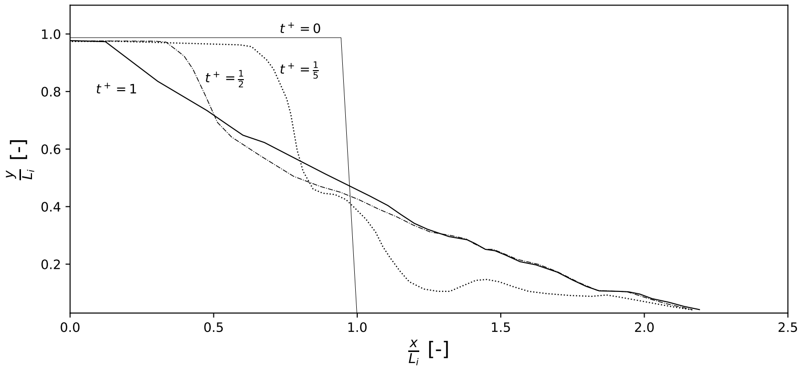

(e) Graph obtained through the PYTHON procedure, showing collapse features

Figure 9.2: Time evolution of the collapse of the column of aspect ratio $a = 1$

Similar to the aspect ratio of $\frac{1}{2}$, we also notice that halfway through the collapse, we are already close to the shape of the column's final deposits. Moreover, the final deposits of the column has also trapezoidal shape and the column quickly reaches its final length, even at $t^+ = \frac{1}{5}$ too.

Aspect Ratio $\mathbf{a} = \frac{3}{2}$

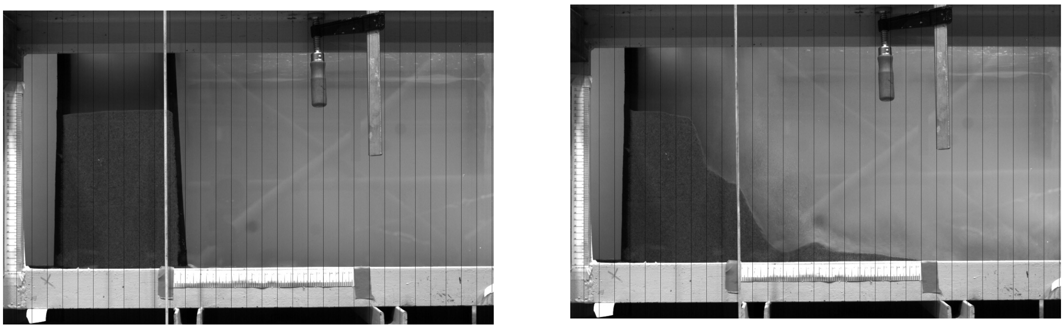

(a) Initial configuration, $t^+ = 0$

(b) $t^+ = \frac{t}{t_f} = \frac{1}{5}$

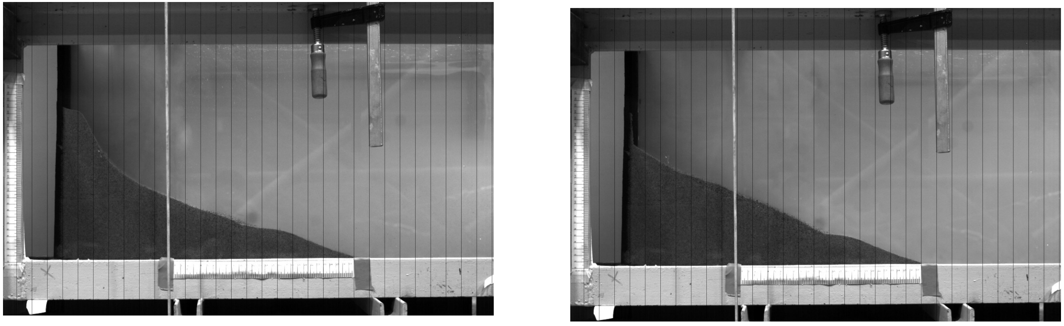

(c) $t^+ = \frac{t}{t_f} = \frac{1}{2}$

(d) Final deposits, $t^+ = 1$

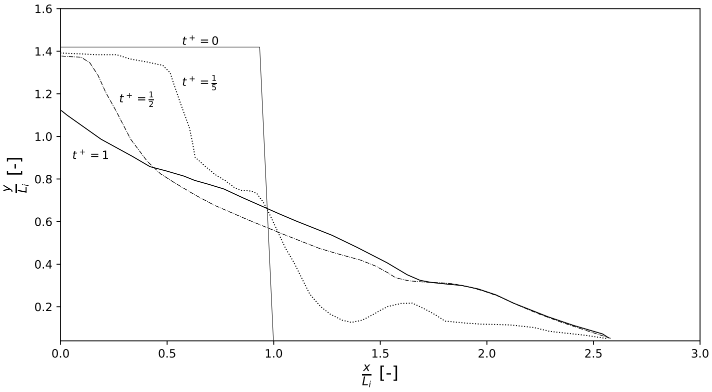

(e) Graph obtained through the PYTHON procedure, showing collapse features

Figure 9.3: Time evolution of the collapse of the column of aspect ratio $a = \frac{3}{2}$

With an aspect ratio now of $\frac{3}{2}$, we see nearly the same collapse behavior as with the unit aspect ratio. We still observe the creation of a hollow zone and a small bump during the collapse. However, the notable difference lies in the final shape of the deposits. Instead of being trapezoidal, it now takes on a triangular form.

Aspect Ratio a = 2

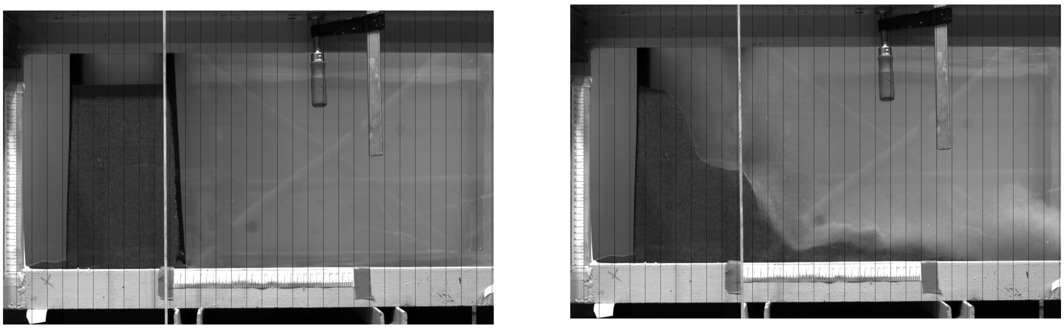

(a) Initial configuration, $t^+ = 0$

(b) $t^+ = \frac{t}{t_f} = \frac{1}{5}$

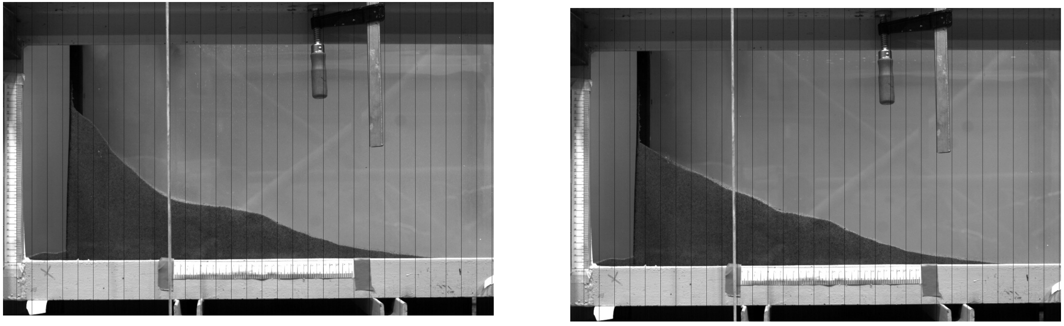

(c) $t^+ = \frac{t}{t_f} = \frac{1}{2}$

(d) Final deposits, $t^+ = 1$

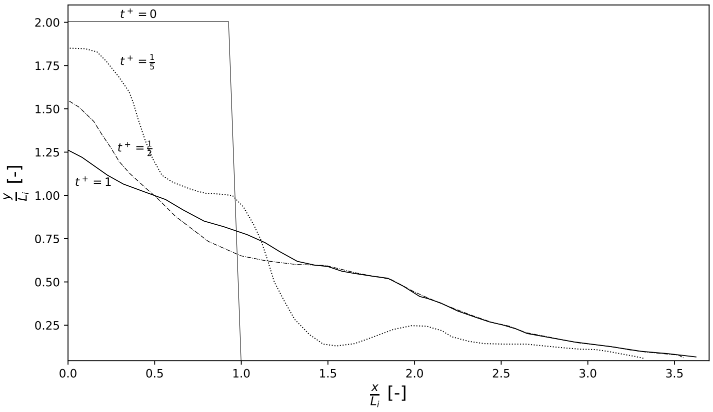

(e) Graph obtained through the PYTHON procedure, showing collapse features

Figure 9.4: Time evolution of the collapse of the column of aspect ratio $a = 2$

When we increase the aspect ratio up to 2, we observe similar collapse characteristics as $a = 1$ a,d $a = 1.5$. The upper right-hand part of the column slides, resulting in the formation of a hollow zone downstream, followed by a slight bump. Similarly to the other aspect ratios, we reach nearly the final length halfway through the collapse. This suggests that the column undergoes the most significant changes during the first half of its total collapse time. Subsequently, it continues to collapse, but more gradually, ultimately forming a triangular-shaped deposit.

Aspect Ratio $\mathbf{a = 3.85}$

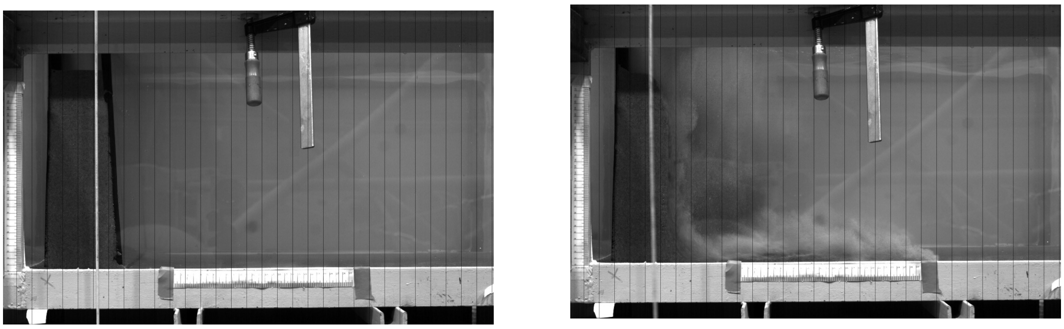

(a) Initial configuration, $t^+ = 0$

(b) $t^+ = \frac{t}{t_f} = \frac{1}{5}$

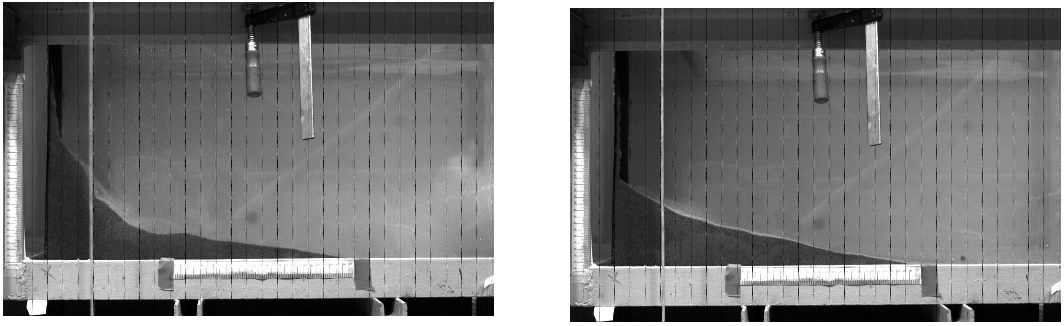

(c) $t^+ = \frac{t}{t_f} = \frac{1}{2}$

(d) Final deposits, $t^+ = 1$

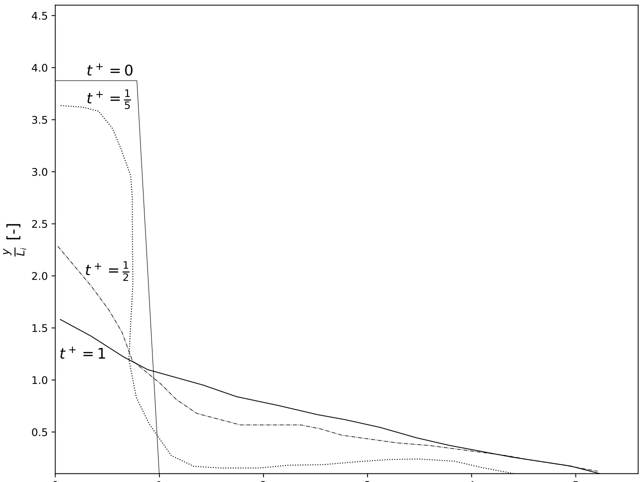

(e) Graph obtained through the PYTHON procedure, showing collapse features

Figure 9.5: Time evolution of the collapse of the column of aspect ratio $a = 3.85$

When we considerably increase the aspect ratio, we still continue to have the same behavior as the one for $a = 2$. However, the column falls faster as we can seen in the height difference between $t^+ = \frac{1}{5}$ and $t^+ = \frac{1}{2}$ compare to the other aspect ratios. The runout distance seems also to be higher.

Table 9.1 and Figure 9.6 present a comparison of the fifth aspect ratios studied, highlighting various criteria for comparisons such as collapse time, final height to initial height ratio, the runout distance L_∞ etc. It also presents a new criteria, the dimensionless time T. This dimensionless time was proposed by L. Lacaze *et al.* in [82] to better compare the different times of collapse t_∞ by taking into account the initial height of the column and is expressed as follow:

$$T = t_\infty \sqrt{\frac{g}{H_i}} \text{ [-]} \tag{9.1}$$

where g is the gravitational constant.

	$a = \frac{1}{2}$	$a = 1$	$a = \frac{3}{2}$	$a = 2$	$a = 3.85$
Shape of final deposit	Trapezoidal	Trapezoidal	Triangular	Triangular	Triangular
Angle of respose α [°]	30.08	28.52	23.89	21.53	18.92
Runout distance L_∞ [-]	0.63	1.19	1.58	2.62	4.24
Ratio $\frac{H_f}{H_i}$ [-]	0.98	0.99	0.79	0.63	0.42
Time of collapse t_∞ [s]	9.33	16.12	14.40	14.16	9.25
Dimensionless time T [-]	90.18	102.11	91.12	82.36	79.02

Table 9.1

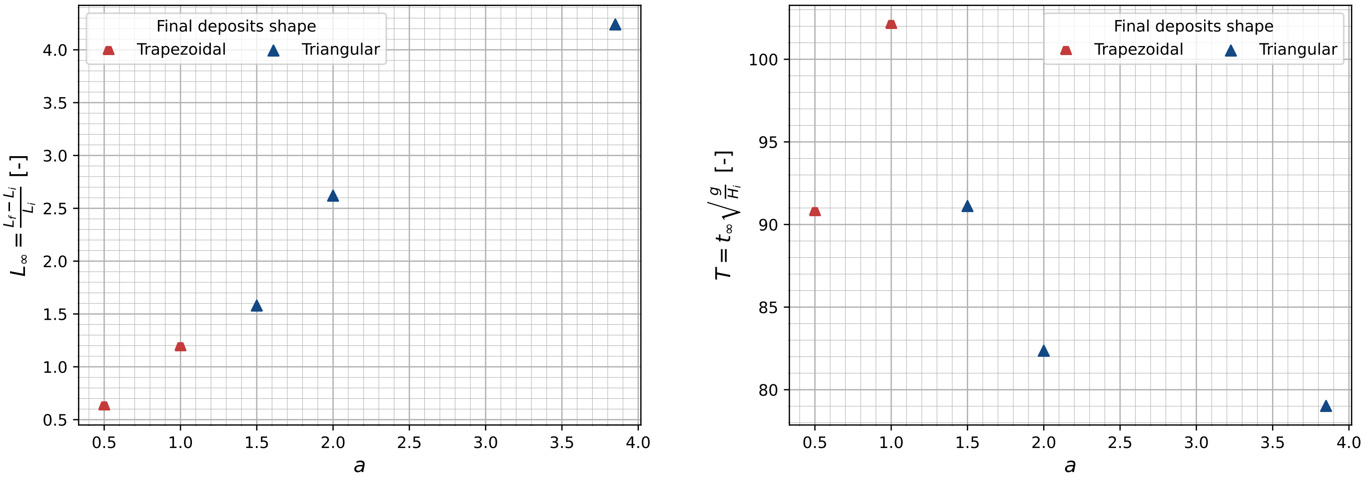

(a) Runout distances comparison, L_∞ (b) Dimensionless times comparison, T

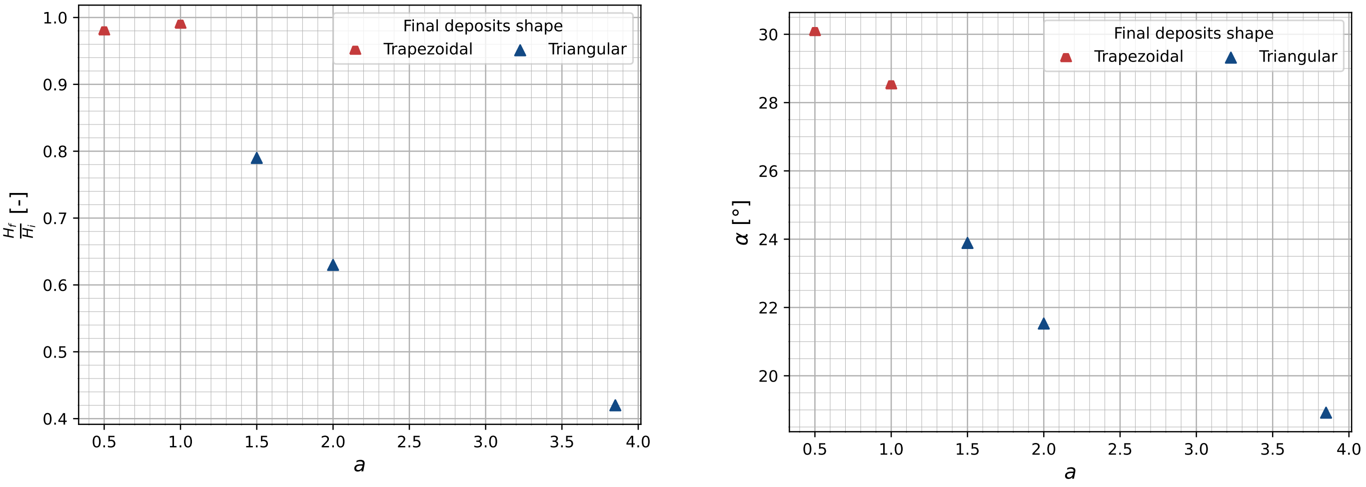

(c) Heights ratios comparison, $\frac{H_f}{H_i}$ (d) Repose angles comparison,α

Figure 9.6: Comparison of the fifth aspect ratios with various criteria

Failure surface

When tuning the aspect ratio, we also observed that the failure surface was significantly different. In Figure 9.7, we observe that, the higher the aspect ratio is, the deeper in the column is the failure surface. In Figure 7.1, we noted that for coarse sand and loose column, the critical aspect ratio was $a_L = 3$. We can note that with our configuration, the critical aspect ratio is not yet reached at $a = 3.85$.

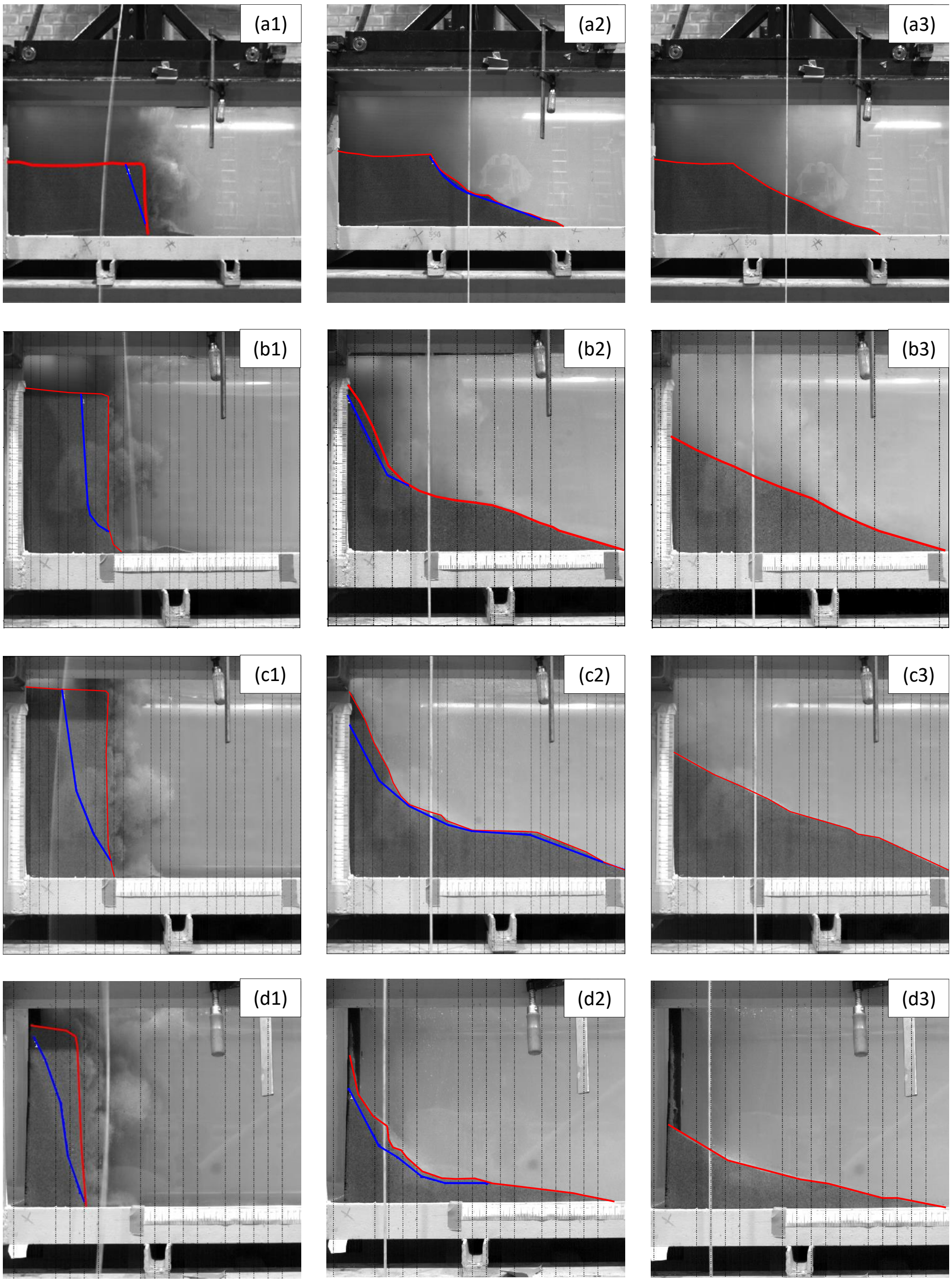

Figure 9.7: Collapse of submerged sand column with aspect ratio of (a) $a = 0.68$; (b) $a = 1.74$; (c) $a = 2$; (d) $a = 3.85$ and at time (1) $t = 0$; (2) $t = t_\infty/2$; (3) $t = t_\infty$. The red is the contour of the column. The blue line is the failure surface.

Summary

To summarize the parametric analysis of the collapse of granular column with respect to the aspect ratio, several observations can be noticed.

Firstly, when the aspect ratio exceeds a value of one, the final shape of the deposit tends to have a triangular shape. Below this value, the final shape of deposit takes on a trapezoidal shape.

Secondly, the angle of repose seems to decrease as the aspect ratio increases. Conversely, the run-out distance is increasing significantly as the aspect ratio increases.

Furthermore, the ratio between the initial and final height of the column appears to decrease as the aspect ratio increases. This ratio is close to one for aspect ratio below unit value and seems directly related to the final shape of the column.

Lastly, in terms of collapse times, we notice a faster fall for low aspect ratios such as $a = 0.5$ compare to $a = 1$. However, if we continue to increase the aspect ratio beyond one, the collapse time decreases.

9.1.2 With respect to the initial volume fraction

As determined in Section 8.3, the default sand column is simply poured in the channel. The column is thus considered to be loose with an initial volume fraction of $\phi_{loose} \simeq 0.569$. In this section we will study the differences when the sand column is dense.

To compact the sand column we used a piece of wood to push on the top of the column. It is impossible to determine the volume ratio directly in the channel but as for the loose column, we will estimate it by using the results found in Table 8.1 : $\phi_{dense} \simeq 0.630$

In Figure 9.8, we observe that the collapse features are different depending on the initial volume fraction. For the loose column, a big sand volume is detached in one from the rest of the column, in the right upper corner. In contrast, for the dense column we observe a slower erosion and sand volumes that come off the column are smaller and more numerous. The dense column is slightly slower to reach its final shape, and has a higher H_f
But we also observe that that behavior of both columns does not differ as much as

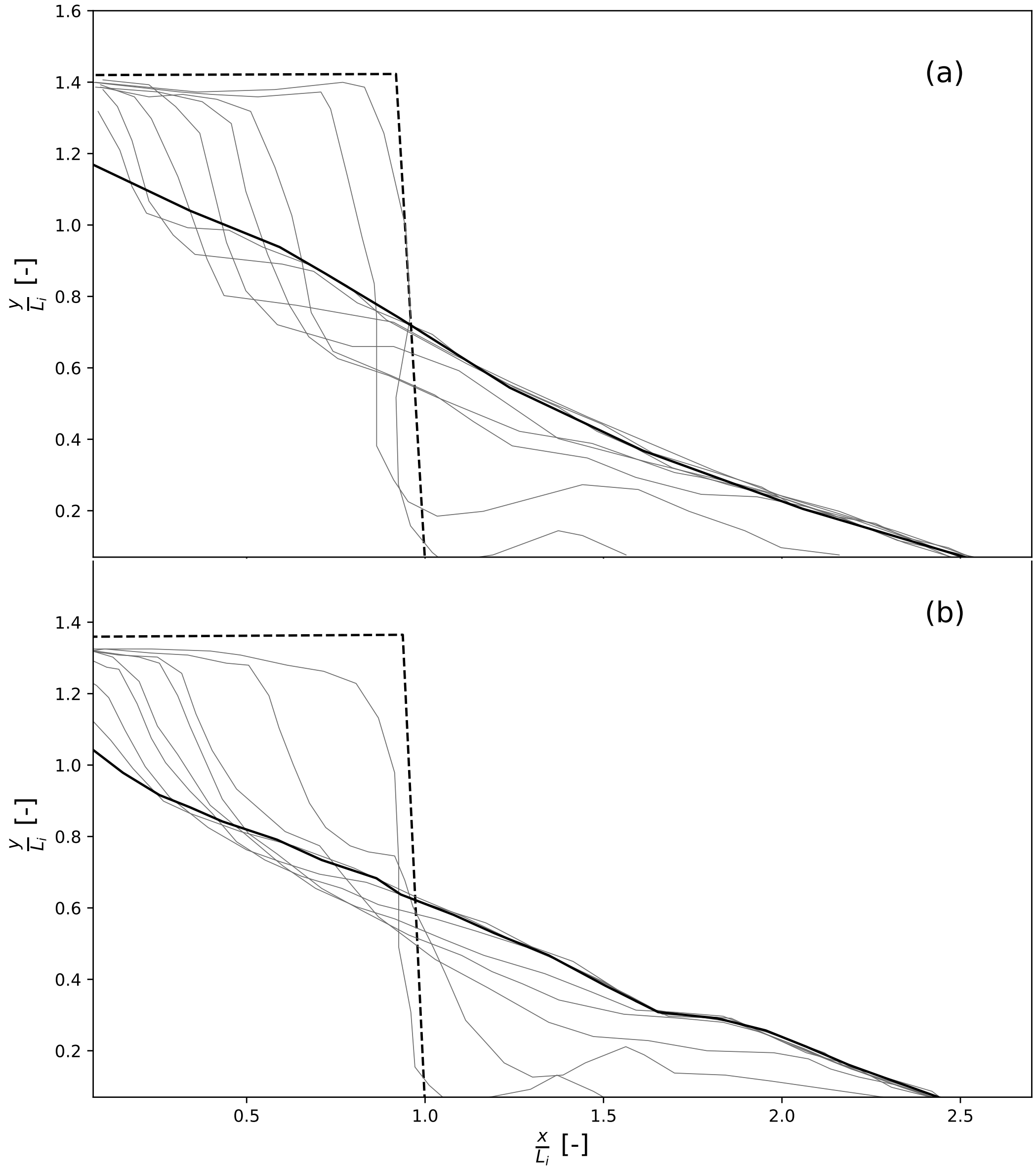

Figure 9.8: Collapse of a dense and a loose column containing the same amount of sand for an aspect ratio $A \simeq 1.5$, and with $\Delta t_{step} = t_{\infty}/9$.
(a) Dense : $\phi_i \simeq 0.63$, $L_i = 14.0$ cm, $H_i = 21.5$ cm, 1.67 s between profiles and $t_{\infty} = 15.07$ s;
(b) Loose : $\phi_i \simeq 0.569$, $L_i = 16.5$ cm, $H_i = 24.5$ cm, 1.55 s between profiles and $t_{\infty} = 13.95$ s

seen in literature in Section 7.2. Both columns have a similar runout distance and $\Delta t_\infty = 1.12$ seconds only. We conclude from these observations that the column we consider loose is not as loose as we thought. Following the literature, it should collapse faster and further.

These differences can be explained by the fact that, in the literature, they use glass beads as particles. These beads are more likely to roll and slide further. Sand grains does not have the same size and shape meaning that the compacting, when simply pouring the granular media in water, is not the same as for perfectly spherical elements. Moreover, we use a shovel to pour the sand in the channel, and thus the sand falls in by blocks and is not poured like a fluid. When shoveling the sand in, we create unwanted vibrations by hitting structural elements. These could lead to sand packing in the column.
The association of the column with an initial volume fraction of $\phi_{i,loose} = 0.569$ is not always correct. Indeed, as a result of our previous observations, this column seems to be a little denser than we thought. It confirms the difficulty of estimating experimentally an initial volume fraction when conducting experiments on the channel.

9.1.3 With respect to the size of the grains

Another parameter that influences the collapse behavior of a granular column is the type of grains used, as explain in Section 7.3. In this thesis, one specifically works with sand as the granular material. That allows us to manipulate only the type of sand used in the experiments. So far, we have only worked with the finer type of sand. Now, we will compare its behavior with a sand with coarser grains. Although both types of sand are described and characterized in detail in Section 8.4, the specific characteristics of each sand type are briefly summarized in Table 9.2.

	FINER SAND	COARSER SAND
Range [mm]	[0,2]	[0,3]
Mean diameter $\overline{d}$ [mm]	0.275	1.363
Median diameter d_{50} [mm]	0.367	1.73

Table 9.2

We will compare and analyze the differences in the time evolution of two columns composed of these two distinct types of sand: the finer one and the coarser one.

Both columns have an aspect ratio $a = 1.75$.

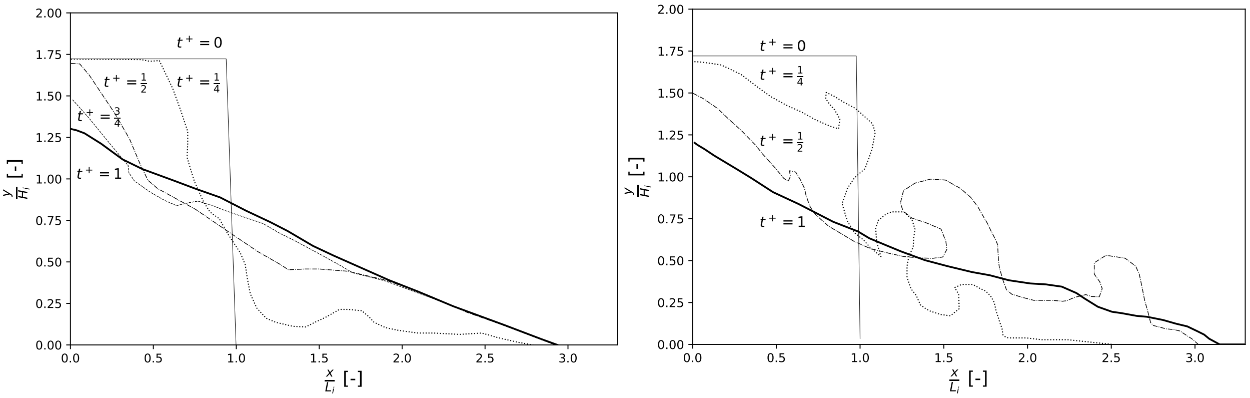

(a) Finer sand $d_{50} = 0.41$ (b) Coarser sand $d_{50} = 1.71$

Figure 9.9: Evolution of the column profile over time for two different types of sand. The axes are dimensionless and one remembers that $t^+ = \frac{t}{t_f}$ where t_f is the collapsing duration, i.e, when the column is at rest.

In Figure 9.9, we can clearly observe the significant differences in the behavior of the collapse. Indeed, when using the sand with coarser grains, we notice the apparition of vortexes all along the collapse. For a better visualization of these, the reader may refer to Figure 9.10.

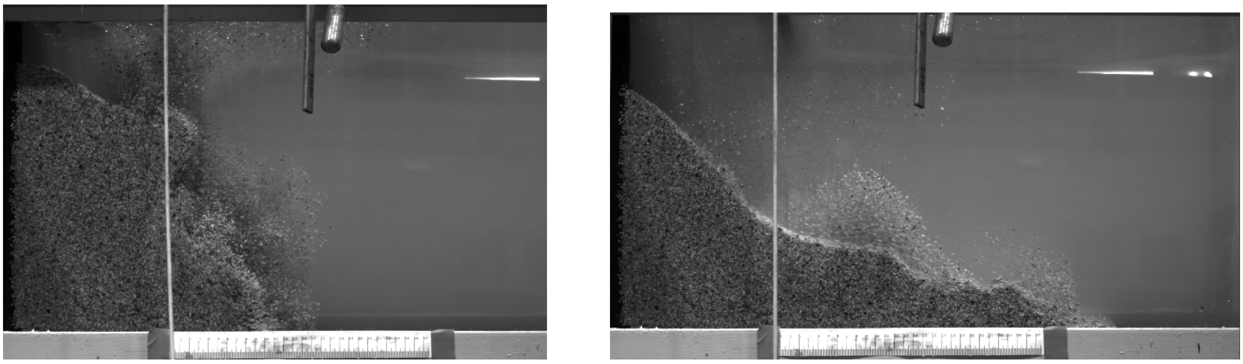

(a) $t^+ = \frac{1}{4}$ (b) $t^+ = \frac{1}{2}$

Figure 9.10: Evolution of the column profile over time for two different types of sand. The axes are dimensionless and one remember that $t^+ = \frac{t}{t_f}$ where t_f is the collapsing duration, i.e, when the column is at rest.

With Figure 9.11, we can observe more precisely the final deposit of the two columns and all the important ratios and parameters are synthesized in the Table 9.3.

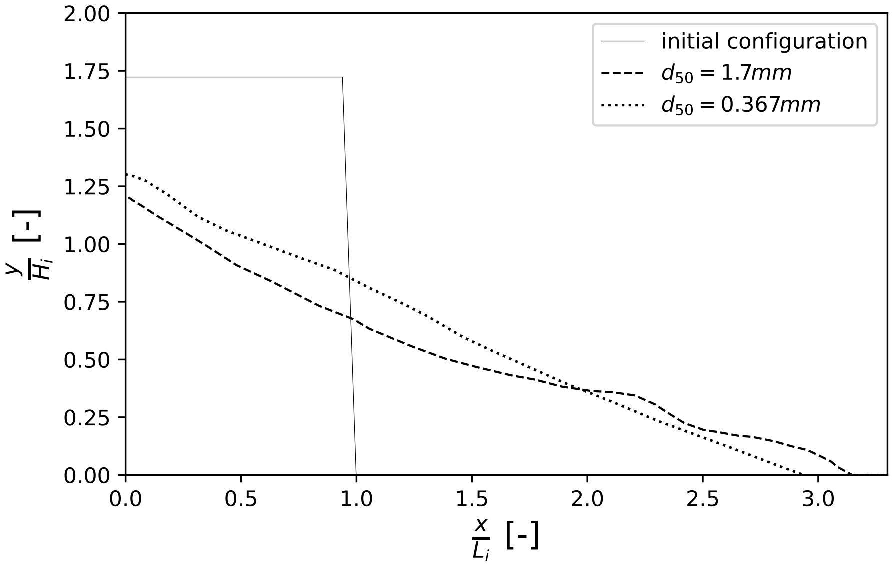

Figure 9.11: Comparison of the final deposit between the two types of sand.

Comparison summary of the two experiments $a = 1.75$	TYPE OF SAND		
	FINE SAND	COARSE SAND	Variation
Range [mm]	[0,2]	[0,3]	-
Mean diameter $\overline{d}$ [mm]	0.275	1.363	+395%
Median diameter d_{50} [mm]	0.367	1.73	+371%
Runout distance L_∞ [-]	1.95	2.134	+9.43%
Ratio $\frac{L_i}{\overline{d}}$ [-]	589.09	124.75	-78.82%
Ratio $\frac{H_f}{H_i}$ [-]	0.748	0.694	-7.7%
Collapsing duration t_f [s]	18.03	2.24	-87.57%
Repose angle α [°]	27.23	29.4	+7.96%

Table 9.3

The runout distance L_∞ and the ratio $\frac{H_f}{H_i}$ are almost identical for both types of sand, with a difference of approximately $+9.43\%$ and -7.7% respectively. These observations align with the results discussed in Section **??**. In fact, the system-size to grain-size ratio ($\frac{L_i}{\overline{d}}$) exceeding 75 suggests that there should not be significant

grain-size effects. Moreover, our ratio and value for the run-out distance also agree with the numerical values in the Table 7.3.
We can notice that the angle of repose if greater for the coarser sand than with the finer sand. This corroborates results obtained by Chik, Zamri and Vallejo [83] and by Hamzah M. Beakawi *et al.*[84]. They reported that the angle of repose for a mixture with predominantly coarse sand is greater than the one for a mixture with predominantly fine sand.

In summary, based on our parametric analysis regarding the grain size, we conclude that due to the high system-size to grain-size ratios, we do not observe significant differences in the shape of the final deposit between the two columns. Nevertheless, the behavior during collapse is substantially different between the two types of sand. Specifically we observe an accentuation of vortices with a coarser sand.

9.1.4 Presence of a sand bed

In all the previous experiments, we never have a sand band downstream of the door. If we observe the numerical simulation, there is a sand bed all over downstream of the door. In fact, it is easier to have the latter for the boundary conditions and setting a constant value of ϕ_s in this region.

We were wondering what was the influence of this sand bed on the behavior of the collapse of the granular column, so we analyzed the difference in final deposit between an experiment where we had a sand bed and one without. The results can be seen in Figure 9.12, 9.13 and 9.14.

We directly observe that the final deposit has a similar shape over its length but we clearly notice slight differences at the end of the final deposits shape. By zooming on our region of interest (see Figure 9.14), one observes that the final deposits of the experiments without a sand bed tends to go further than the one with a sand bed.

One could deduce that the grains of sand, in contact with the smooth surface of the channel, "roll" on it, carrying them further away. Whereas this rolling movement is limited by the sand bed in the other experiment.

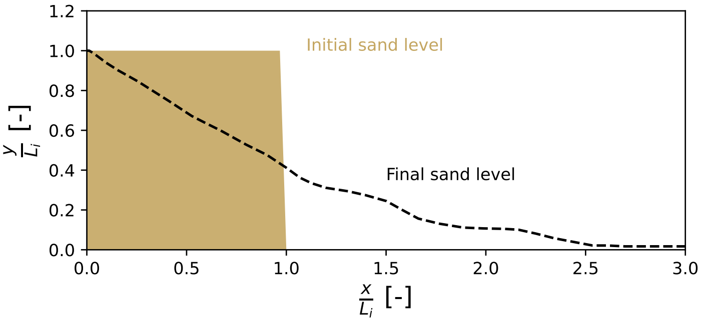

(a) Without a sand bed

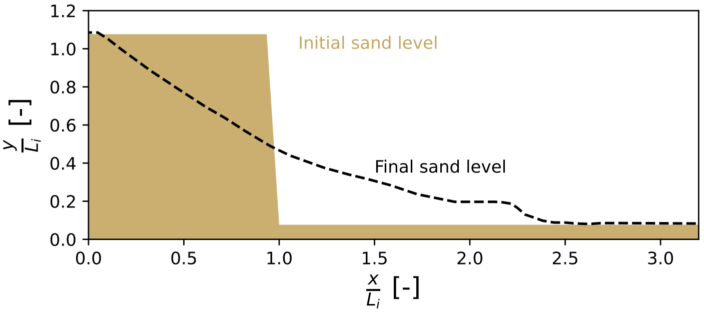

(b) With a sand bed

Figure 9.12: Final deposits of collapse of a columns of aspect ratio $a = 1$, with the $d_{50} = 1.76$ sand median diameter

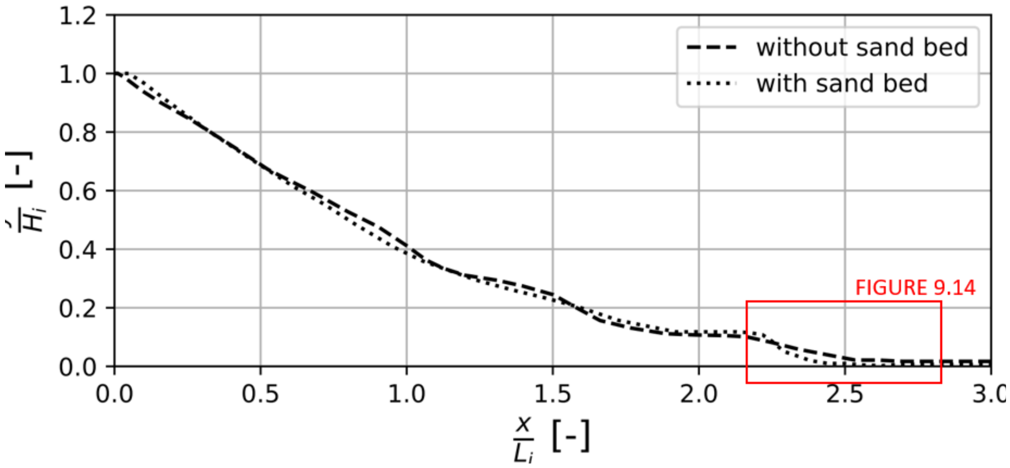

Figure 9.13: Comparison of the final deposit of two collapses, taking into account the presence or absence of a sand bed, with same parameters as Figure 9.12.

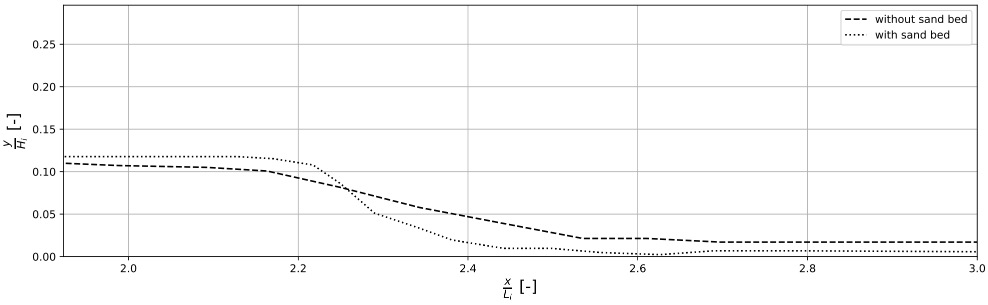

Figure 9.14: Zoom of the region of interest of Figure 9.13

9.2 Velocity fields analysis through DaVis 8

In this section, we will analyze our results with the software DaVis 8. As previously mentioned in Section 8.5.4, the presence of the moving cable in the recording causes problems in the detection of the moving particles. Therefore, the amount of analyzable images is limited.

Aspect ratio

First we analyzed the beginning of the collapse of the sand column for multiple aspect ratio a to highlight the collapse at the failure surface. Figure 9.15 presents analyses of the column's falling velocity for aspect ratios 1, 1.5 and 2. The vectors correspond to moving particles, so we can see the sliding of the volume of sand above the failure surface, as already observed in Section 7.1. For aspect ratio 2, the collapse velocity appears to be slightly higher, at around 0.1 m/s, compared with the other two, where it's more in the region of 0.045 m/s.
When the aspect ratio is increased, with $a = 2.95$ and $a = 3.85$, the observed phenomenon is not the same as presentend in Figure 9.16a and 9.16b. Whereas with lower aspect ratios, Figure 9.15 highlights the collapse of the failure surface, here we observe a progressive erosion of the column's right lateral surface. This phenomenon starts at the top right-hand corner and works its way down to the bottom of the column. In fact, the grains detach themselves from the rest of the column and fall away on their own. Unlike the failure surface, where the sand falls in blocks. Note that this does not mean that there is no failure surface when there is erosion, or vice versa! In order, here's what happens after the door is opened: erosion starts and lasts about 1 second and only then does the volume on the failure surface begin to fall. What we observe is that the quantity of sand eroded is proportionally greater for columns with higher aspect ratio. We also observe that the particles falling by erosion are much faster ($\sim$ 0.8 m/s) than the volume

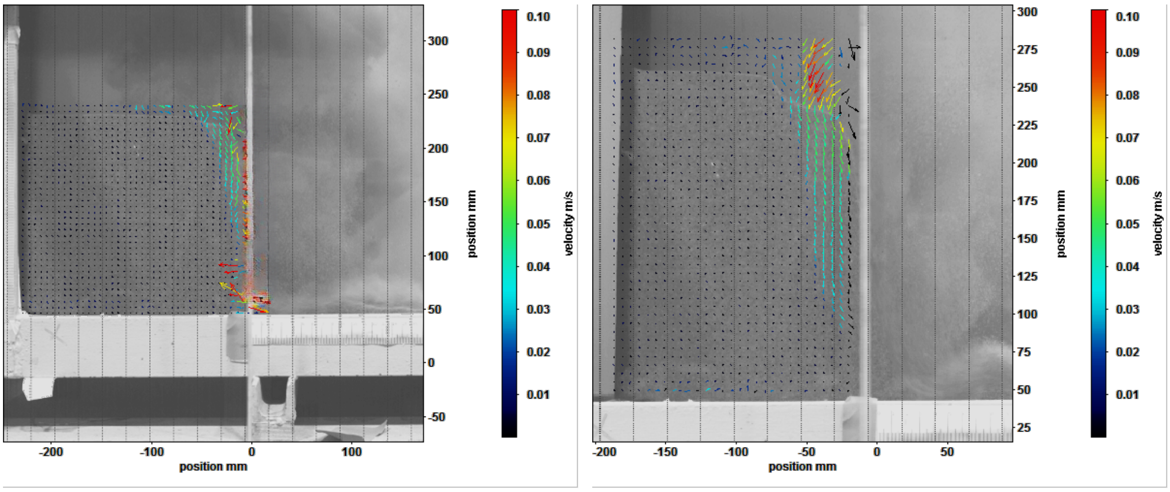

(a) Aspect ratio $a = 1$, at $t = 1.72$ s (Cable velocities have been removed)

(b) Aspect ratio $a = 1.5$, at $t = 1.8$ s

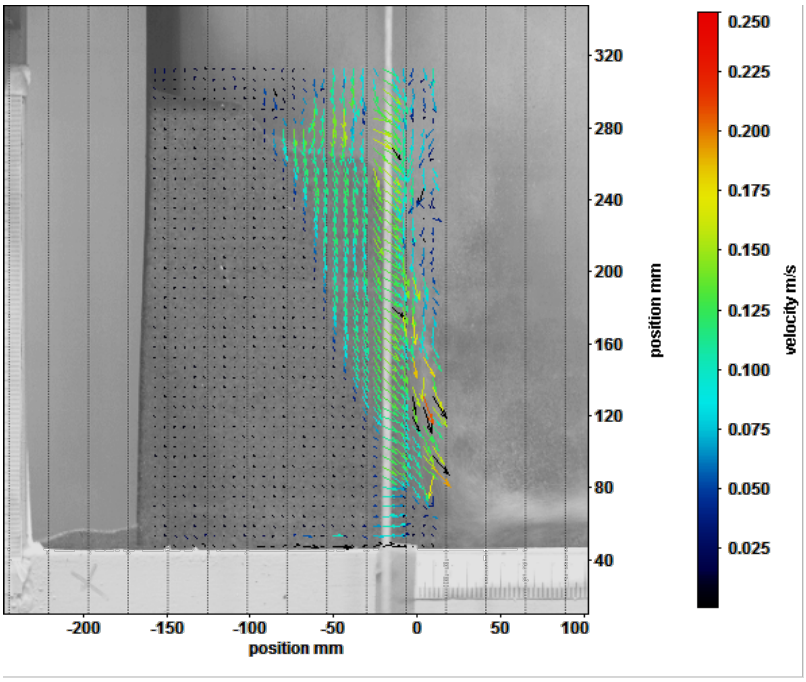

(c) Aspect ratio $a = 2$, at $t = 2.02$ s

Figure 9.15: PIV analysis of the collapse beginning for aspect ratios $a = 1$, 1.5, 2

of sand falling at the failure surface.

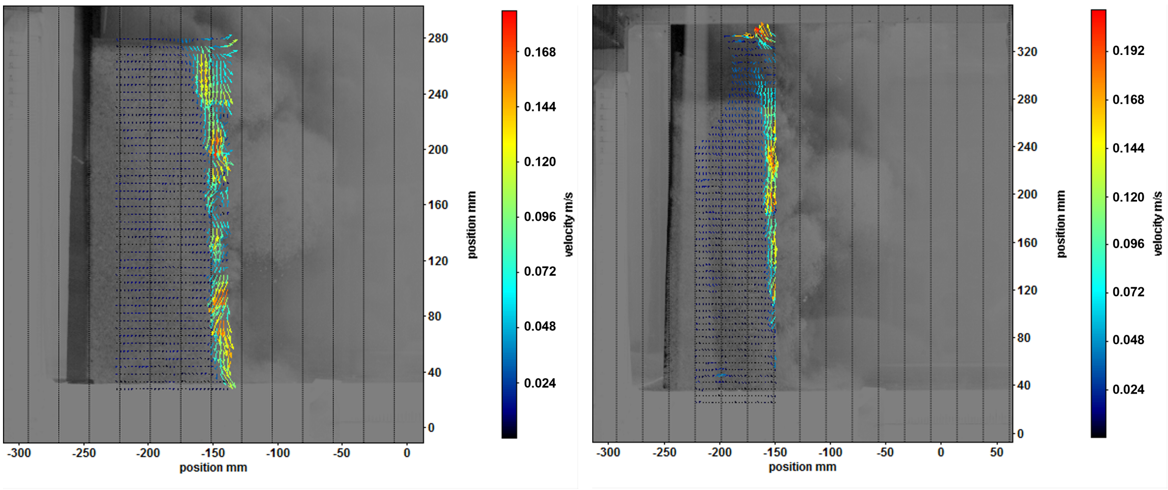

(a) Aspect ratio $a = 2.95$, at $t = 0.47$ s

(b) Aspect ratio $a = 3.85$, at $t = 0.68$ s

Figure 9.16: PIV analysis of the collapse beginning for aspect ratios $a = 2.95$, 3.85

Vortices

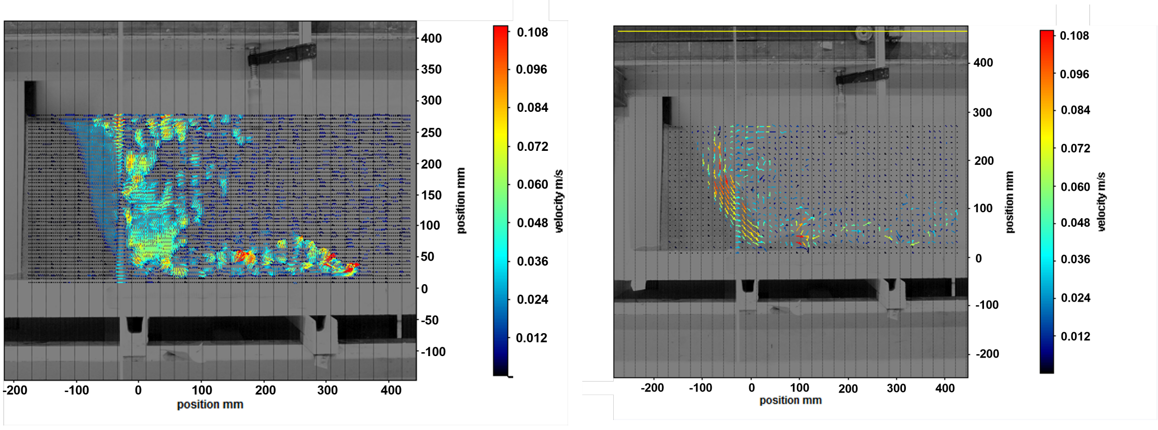

(a) Initial motion in the sand column

(b) Motion in the sand column after 2.0 s

Figure 9.17: PIV analysis of the collapse for aspect ratio $a = 2$ and grain median diameter is $d_{50} = 0.41$ [mm].

Figure 9.17a shows the volume of sand beginning to fall along the failure surface. But we can also see the velocities of the particles set in motion, in particular, the particles put into suspension by the opening of the gate, but also the particles dropped by erosion. Then, in Figure 9.17b, we can see that the volume of sand detached from the failure surface comes into contact with the bottom of the channel. This creates the beginnings of recirculation and therefore of a slight vortex in the lower part of the channel. Of course, these vortices are much less intense than when using coarser sand.

Figure 9.18 shows that when using coarser-grained sand, vortices are much more evident. We know that the duration of the collapse is also shorter for this sand, and on the PIV, this is translated into higher velocities. We can also see that 2 vortices are created. One appears at the point where the column comes into contact with the bottom of the channel, and the other in the center region of the collapse. At the end of the collapse, these 2 vortices disappear to make way for the final deposit.

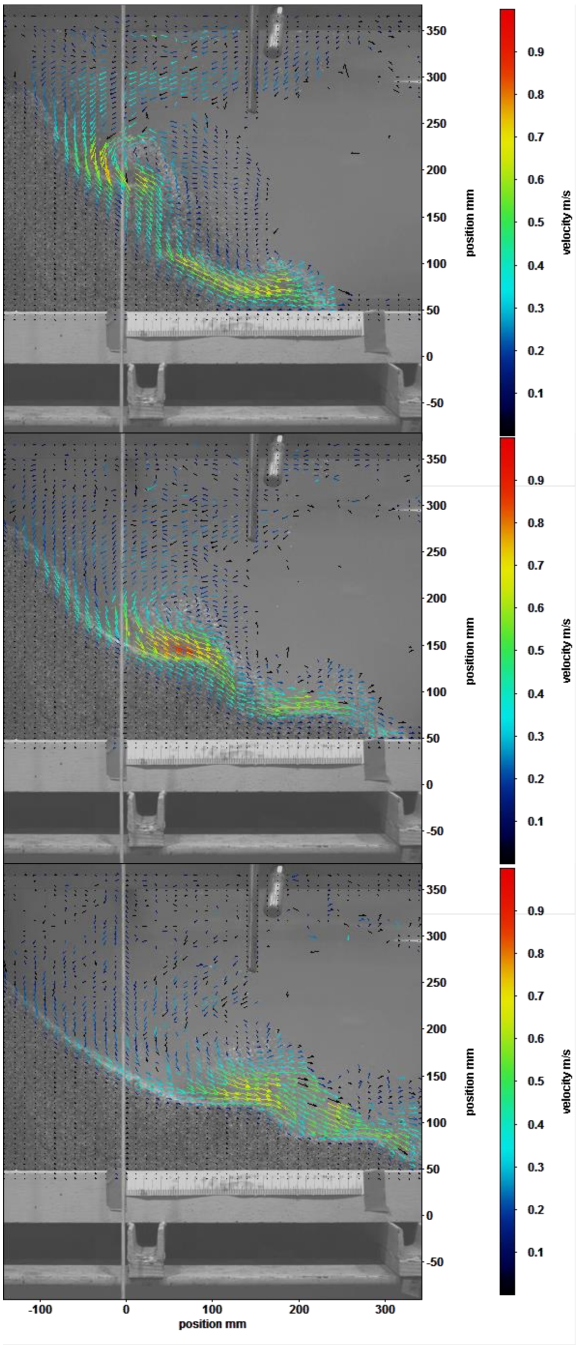

Figure 9.18: PIV analysis of the collapse for aspect ratio $a = 2$ and grain median diameter is $d_{50} = 1.73$ [mm].

Air bubbles

It was during the PIV analysis that we realized that there were particles moving vertically above the sand column as the collapse traveled along the bottom of the channel (see Figure 9.19). After analyzing the images, we realized that these were in fact fine air bubbles trapped in the column that had been released by the collapse and were therefore escaping towards the water surface (see Figure 9.20).

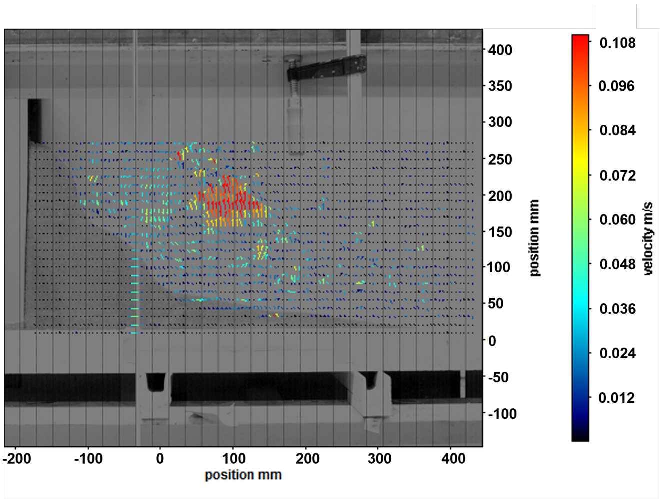

Figure 9.19: Air bubbles motion seen through PIV analysis.

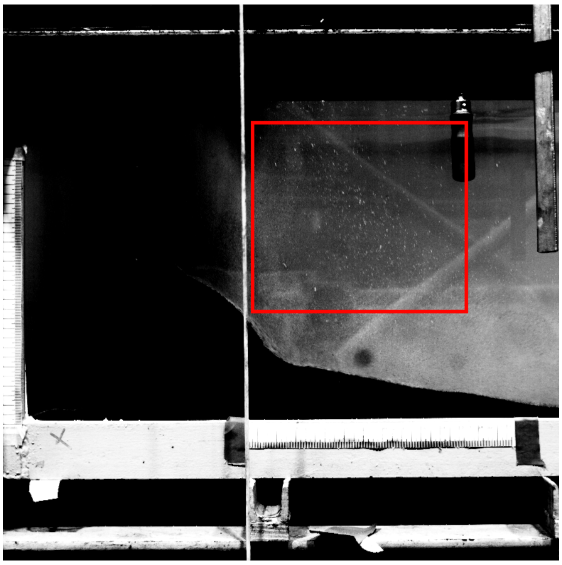

Figure 9.20: Presence of air bubbles highlighted by darkening the photo of the channel

9.3 Comparison with experiments from the former setup

In this section we will compare our experimental results to the one obtained previously by Flora in her master thesis [6]. Firstly, we will compare the collapse of a column with an aspect ratio $a = 1$, a sand with a median diameter of 1.7 [mm] and a sand bed initially set on the bottom of the channel. In Figure 9.22, we observe similar behaviors, for both cases, a vortex is created when the collapse reaches the bottom of the channel. In our case, it seems that two vortices are created, one at the bottom and an other one in the center region of the collapse. It also seems that Flora's vortex is more defined/has a more evident recirculation. In the two experiments, what differs is the initial dimensions. The previous experiment has $H_i = L_i = 150$ [mm] and ours has $H_i = L_i = 245$ [mm]. This difference of initial dimensions could explain this observation and it would be interesting to conduct experiments on the influence of the latter on the column collapse behavior for same aspect ratios.

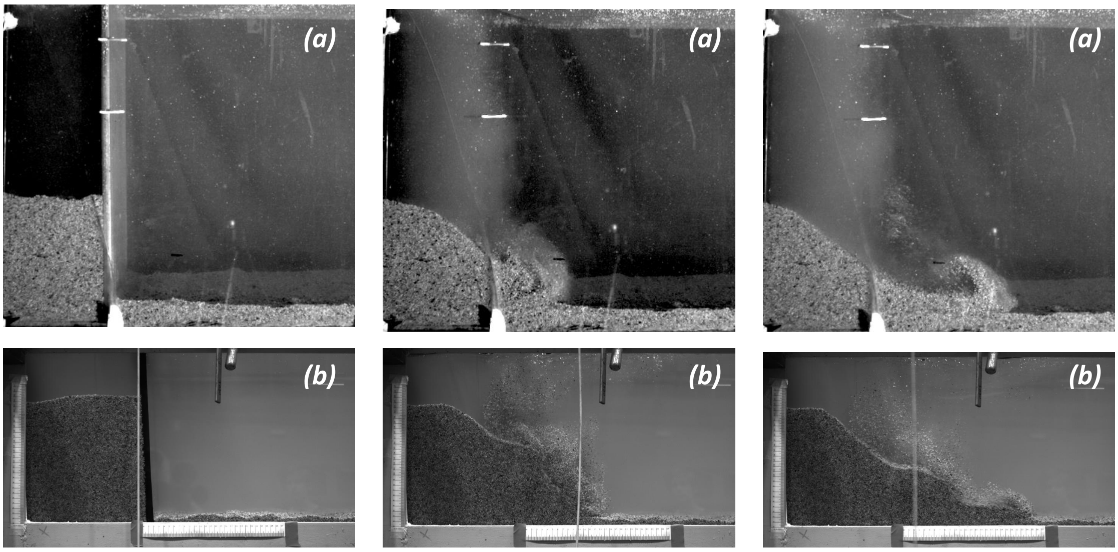

Figure 9.21: Successive stages of collapse of a column of aspect ratio a = 1. (a) Flora's results; (b) our results

Our final deposit has a slight trapezoidal shape whereas Flora's is a triangle. The deposit angles and the dimensionless final length ($= \frac{L_f}{L_i}$) are similar.

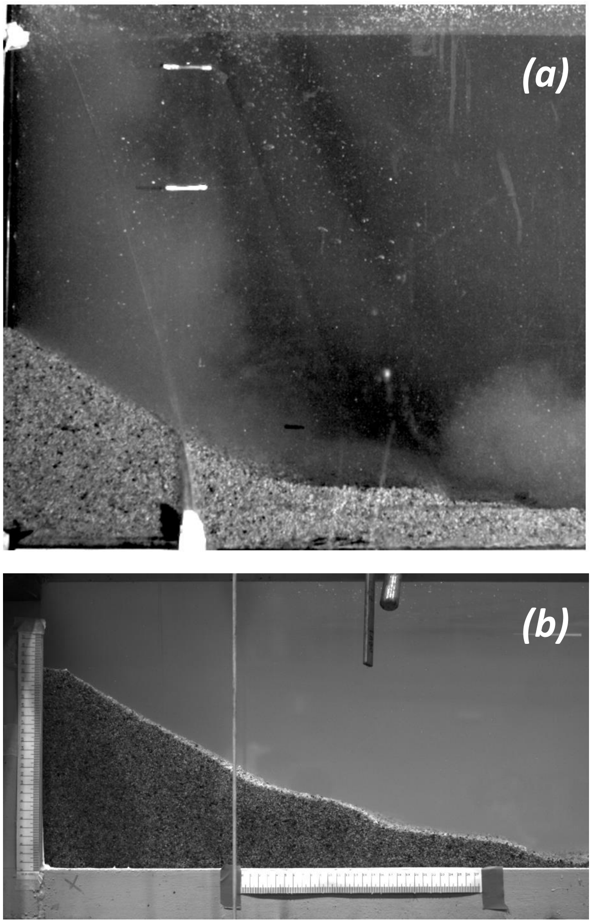

Figure 9.22: Final deposit of a column of aspect ratio a = 1. (a) Flora's results; (b) our results

When looking at Figure 9.23, we also observe that the right region of the final deposit obtained through the experiments of the former channel is flatter than ours.

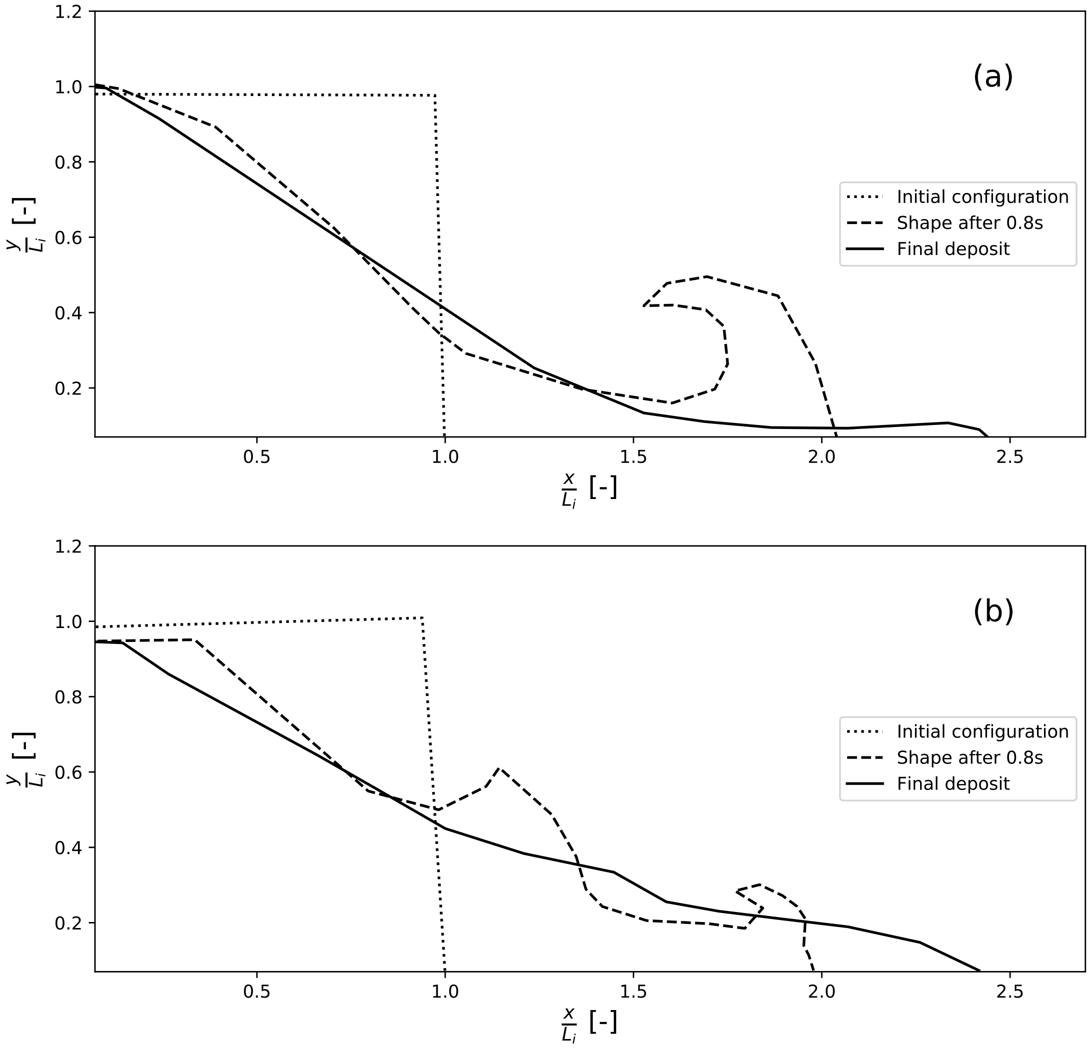

Figure 9.23: Comparison of experimental shapes observed in a column collapsing with aspect ratio a = 1. (a) Nennen (2021) [6]; (b) Our results.

10

Comparison with numerical simulation

This chapter focuses on comparing the results obtained from our experiments with the numerical simulations based on the model explained in Chapter 6.

The simulations use various types of sand, each characterized by its median grain diameter (d_{50}). The following ones are used in the simulations:

- $d_{50} = 0.56$ mm
- $d_{50} = 0.225$ mm
- $d_{50} = 1.72$ mm

It has been indicated that the assumption of a continuous medium was no longer valid with the value of $d_{50} = 1.72$ in the numerical model and may lead to simulation errors. Therefore, we decided to not compare the experiments conducted with this grain size and to compare with a sand type that has the closest d_{50} value from our others experiments. It turns out to be $d_{50} = 0.56$. The sand used in our experiments had an initial d_{50} of 0.367 mm, but due to multiple reuse cycles in water (as demonstrated in Section 8.4.1), it reaches a d_{50} of 0.41 mm.

10.1 Final deposits shape

To facilitate a meaningful comparison between the numerical simulations and the experiments, we need to know our initial volume fraction. As we explained in Section 7.2, estimating the initial volume fraction precisely during an experiment is challenging and difficult. Some laboratory experiments were conducted to estimate it (see Section 8.3). Primary results indicated that a non-compacted column with our sand ($d_{50} = 0.367$) would have an initial volume fraction of $\phi_{s,i} = 0.569$. whereas a compacted column (dense), would have an initial volume fraction of $\phi_{s,i} = 0.630$.

However, as this remains just an approximation of the initial volume fraction, we will compare the results of the numerical model for different values of the initial volume fraction. We observe how our column behaves, whether it tends towards a denser or looser collapse behavior. Figure 10.1 illustrates the latter by comparing the final deposits of columns with aspect ratio $a = 2$ obtained from numerical simulations, using different initial volume fractions, with our experimental result. In our experience, we ensure to obtain the loosest column possible, with an estimated initial volume ratio of $\phi_{s_i} = 0.569$

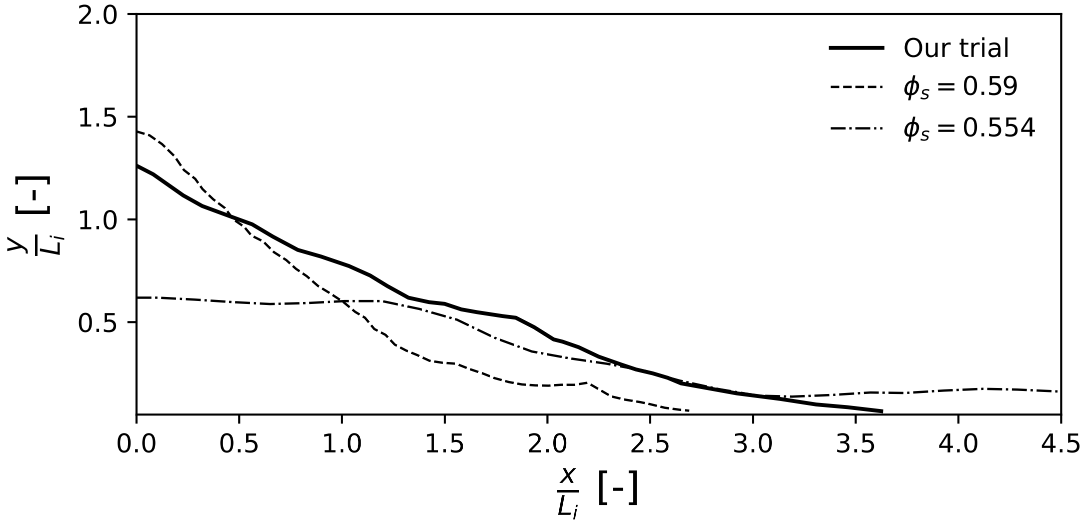

Figure 10.1: Final deposit of column $a = 2$ using different ϕ_{s_i} with numerical simulations[38], the solid line represents our experimental result.

When comparing the shape of the final deposit of our experimental results with the numerical ones, it becomes apparent that our experimental column exhibits a final deposit shape that falls between the numerical boundaries represented by a very loose column ($\phi_s = 0.554$) and a fairly dense column ($\phi_s = 0.59$). This suggests that our column's behavior lies somewhere in between these two final deposits shapes. It seems that the experimental estimate of our initial volume fraction $\phi_{s_i} = 0.569$ appears to be quite close to the numerical results.

We also observe that for this same aspect ratio, we obtain a runout distance

L_∞ smaller than for the looser column but larger than the denser column. Figure 10.2 illustrates the comparison between the numerical results and the experimental ones in terms of the dimensionless runout distance L_∞ for various aspect ratios.

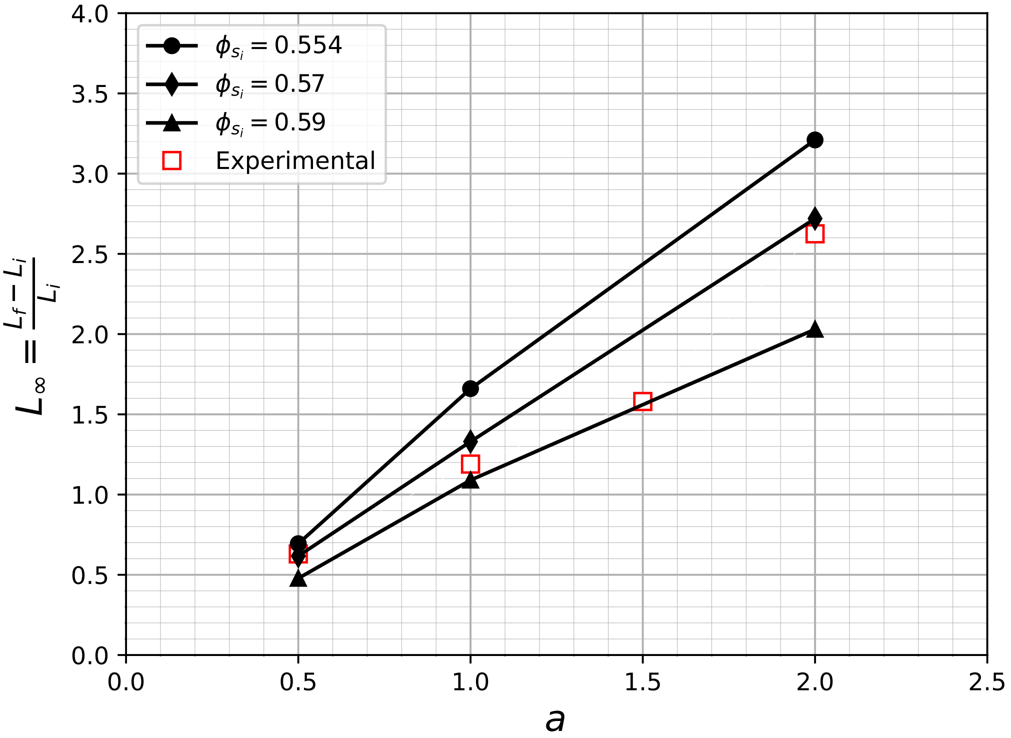

Figure 10.2: Dimensionless runout distance, L_∞, for different aspect ratios a and initial volume fractions $\phi_{s,i}$ with numerical simulation[38]. Our experimental results are represented in red squares.

Figure 10.2 demonstrates fairly similar results between the numerical simulations and our experimental values. Indeed, when comparing our experimental results with the numerical results with an initial fractional volume $\phi = 0.57$, for the aspect ratios $0.5 - 1 - 2$, the average difference between our results and the numerical results is approximately 5.31%. Notably, for aspect ratio $a = 1.5$, our experiment aligns better with the numerical result for a value of $\phi_{s,i} = 0.59$.

Several assumptions can be made to explain this difference. Firstly, the lack of a specific numerical value for aspect ratio 1.5 makes it uncertain whether the linearity observed between aspect ratios 1 and 2 holds true. Therefore, it is possible that aspect ratio 1.5 behaves differently between these two values. Secondly, achieving the same initial volume fraction for each column is difficult (see Section 9.1.2), and the experiments conducted with these aspect ratios may have resulted in a denser configuration.

Another criteria of interest to characterize the shape of the final deposits is the ratio between the final height and the initial height of the column, $\frac{H_f}{H_i}$. In Papalexandris *et al* (2022) [38], they only provide the ratio between the final height and the initial length, $\frac{H_f}{L_i}$. However, since $\frac{H_f}{H_i} = \frac{H_f}{H_i}\frac{L_i}{L_i} = \frac{H_f}{L_i}\frac{L_i}{H_i} = \frac{H_f}{H_i}\frac{1}{a}$, our criteria can be found straightforward. Both of these criteria are presented in Figure 10.3

In summary, we observe that our experimental results align with the trend of the numerical results. However, there is a difference of behavior between the runout distance and height criteria. While the runout distance criterion tends to align our experiments results with an initial fraction volume of $\phi_{s_i} = 0.57$, the experimental results obtained for the height criterion tend to follow the numerical curve associated with an initial volume fraction of $\phi_{s_i} = 0.59$.

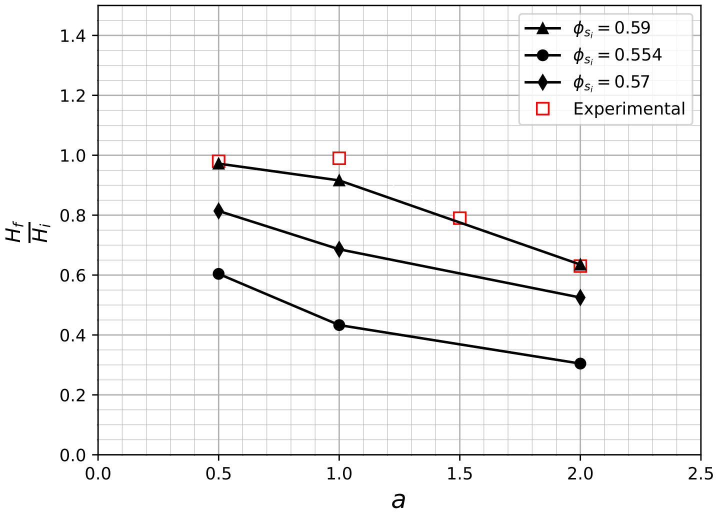

(a) Ratio between final height and initial height, $\frac{H_f}{H_i}$

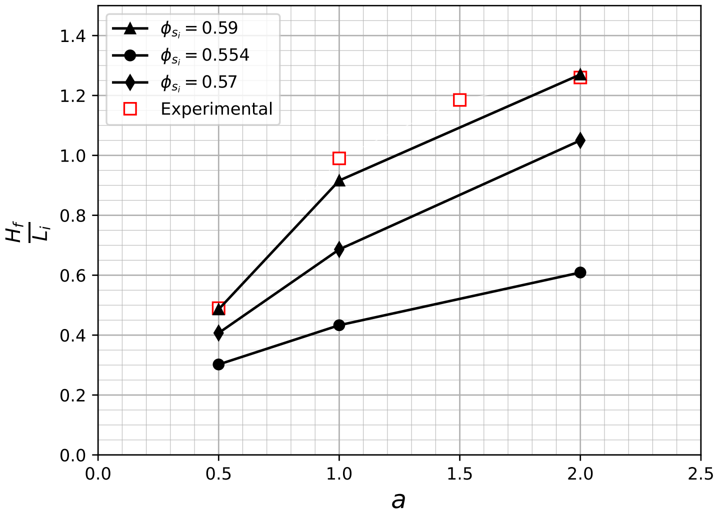

(b) Ratio between final height and initial length, $\frac{H_f}{L_i}$

Figure 10.3: Several ratio for different aspect ratios a and initial volume fractions ϕ_{s_i} with numerical simulations [38]. Our experimental results are indicated by red squares.

10.2 Collapse features

The previous section highlights the behaviors of the shapes of the final deposits of the column. This section compares the collapse characteristics of the columns over time.

A first comparison between the numerical simulations and the experimental results is available in Figure 10.4. To better compare the simulation times with real times, we have scaled the time with $t^+ = \frac{t}{t_f}$ where t_f is the time of collapse of the column. Since we only had numerical collapses for densely-packed columns ($\phi_s = 0.59$) or loose-packed column ($\phi_s = 0.554$), we chose to compare with the densely-packed column. Indeed, its behavior seemed to be the closest to our experiments, following the comparisons done in the previous Section 10.1.

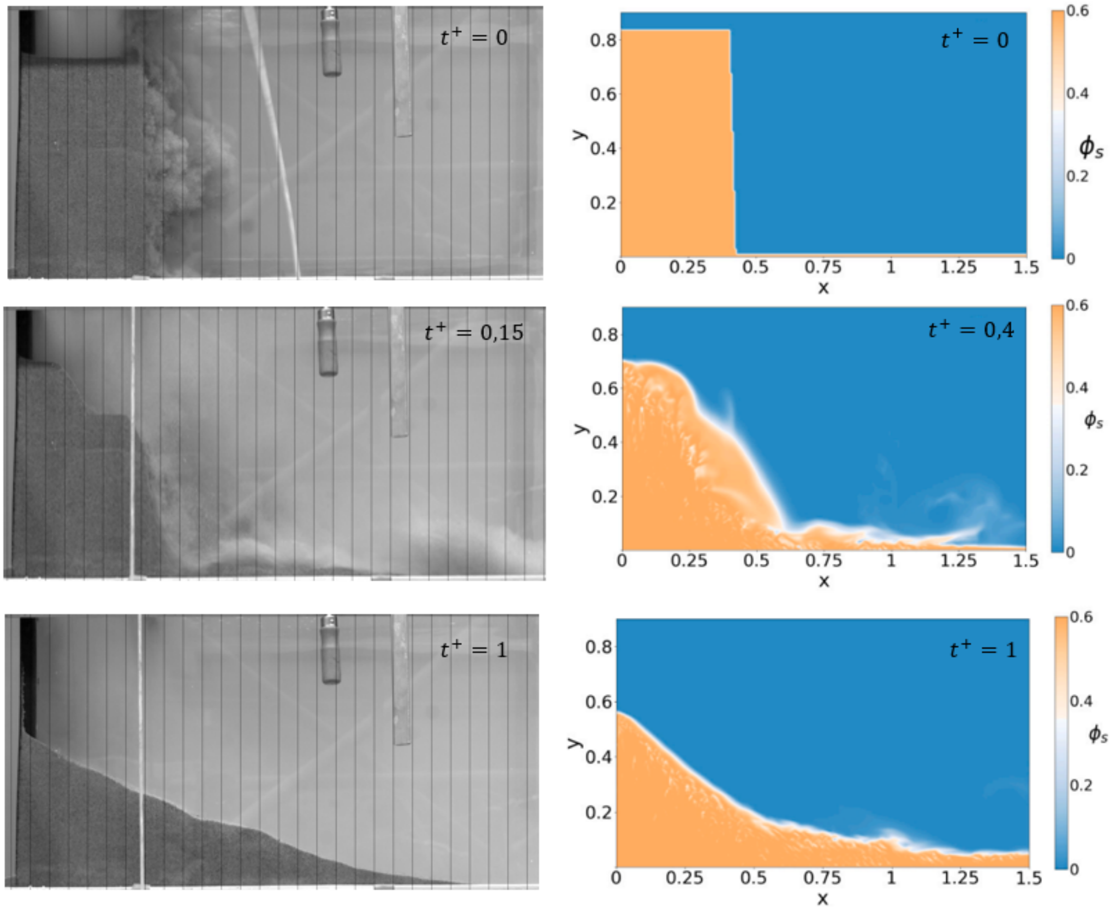

Figure 10.4: Collapse of densely-packed ($\phi_s = 0.59$) columns. Comparison between our experiments (left) and numerical simulation from [38] for aspect ratio $a = 2.0$.

Figure 10.4 illustrates that the columns exhibits, at first glance, broadly similar collapsing behavior. The main differences are observed in the collapse time. The experimental column falls much faster than the numerical simulation. Moreover, we observed in experimental collapses that the corner of the columns comes down, followed by slippage along the failure surface, while the left side initially remained at nearly the same height as the initial height. This disengagement and slippage seem to be less noticeable in the numerical simulations, at least on a smaller scale. Slippage can also be seen along a fracture surface, but the height of the column seems to fall at the same time the slippage occurs. This observation is confirmed by Figure 10.5, clearly showing that the height of the numerical column is falling faster than the experimental one during the first half of the collapse. It is during this first time of the collapse that we observe the slippage on the experiment column. However, as the collapse progresses, the behavior of the two columns appear to converge and exhibit similar variations in height during the latter half of the collapse. This suggests that the behavior of the numerical column catches up with the experimental column over time, in terms of heights ratio.

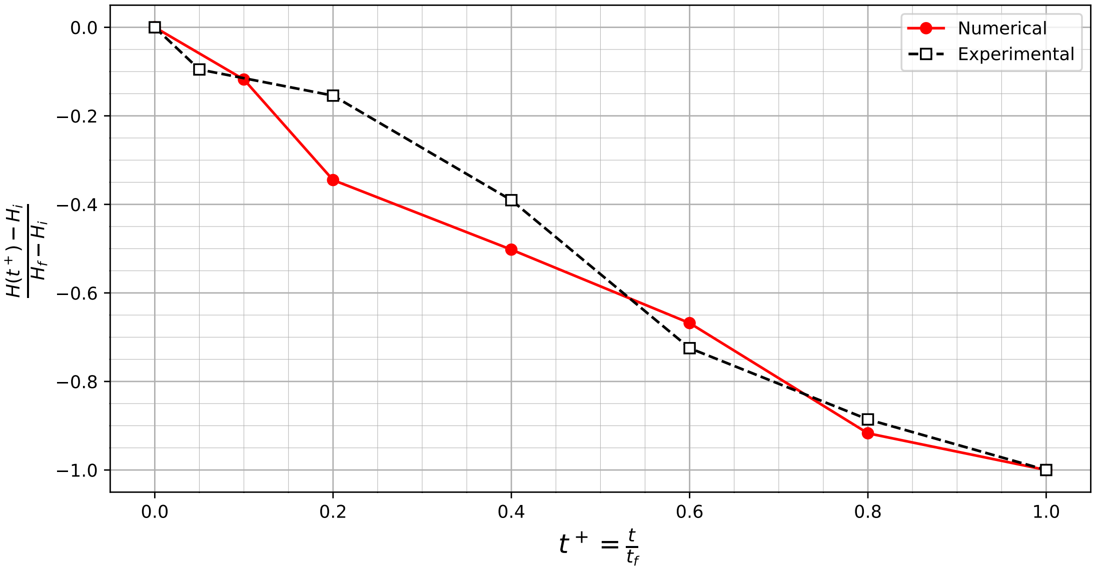

Figure 10.5: Evolution of the heights ratio over time in the case of densely-packed columns ($\phi_{s_i} = 0.59$)[38] Our experimental results are indicated in dashed lines.

Another observation, which was previously observed in the analysis of our experimental results in Section 9.1.1, is that we reach the runout distance relatively quickly. Indeed, at $t^+ = 0.15$ we are already close to the distance reached in $t^+ = 1$. This is in contrast to the behavior observed in the numerical simulations. At $t^+ = 0.4$, the numerical simulation has not yet reached its runout distance. To corroborate these observations, the comparison of the evolution of the dimensionless runout distance over time, for different aspects between the numerical and experimental results, is shown in Figure 10.6.

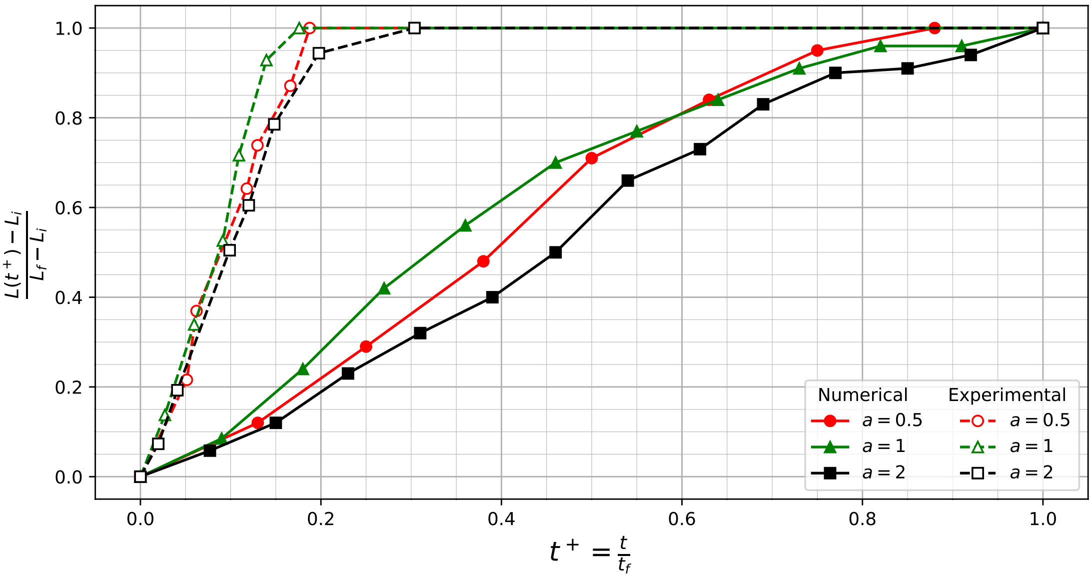

Figure 10.6: Evolution of the normalized runout distance over time for three different aspect ratios a in the case of densely-packed columns ($\phi_{s_i} = 0.59$)[38] Our experimental results are indicated in dashed lines.

The observations drawn from the comparison between the two collapses are clearly observed. While numerically the column reaches its runout distance relatively linearly with respect to the scaled times, experimentally we observe a much faster convergence towards the runout distance. The experimental column seems to reach its runout distance first, and then only starts to lose height, whereas the numerical column seems to loose height at the same time as its length increases.

In conclusion, the comparisons between the final deposit shapes obtained from numerical simulations and experimental observations show good agreements, indicating that the numerical simulations provides a good approximation of the final shape. However, the characteristics of the collapse over time are quite different. The numerical simulations show a slower progression towards the runout distance compared to the experimental observations, whereas the column reaches its runout distance relatively quickly. Here are some hypotheses to help explain the origins of these differences.

- The type of sand used in the experiments is not exactly the same as the one used in the simulations. We have shown that experimentally we have a slightly grain size effect in terms of collapse features, as shown in Figure 9.9. Numerically, we also observe a grain-size effect as represented in Figure 10.7, presenting the different in the shape of the final deposits for two types of sand.

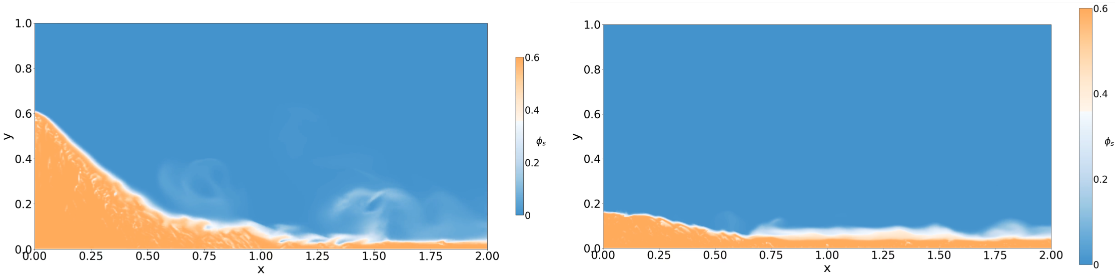

(a) $d_{50} = 0.56$ mm (b) $d_{50} = 0.225$ mm

Figure 10.7: Comparison of the final deposits of two different types of sand with $\phi_{s_i} = 0.59$ and $a = 2$ with numerical simulations [38]

- The difference for the height ratio can arise from a wall effect with the upstream door holding the column.

- The difference for the runout distance can also arise also a wall effect with side windows of the channel.

- The numerical model may not accurately capture the dynamic aspects of the collapse process. The sand is numerically represented as perfect spheres, which is not the case in reality.

This page is intentionally left blank.

Conclusion

Through this thesis we are proud to have been able to contribute our grain of sand to the understanding of granular media.

To achieve this goal, the state of the art has provided valuable context for our work, revealing the evolution of research on granular media from an empirical approach to deeper fundamental understanding of its physical mechanisms. This multidisciplinary discipline continues to be an active area of research with diverse applications in many fields.

The first part of the thesis focused on designing a mechanical system to study a precise configuration of granular flows.

Chapter 2 presented the context of this design by discussing about the limitations of the former design, such as the free surface, the pneumatic mechanism, and sealing, and by emphasizing the new system requirements.

Chapter 3 presented the process followed for designing the system. It includes the understanding of the requirements and constraints and finding several suitable solutions to solve the problematic. Once these solutions are adequate, the dimensioning phase allowed to get the main dimensions of the future system.

The Chapter 4 presented an overview of the final design from its 3D CAD model to the pictures of the system after its physical assembly. It has shown that when assembling a system, adjustments may occur to deal with situations that were not anticipated during the design phase. Assembling the system ourselves really gave us a different perspective on system design. For instance, by learning about the manufacturers' expectations and limitations we highlighted relevant points to take care to while designing.

Chapter 5 concluded the first part by validating our mechanism related to the predefined functions and constraints. A study of the average opening time for comparison with an instantaneous criterion was carried out. Additionally, it has been shown that the variations of the water surface were relatively small thanks to analysis using BAUMER probes. This chapter concluded with the fact that the assembly caused the door to be deformed, which meant that its deflection was greater than expected during experiments.

The second part of this thesis focused on the use of the designed mechanism to experimentally study the collapse of a granular column in water at rest and to compare the results with numerical simulations.

In Chapter 6, the theoretical model of Monsorno *et al*[5] is briefly explained serving as a good foundation for understanding the physical behavior of granular material two-phases flows. It ends with the explanations of the numerical implementation of this theoretical model.

Chapter 7 summarized the key parameters influencing the collapse of a column, providing crucial insights for future parametric analyses and serving as a valuable resource for novice students seeking a quick understanding of the most influential parameters in granular column collapse.

Chapter 8 describes our entire experimental setup, including the mechanism designed in the first part of the thesis. Particle size analyses were conducted on different types of sand. An approximation of the initial volume fraction was performed, highlighting the difficulty of accurately estimating this value in experiments. A detailed description of the image processing methods used is provided, including the use of PYTHON method for sand-water interface analysis and the DAVIS 8 software for velocity fields characterization. Furthermore, we outlined the limitations of the setup to guide future improvements by subsequent researchers.

Chapter 9 presented the experimental results. Parametric studies revealed that varying the aspect ratio above unity led to triangular-shaped final deposits, while below unity, the shape is trapezoidal. Additionally, we observed that the ratio of final height to initial height and the angle of repose decreased as the aspect ratio increased, while the runout distance significantly increased.
By varying the initial volume fraction, we discovered that the column was denser

than initially expected. Increasing the volume fraction showed longer collapse times and greater final heights. Regarding grain size, we found that while it did not greatly affect the final shape of the deposits, it significantly impacted their collapsing features. Analyzing the presence or absence of a sand bed revealed that sand grains tend to roll and travel further on smooth ground where a sand bed is absent. Velocity field analysis highlighted erosion in high-aspect-ratio columns and the presence of air bubbles during column collapse, which could potentially influence the results of the comparison by the presence of a second fluid in the collapse.

In the final chapter, comparisons between the experiments conducted in this thesis and the numerical simulations based on the model proposed by Monsorno *et al*[5] were carried out. The comparisons between the final deposits shapes indicated good agreements between the two approaches. However, it is important to note that there were notable differences in the characteristics of the collapse over time between the experiments and the numerical simulations. Specifically, the numerical simulations demonstrated a slower progression towards the runout distance, while in the experiments, the column reached its runout distance at a relatively faster rate.

The aforementioned comparison between experiments and simulations has revealed both agreements and deviations. This highlights the fact that although significant progresses have been made in understanding granular flows, there is still much to explore in order to achieve a comprehensive understanding. Interestingly, when comparing our results with previous experiments, we observed different outcomes for columns with the same aspect ratio, with the only differing factor being the scale used in the experiments. This suggests the need for further investigations into the influence of scale on granular flows. We also noticed some sand grains in suspension in the water during the collapse, it would be interesting to experimentally measure the amount of suspended sand in time. Additionally, it would be valuable to explore the experimental study of 3D water-sand mixture flows, as there is limited literature available on this particular configuration. Finally, we conclude as the Groupement De Recherche Milieux Divisés already did in its granular flows review, 20 years ago[39]:

"We are far from the end of the story"

Bibliography

[1] C. S. Campbell, “Rapid granular flows,” *Annual Review of Fluid Mechanics*, vol. 22, no. 1, pp. 57–90, 1990.

[2] Wikipedia contributors, *Granular material — Wikipedia, the free encyclopedia*, [Online; accessed 1-June-2023], 2023.

[3] O. P. Bruno Andreotti Yoël Forterre, *Les milieux granulaires, Entre fluide et solide*. 2011, p. 512.

[4] F. Courboulex, E. Mercerat, A. Deschamps, *et al.*, “Strong site effect revealed by a new broadband seismometer on the continental shelf offshore nice airport (southeastern france),” *Pure and Applied Geophysics*, vol. 177, Jul. 2020.

[5] D. Monsorno, A. A. Dimas, and M. V. Papalexandris, “Time-accurate calculation of two-phase granular flows exhibiting compaction, dilatancy and nonlinear rheology,” *Journal of Computational Physics*, vol. 372, pp. 799–822, 2018, ISSN: 0021-9991.

[6] F. Nennen, “Experimental and numerical analysis of the collapse of a granular column in water at rest,” Université Catholique de Louvain, 2021.

[7] S. Paul, “Rhéologie des écoulements granulaires: variables internes et effets d’échelle,” Theses, Université de Montpellier, Dec. 2017.

[8] M. Talebpour, “Numerical investigation of turbulent-driven secondary flow,” Ph.D. dissertation, Aug. 2016.

[9] C. Coulomb, “Essai sur un application de règles de maximis et minimis à quelques problèmes de staique relatifs à l’architecture,” *Mém. Math. Phys. Acad. R. Sci., Paris 7*, pp. 343–382, 1773.

[10] G. H. L. Hagen, *Bericht über die zur Bekanntmachung geeigneten Verhandlungen der Konigl.Preuss.Akademie der Wissenschaften zu Berlin.* 1852, pp. 35–42.

[11] O. Reynolds, "Lvii. on the dilatancy of media composed of rigid particles in contact. with experimental illustrations.," *The London, Edinburgh, and Dublin Philosophical Magazine and Journal of Science,*, vol. 20, pp. 469–481, 117 Dec. 1885.

[12] ——, "Experiments showing dilatancy, a property of granular material, possibly connected with gravitation," *Royal Institution of Great Britain*, Feb. 1886.

[13] A. Einstein, "Eine neue bestimmung der moleküldimensionen," *Annalen der Physik*, vol. 324, no. 2, pp. 289–306, 1906.

[14] ——, "Berichtigung zu meiner arbeit: „eine neue bestimmung der moleküldimensionen"`[U+FE01]`," *Annalen der Physik*, vol. 339, no. 3, pp. 591–592, 1911.

[15] É. Guazzelli and O. Pouliquen, "Rheology of dense granular suspensions," *Journal of Fluid Mechanics*, vol. 852, P1, 2018. DOI: `10.1017/jfm.2018.548`.

[16] P. H. R.L. Brown, "Packing of regular (spherical) and irregular particles," *Nature*, vol. 156, no. 3962, pp. 421–422, 1945.

[17] ——, "Effect of container walls on packing density of particles," *Nature*, vol. 157, no. 3992, p. 585, 1946.

[18] K. Terzaghi and G. S. of America, *Mechanism of Landslides.* Harvard University, Department of Engineering, 1950.

[19] R. Bagnold, "The physics of blown sand and desert dunes," *London: Methuen,*, p. 265, 1941.

[20] ——, "Experiments on a gravity-free dispersion of large solid spheres in a newtonian fluid under shear," *Proc. R. Soc. Lond. A*, vol. 225, no. 1160, pp. 49–63, 1954.

[21] e. a. Savage, "Granular flows down rough inclines - review and extension," Studies in Applied Mechanics, vol. 7, pp. 261–282, 1983.

[22] T. G. Drake, "Granular flow: Physical experiments and their implications for microstructural theories," *Journal of Fluid Mechanics*, vol. 225, pp. 121–152, 1991.

[23] H. K. Savage S.B., "The dynamics of avalanches of granular materials from initiation to runout. part i: Analysis.," *Acta Mechanica*, pp. 201–223, 86 1991.

[24] S. Ogawa, "Multitemperature theory of granular materials," *Proc. US-lpn. Semin. Contin.-Mech. and Stat. Approaches Meeh. Granular Mater.*, pp. 208–217, 1978.

[25] X. Chen, J. Wang, and J. Li, “Multiscale modeling of rapid granular flow with a hybrid discrete-continuum method,” *Powder Technology*, vol. 304, pp. 177–185, 2016, SI:Particle2015, ISSN: 0032-5910.

[26] P. A. Cundall, “A computer model for simulating progressive, large-scale movements in blocky rock systems,” 1971.

[27] P. A. Cundall and O. D. L. Strack, “A discrete numerical model for granular assemblies,” *Géotechnique*, vol. 29, no. 1, pp. 47–65, 1979.

[28] S. Thallak, “Discrete element modelling of cyclic behaviour of granular materials,” *Geotechnical and Geological Engineering*, vol. 21, pp. 297–329, Jan. 2003. DOI: `10.1023/B:GEGE.0000006036.00597.0b`.

[29] A. Soroush and B. Ferdowsi, “Three dimensional discrete element modeling of granular media under cyclic constant volume loading: A micromechanical perspective,” *Powder Technology*, vol. 212, no. 1, pp. 1–16, 2011, ISSN: 0032-5910.

[30] H. Zhu, Z. Zhou, R. Yang, and A. Yu, “Discrete particle simulation of particulate systems: A review of major applications and findings,” English, *Chemical Engineering Science*, vol. 63, no. 23, pp. 5728–5770, 2008, ISSN: 0009-2509.

[31] P. Mutabaruka, “Modélisation numérique des milieux granulaires immergés : Initiation et propagation des avalanches dans un fluide,” 2013.

[32] L. Lacaze, J. Bouteloup, B. Fry, and E. Izard, “Immersed granular collapse: From viscous to free-fall unsteady granular flows,” *Journal of Fluid Mechanics*, vol. 912, A15, 2021. DOI: `10.1017/jfm.2020.1088`.

[33] P. Jop, Y. Forterre, and O. Pouliquen, “A constitutive law for dense granular flows,” *Nature*, vol. 441, pp. 727–30, Jul. 2006. DOI: `10.1038/nature04801`.

[34] Y. Jiang and M. Liu, “Granular solid hydrodynamics,” *Granular Matter*, vol. 11, pp. 139–156, 2008.

[35] D. Henann and K. Kamrin, “A predictive, size-dependent continuum model for dense granular flows,” *Proceedings of the National Academy of Sciences of the United States of America*, vol. 110, Mar. 2013. DOI: `10.1073/pnas.1219153110`.

[36] J. D. Goddard, “Continuum Modeling of Granular Media,” *Applied Mechanics Reviews*, vol. 66, no. 5, May 2014, 050801, ISSN: 0003-6900.

[37] M. Constant, F. Dubois, J. Lambrechts, and V. Legat, “Implementation of an unresolved stabilised fem–dem model to solve immersed granular flows,” *Computational Particle Mechanics*, vol. 6, Sep. 2018. DOI: `10.1007/s40571-018-0209-4`.

[38] "Numerical study of the collapse of columns of sand immersed in water using two-phase flow modelling," *International Journal of Multiphase Flow*, vol. 153, p. 104 143, 2022, ISSN: 0301-9322.

[39] G. D. R. Midi, "On dense granular flows," *The European Physical Journal E*, vol. 14, pp. 341–365, 2003.

[40] G. Lube, H. E. Huppert, R. S. J. Sparks, and A. Freundt, "Collapses of two-dimensional granular columns," *Phys. Rev. E*, vol. 72, p. 041 301, 4 Oct. 2005.

[41] E. L. THOMPSON and H. E. HUPPERT, "Granular column collapses: Further experimental results," *Journal of Fluid Mechanics*, vol. 575, pp. 177–186, 2007. DOI: `10.1017/S0022112006004563`.

[42] L. Lacaze, J. Phillips, and R. Kerswell, "Planar collapse of a granular column: Experiments and discrete element simulations," English, *Physics of Fluids*, vol. 20, no. 6, p. 063 302, 2008, Other identifier: 063302, ISSN: 1070-6631. DOI: `10.1063/1.2929375`.

[43] L. Rondon, O. Pouliquen, and P. Aussillous, "Granular collapse in a fluid: Role of the initial volume fraction," *Physics of Fluids - PHYS FLUIDS*, vol. 23, Jul. 2011.

[44] C.-H. Lee, Z. Huang, and M.-L. Yu, "Collapse of submerged granular columns in loose packing: Experiment and two-phase flow simulation," *Physics of Fluids*, vol. 30, p. 123 307, Dec. 2018.

[45] Y. Grasselli and H. Herrmann, "On the angles of dry granular heaps," *Physica A: Statistical Mechanics and its Applications*, vol. 246, no. 3, pp. 301–312, 1997, ISSN: 0378-4371.

[46] D. Bonamy, F. Daviaud, L. Laurent, M. Bonetti, and J. P. Bouchaud, "Multiscale clustering in granular surface flows," *Phys. Rev. Lett.*, vol. 89, p. 034 301, 3 Jun. 2002.

[47] S. Courrech du Pont, P. Gondret, B. Perrin, and M. Rabaud, "Granular avalanches in fluids," *Phys. Rev. Lett.*, vol. 90, p. 044 301, 4 Jan. 2003. DOI: `10.1103/PhysRevLett.90.044301`. [Online]. Available: `https://link.aps.org/doi/10.1103/PhysRevLett.90.044301`.

[48] E. Azanza, "Ecoulements granulaires bidimensionnels sur un plan incliné," 1998.

[49] G. Berton, R. Delannay, P. Richard, N. Taberlet, and A. Valance, "Two-dimensional inclined chute flows: Transverse motion and segregation," *Phys. Rev. E*, vol. 68, p. 051 303, 5 Nov. 2003.

[50] O. Pouliquen, "Scaling laws in granular flows down rough inclined planes," *Physics of Fluids*, vol. 11, no. 3, pp. 542–548, Mar. 1999.

[51] A. Daerr and S. Douady, "Two types of avalanche behaviour in granular media," *Nature*, vol. 399, pp. 241–243, 1999.

[52] O. Pouliquen and R. Gutfraind, "Stress fluctuations and shear zones in quasistatic granular chute flows," *Phys. Rev. E*, vol. 53, pp. 552–561, 1 Jan. 1996.

[53] F. Chevoir, M. Prochnow, P. Moucheront, *et al.*, "Dense granular flows in a vertical chute," *Powders and Grains 2001*, 2020.

[54] F. Chevoir, M. Prochnow, P. Moucheront, *et al.*, "Dense granular flows in a vertical chute," *Powders and Grains*, Jan. 2001.

[55] G. Lauber and W. H. Hager, "Experiments to dambreak wave: Horizontal channel," *Journal of Hydraulic Research*, vol. 36, no. 3, pp. 291–307, 1998.

[56] M. Aurisicchio, R. Bracewell, and G. Armstrong, "The function analysis diagram: Intended benefits and coexistence with other functional models," *Artificial Intelligence for Engineering Design, Analysis and Manufacturing*, vol. 27, Aug. 2013.

[57] I. Michalakoudis, P. Childs, M. Aurisicchio, and J. Harding, "Using functional analysis diagrams to improve product reliability and cost," *Advances in Mechanical Engineering*, vol. 9, no. 1, p. 1 687 814 016 685 223, 2017.

[58] *Fundamentals of Machine Component Design.* John Wiley & Sons Incorporated, 2021, ISBN: 9781119834854.

[59] A. Palmgren, B. Ruley, G. Palmgren, and i. SKF Industries, *Ball and Roller Bearing Engineering.* SKF Industries, 1945.

[60] J. Vidosic, *Machine Design Projects.* Ronald Press Company, 1957.

[61] Geotechdata.info. "Soil void ratio." (2013).

[62] M. Uesugi and H. Kishida, "Frictional resistance at yield between dry sand and mild steel," *Soils and Foundations*, vol. 26, no. 4, pp. 139–149, 1986, ISSN: 0038-0806.

[63] D. Monsorno, C. Varsakelis, and M. Papalexandris, "Poiseuille flow of dense non-colloidal suspensions: The role of intergranular and nonlocal stresses in particle migration," *Journal of Non-Newtonian Fluid Mechanics*, vol. 247, pp. 229–238, 2017, ISSN: 0377-0257.

[64] D. Monsorno, A. A. Dimas, and M. V. Papalexandris, "Time-accurate calculation of two-phase granular flows exhibiting compaction, dilatancy and nonlinear rheology," *J. Comput. Phys.*, vol. 372, no. C, pp. 799–822, Nov. 2018, ISSN: 0021-9991.

[65] S. Benyahia, M. Syamlal, and T. J. O'Brien, "Extension of hill–koch–ladd drag correlation over all ranges of reynolds number and solids volume fraction," *Powder Technology*, vol. 162, no. 2, pp. 166–174, 2006, ISSN: 0032-5910.

[66] M. Papalexandris, "A two-phase model for compressible granular flows based on the theory of irreversible processes," *Journal of Fluid Mechanics*, vol. 517, pp. 103–112, Oct. 2004.

[67] M. A. Goodman and S. C. Cowin, "A continuum theory for granular materials," *Archive for Rational Mechanics and Analysis*, vol. 44, pp. 249–266, 1972.

[68] C. Varsakelis and M. V. Papalexandris, "Low-mach-number asymptotics for two-phase flows of granular materials," *Journal of Fluid Mechanics*, vol. 669, pp. 472–497, 2011.

[69] D. Monsorno, C. Varsakelis, and M. V. Papalexandris, "A two-phase thermomechanical theory for granular suspensions," *Journal of Fluid Mechanics*, vol. 808, pp. 410–440, 2016. DOI: `10.1017/jfm.2016.649`.

[70] J. M. Powers, D. S. Stewart, and H. Krier, "Analysis of Steady Compaction Waves in Porous Materials," *Journal of Applied Mechanics*, vol. 56, no. 1, pp. 15–24, Mar. 1989, ISSN: 0021-8936.

[71] A. J. Chorin, "A numerical method for solving incompressible viscous flow problems," *Journal of Computational Physics*, vol. 2, no. 1, pp. 12–26, 1967, ISSN: 0021-9991.

[72] M. Cabrera and N. Estrada, "Granular column collapse: Analysis of grain-size effects," *Phys. Rev. E*, vol. 99, p. 012 905, 1 Jan. 2019.

[73] A. Bougouin, L. Lacaze, and T. Bonometti, "Collapse of a liquid-saturated granular column on a horizontal plane," *Phys. Rev. Fluids*, vol. 4, p. 124 306, 12 Dec. 2019.

[74] C. JIAN, *Discrete element method for 3d simulations of mechanical systems of non-spherical granular materials.*

[75] A. Bougouin and L. Lacaze, "Granular collapse in a fluid: Different flow regimes for an initially dense-packing," *Phys. Rev. Fluids*, vol. 3, p. 064 305, 6 Jun. 2018. DOI: `10.1103/PhysRevFluids.3.064305`. [Online]. Available: `https://link.aps.org/doi/10.1103/PhysRevFluids.3.064305`.

[76] V. Topin, Y. Monerie, F. Perales, and F. Radjaı¨, "Collapse dynamics and runout of dense granular materials in a fluid," *Phys. Rev. Lett.*, vol. 109, p. 188 001, 18 Nov. 2012. DOI: `10.1103/PhysRevLett.109.188001`. [Online]. Available: `https://link.aps.org/doi/10.1103/PhysRevLett.109.188001`.

[77] A. Valerga, R. Jimenez-Rodriguez, S. Fernandez-Vidal, and S. R. Fernandez Vidal, "Photogrammetry as an engineering design tool," in Jun. 2020, ISBN: 978-1-83968-212-4.

[78] L. GmbH. "Fluid mechanics flowmaster." ().

[79] A. Boomsma, S. Bhattacharya, D. Troolin, S. Pothos, and P. Vlachos, "A comparative experimental evaluation of uncertainty estimation methods for two-component piv," *Measurement Science and Technology*, vol. 27, p. 094 006, Sep. 2016. DOI: `10.1088/0957-0233/27/9/094006`.

[80] C. NV, *Déclaration des performances, produit : Sable de rivière 0/2*, Accessed: 18-05-2023.

[81] B. Spinewine, "Two-layer flow behaviour and the effects of granular dilatancy in dam-break induced sheet-flow," Ph.D. dissertation, Dec. 2005.

[82] L. Lacaze, J. Phillips, and R. Kerswell, "Planar collapse of a granular column: Experiments and discrete element simulations," English, *Physics of Fluids*, vol. 20, no. 6, p. 063 302, 2008, Other identifier: 063302, ISSN: 1070-6631.

[83] Z. Chik and L. E. Vallejo, "Characterization of the angle of repose of binary granular materials," *Canadian Geotechnical Journal*, vol. 42, pp. 683–692, 2005.

[84] "A review on the angle of repose of granular materials," *Powder Technology*, vol. 330, pp. 397–417, 2018.

[85] C. Varsakelis and M. Papalexandris, "On the relevance of low-mach-number asymptotics in thermodynamics of heterogeneous, immiscible mixtures," *Journal of Non-Equilibrium Thermodynamics*, vol. 42, Jan. 2016.

[86] S. S. Frazão, "Hydraulique fluviale - rivières et sédiments," Université Catholique de Louvain, 2022.

[87] T. Weinhart, R. Hartkamp, A. R. Thornton, and S. Luding, "Coarse-grained local and objective continuum description of three-dimensional granular flows down an inclined surface," *Physics of Fluids*, vol. 25, no. 7, Jul. 2013.

Appendices

A

Specifications

This page is intentionally left blank.

		Specifications
Context		**Water channel opening door system** The aim of this project is to design and manufacture a system that simulate a dam break at smaller scale in a water channel. To do so, it is asked to conceive a door that opens almost instantly. The door should solve the previous system issues.
Date	**Authors**	**Main functions**
09-2022	V.Anciaux B.Schoeps	**MF1:** Open and close a door on the channel. **MF2:** Ensure sealing at the door. **MF3:** Move the door system along the axis of the channel.

		Main constraints
		1. Opening speed 2. Channel dimensions 3. Pressure resistance 4. Water resistance 5. Sandy environment 6. Budget 7. Multi-purpose
Date	**Authors**	**Constraints requirements**
09-2022	V.Anciaux B.Schoeps	**CR 1 - Opening speed**: The opening speed should respect the condition of instantaneousness. The computation of the criterion is detailed in section 5.2
09-2022	V.Anciaux B.Schoeps	**CR 2 - Channel dimensions**: - Height : $H = 0,4[m]$. - Width : $W = 0,5[m]$.
09-2022	V.Anciaux B.Schoeps	**CR 3 - Pressure resistance**: Maximal pressure (with water and sand on one side and air on the other side) : **8200 Pa**
09-2022	V.Anciaux B.Schoeps	**CR 4 - Water resistant**: It should avoid rusting.
09-2022	V.Anciaux B.Schoeps	**CR 5 - Sandy environment**: A lot of grain with different sizes and shapes will be present in the working environment. The system should keep on working correctly in this environment (Avoid the jamming of the system by the sand grains, avoid abrasion...)
09-2022	V.Anciaux B.Schoeps	**CR 6 - Budget**: The total cost of the project should not exceed 3000€ TVAC
09-2022	V.Anciaux B.Schoeps	**CR 6 - Multi-purpose**: The system should be usable for other works, like the simulation of a dam break.

B

User manual - English version

B.1 Glossary

- Railway cart
- Sliding door
- Cable
- Counterweight structure
- Stabilizing plate
- Drop-down plate
- Channel

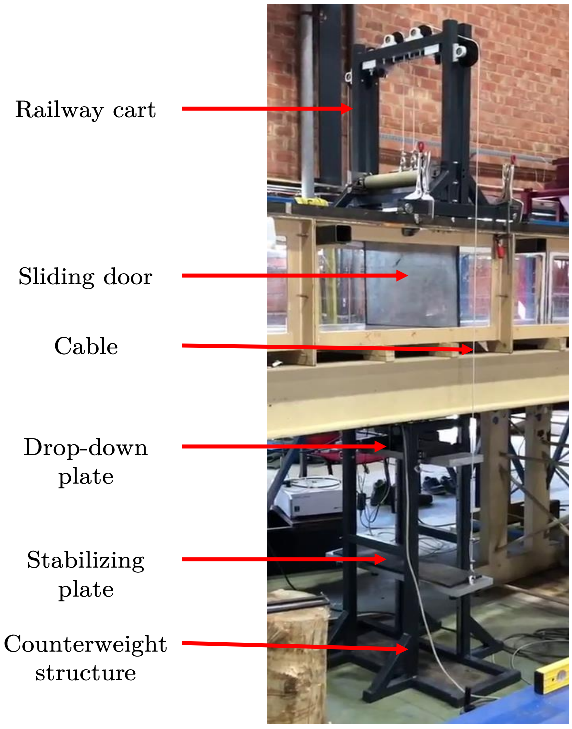

B.2 Risks and measures to take

The installation, use and removal of the mechanism can lead to a number of significant risks (the weight of the mechanism, the free-fall mass and the electromagnet's electronics). Measures must be taken to ensure the safety of the user:

- It is essential to always wear safety shoes when installing, using and uninstalling the mechanism.
- During use, make sure that the counterweight is isolated by traffic cones or safety barriers to prevent people from passing through while the weights are falling.
- Ask a qualified person to operate the bridge crane. Any laboratory technician is can do this.
- Electrical connections must always be fixed high up.

B.3 Installation

1. Check that the gasket[1] adheres perfectly to the sliding door. If not, change the gasket or re-glue it to the plate with LOCTITE 401.
2. The edges of the glass panes on the channel are quite sharp and cause severe damage to the gaskets. File them with a metal blade where you want to place the sliding door.
3. Put the sliding door in the channel. Be sure to be perpendicular to the channel walls.
4. Make sure that the adjustable rollers are loose (= they are in distant position). Use the overhead crane to lift the railway cart. *Warning : Ask an operator if you are not qualified to use it.*
   Using the overhead crane, align the railway cart with the door and slowly go down making sure that the door goes in between all the rollers of the cart. When the cart is reaching the rail, make sure that all four wheels are on the rail and that the rail comes between the bearings with a vertical axis.
5. Put the cart in position and lock it in place using at least 4 clamps. Clamp it vertically and horizontally.
6. Insert the skids of the drop-down plate into the sliders of the counterweight structure, put it all up. Lock it up using the safety bars.
7. Put the counterweight structure under the channel, at the exact same position of the railway cart. The larger part parallel to the door.
8. Put the rubber sheet inside the base of the structure of the counterweight.
9. Put the stabilizing plate on the rubber sheet.
10. Attach the cables to the door and pull it up until it is 40 cm over the bottom of the channel. Block the door using a piece of wood.
11. Attach the cable to the stabilizing plate that it is still supposed to be lying on the rubber sheet (= the lowest position possible).
12. Make sure that the cables are stretched in exactly the same way. To do so, unblock the door and put it down into the channel, then, use a level on the stabilizing plate and make sure it is perfectly horizontal.
13. Tighten the rollers until they are tangent to the sliding door.

---

[1] ERIKS Profilé rainuré TPeRX 60 noir 3338 L=30 m

B.4 Usage

The purpose of this mechanism is to raise almost instantly a door by means of a counterweight system. The speed at which the door is raised depends on several parameters, particularly the weights installed on the counterweight and the hydrostatic forces exerted on the door.

Critical Security Warnings :

- The system is not aim to undergo waves. It can undergo a maximum water flow rate of 5 l/s.
- The counterweight system uses an electro-magnet that works with a voltage of 240 V. ac. Knowing that the working environment is likely to have water, make sure to isolate any electrical parts from the places that could get wet (switchs, electrical sockets and plugs...).
- The counterweight system is made of elements that have falling masses in a range of 10 to 50 kg depending on the loading. These elements are located under the channel and fall from a height of 110 cm.
- While operating, make sure that the counterweight is isolated with cones or security barriers to avoid people walking by when masses are falling.

1. Check that the door is correctly installed on the channel by referring to the Appendix B.3. At this moment, the drop-down plate is at its lowest position and so the sliding door is up.
2. Check that the clamps are correctly tightened. If not, retighten them.
3. Place the safety cones or barriers around the counterweight structure. It has to stay there all along the experiment.
4. If they are there, remove the two horizontal safety bars that are placed on the side walls of the counterweight structure.
5. Place the handle bar on the drop-down plate.
6. Activate the electromagnet by plugging in the socket connected to it. When the power is on, the electromagnet is activated. Make sure that the switch of the socket or its connection is more than 2 meters away from the channel.

7. Gently lift the drop-down plate by its handle to halfway up. Remove the bar from the handle while supporting the plate underneath and continue to raise it up to the electromagnet.
8. Once the plate is attached to the electromagnet, replace the horizontal safety bars that are placed on the side walls of the counterweight structure. From this time, make sure to never let anything go under the drop-down plate. Any electrical dysfunctionment could lead instantly to the unwanted release of the weight.
9. Add the necessary weight corresponding to the door lift according to your application. Usually, putting 15kg is large enough. Be careful to distribute the weight evenly over the drop-down plate.
10. Strap the weights down to prevent them from shifting during the free fall.
11. Clean the gaskets from any residual grains of sand.
12. Humidify the gaskets with some water.
13. Lower the sliding door to the bottom of the channel.
14. Wait until the stabilizing plate is properly stabilized and no longer vacillates.
15. Remove the horizontal safety bars that are placed on the side walls of the counterweight structure. Warning : the weight is now able to drop.
16. When you are ready, disconnect the electromagnet by disconnecting the power or closing the switch. The drop-down plate will instantly fall on the stabilizing plate leading to the raise of the sliding door.

B.5 Uninstallation and storage

1. Put the drop-down plate up and lock it up using the safety bars.
2. Put the stabilizing plate down and remove the cables from it. Take out the stabilizing plate and the rubber sheet and store them.
3. Lower the door into the channel and remove the cables. Store them.
4. Now that the stabilizing plate is out, remove the safety bars and lower the drop-down plate. Take it out of the sliders by tilting the counterweight structure. Store the drop-down plate.

5. Store the counterweight structure. Make sure to store the 2 safety bars and the drop-down plate handle bar with the structure to prevent from losing them.
6. Loosen the rollers. Use the overhead crane to lift the railway cart gently. (Warning : Ask an operator if you are not qualified to use it).
7. Put the railway cart down on the ground and store it.
8. Take the door out of the channel and store it.

C
Manuel d'utilisation - Version française

C.1 Lexique

- Chariot
- Porte coulissante
- Cable
- Structure du contrepoids
- Plaque stabilisante
- Plaque tombante
- Canal

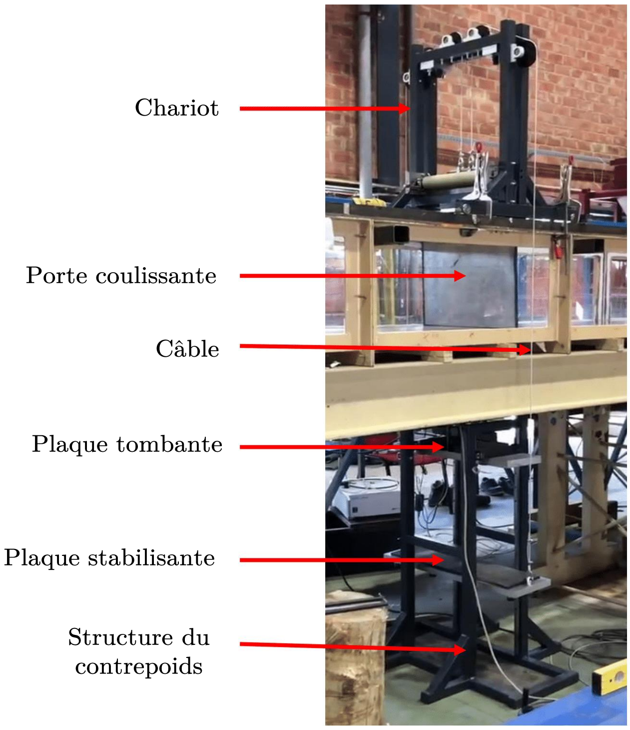

C.2 Risques et mesures à prendre

L'installation, l'utilisation et la déinstallation du mécanisme peuvent entraîner un certain nombre de risques importants (le poids du mécanisme, la masse en chute libre et l'électronique de l'électro-aimant). Des mesures doivent être prises pour assurer la sécurité de l'utilisateur et des personnes aux alentours:

- Il est indispensable de toujours porter des chaussures de sécurité lors de l'installation, de l'utilisation et de la désinstallation du mécanisme.
- Pendant l'utilisation, s'assurer que le contrepoids est isolé par des cônes de signalisation ou des barrières de sécurité afin d'empêcher le passage de personnes à proximité du mécanisme pendant la chute des poids.
- Demander à une personne qualifiée de faire fonctionner le pont roulant. Tout technicien de laboratoire est habilité à le faire.
- Les connexions électriques doivent toujours être fixées en hauteur.

C.3 Installation

1. Vérifiez que le joint[1] est correctement collé à la porte coulissante. Si non, changez le joint ou re-collez le à la porte avec la colle LOCTITE 401.
2. Les arêtes des vitres du canal sont assez coupantes et peuvent endommager le joint. Limez-les à l'endroit où vous voulez placer la porte coulissante pour en adoucir l'angle.
3. Mettez la porte coulissante dans le canal. Assurez-vous qu'elle soit bien perpendiculaire aux murs du canal.
4. Assurez-vous que les rouleaux soient desserrés (= ils sont éloignés l'un de l'autre). Utilisez le pont roulant pour soulever le chariot *Attention : Demandez à un technicien de le faire si vous n'avez pas la license pour l'utiliser.* En utilisant le pont roulant, alignez le chariot avec la porte coulissante et descendez-le sur les rail. Assurez-vous que les quatres roues soient bien sur les rails et que le rail de droite (lorsqu'on regarde dans le sens de l'écoulement) passe bien entre les roulements verticaux qui servent de guidage
5. Mettez le chariot à la position désirée et bloquez le en utilisant au moins quatre serre-joints. Clamez le verticalement et horizontalement.
6. Insérez les patins de la plaque tombante dans les glissières de la structure du contrepoids et montez-la jusque tout en haut. Bloquez-la en utilisant les barres de sécurité.
7. Mettez la structure du contrepoids sous le canal, exactement à la même position que le chariot. La partie la plus large doit être parallèle à la porte coulissante.
8. Mettez la feuille de caoutchouc à l'intérieur de la base de la structure du contrepoids.
9. Mettez la plaque stabilisante sur la feuille de caoutchouc.
10. Attachez les cables à la porte et soulevez-la de 40 cm du fond du canal. Bloquez la porte en utilisant un morceau de bois.
11. Attachez le cable à la plaque stabilisante qui est doit toujours reposer sur la feuille de caoutchouc (= la position la plus basse possible).

---

[1] ERIKS Profilé rainuré TPeRX 60 noir 3338 L=30 m

12. Serrez les rouleaux jusqu'à ce qu'ils soient tangents à la porte coulissante.
13. Assurez-vous que les deux cables soient tendu exactement de la même manière. Pour ce faire, débloquez la porte et descendez la au fond du canal, puis, utilisez un niveau pour vérifiez que la plaque stabilisante est parfaitement horizontale.

C.4 Utilisation

Le but de ce mécanisme est de soulever quasi instantanément une porte en utilisant un système de contrepoids. La vitesse de levage de la porte dépend de plusieurs paramètres, notamment, les poids installés sur le contrepoids et les forces hydrostatiques exercées sur la porte.

Avertissements de sécurité importants :

- Le système n'est pas prévu pour résister à des vagues. Il peut supporter un débit d'eau de maximum 5 L/s
- Le système de contrepoids utilise un électro-aimant qui fonctionne avec une tension de 240 V AC. Sachant que l'environnement de travail est propice aux éclaboussures, assurez-vous d'isoler les élements électriques des endroits qui pourraient être mouillés (interrupteurs, multiprises, fiches ...)
- Le système de contrepoids est fait d'élements tombants. Ces élements ont une masse comprise entre 10 et 50 kg en fonction du chargement. Ils sont situés sous le canal et chutent d'une hauteur de 110 cm.
- Durant l'utilisation, assurez-vous que le contrepoids est isolé avec des cônes de signalisation ou des barrières de sécurité pour éviter que des gens ne passent à proximité quand les masses tombent.

1. Vérifiez que la porte est correctement installée sur le canal en vous réferrant à l'Appendice C.3. A partir d'ici nous considérons que la plaque tombante est en position basse et que la porte coulissante est levée.
2. Vérifiez que les serre-joints sont correctement serrés. Si non, resserrez les.
3. Placez les cônes de signalisation ou les barrières autour de la structure du contrepoids. Ces derniers doivent rester en place durant toute l'utilisation du système.

4. Si elles sont là, enlevez les deux barres de sécurité qui sont placées sur les côtés de la structure du contrepoids.
5. Mettez la barre qui sert de poignée dans les anneaux de la plaque tombante.
6. Allumez l'électro-aimant en branchant ou allumant le multi-prise connecté à ce dernier. Quand le courant passe, l'électro-aimant est actif. Assurez-vous que l'interrupteur du multi-prise est à au moins 2 mètres du canal.
7. Levez doucement la plaque tombante par sa poignée jusqu'à la moitié de sa course. Enlevez la poignée en supportant la plaque par dessous et continuez de monter jusqu'à-ce qu'elle s'accroche à l'électro-aimant.
8. Une fois la plaque aimantée à l'électro-aimant, remettez les barres de sécurité horizontales sur les partie latérales de la structure du contrepoids. A partir de maintenant, assurez-vous de ne rien laisser passer sous la plaque tombante. Tout dysfonctionnement électrique pourraient amener à une chute non-désirée du poids.
9. Ajoutez la masse nécessaire correspondant à votre utilisation. Généralement, mettre une masse de 15 kg est largement suffisant. Faites attention de répartir le poids uniformément sur la plaque tombante
10. Attachez les poids pour éviter qu'ils ne bougent durant la chute.
11. Nettoyez le joint de la porte coulissante pour enlever tous grains de sable résiduels.
12. Humidifiez le joint avec de l'eau pour légèrement le lubrifier.
13. Abaissez la porte coulissante jusqu'au fond du canal.
14. Attendez jusqu'à ce que la plaque stabilisante n'oscille plus.
15. Enlevez les barres de sécurité qui sont sur les cotés de la structure du contrepoids. Attention : Le poids est maintenant libre de tomber.
16. Quand vous êtes prêt, déconnectez l'électro-aimant en coupant le courant. La plaque tombante va chuter instantanement sur la plaque stabilisante, ce qui va entrainer la montée de la porte coulissante.

C.5 Désinstallation et stockage

1. Montez la plaque tombante jusqu'en haut de sa course et bloquez-la avec les barres de sécurité.

2. Mettez la plaque stabilisante au sol et décrochez les cables. Enlevez la plaque stabilisante et la feuille de caoutchouc puis stockez-les.

3. Abaissez la porte dans le canal et décrochez les cables. Stockez-les.

4. Maintenant que la plaque stabilisante est retirée, enlevez les barres de sécurité et abaissez doucement la plaque tombante. Sortez la des glissières en inclinant la structure du contrepoids. Stockez la plaque tombante.

5. Stockez la structure du contrepoids. Veillez à stockez les 2 barres de sécurité et la poignée de la plaque tombante avec la structure pour éviter de les perdre.

6. Désserrez les rouleaux. Utilisez le pont roulant pour soulevez le chariot *Attention : Demandez à un technicien de le faire si vous n'avez pas la license pour l'utiliser*, puis descendez-le sur le sol et stockez-le.

7. Sortez la porte coulissante en dehors du canal et stockez-la.

D

Detailed budget

This page is intentionally left blank.

MISUMI

Name of the component	Utility	Ref. Misumi	Quantity	Unit price(€)	Total price:
Metal roller	Guiding	RORELA38-15-L350	2	40,95 €	81,90 €
Urethane roller	Guiding	RORELAG48-T5-15-L350	2	105,56 €	211,12 €
Rollers' shaft	Carrying the rollers	SFRV15-429-F20-T20-W13	2	36,58 €	73,16 €
Rollers' shaft	Carrying the rollers	PSFG15-429	2	13,53 €	27,06 €
Pulleys' shaft	Porter les poulies	PSFG12-80	4	2,61 €	10,44 €
Bearings	Trolley motion	NTSBGT37-20	4	22,52 €	90,08 €
Bearings	Trolley motion	NTSBGT13-8	4	6,70 €	26,80 €
Pulleys	Lifting mechanism Center	MBRDC80-2.5-12	2	20,73 €	41,46 €
Pulleys	Lifting mechanism Sides	MBRC100-3-12	2	23,41 €	46,82 €
Bearing housings	On the pulley's shafts	C-BGHKA6001ZZ-30	8	12,39 €	99,12 €
Set collars	Locking shafts	PSCSPT15-12	4	9,64 €	38,56 €
Rubber bumper	Door opening dampening	NBBYS20-30-M8	4	10,00 €	40,00 €
Set collars	Locking urethane rollers	SCSBR15-21	4	4,35 €	17,40 €
Set collars	Locking metal rollers	SCSBR15-19	4	4,35 €	17,40 €
Set collars	Locking pulley shafts	SCSBR12-16	8	3,54 €	28,32 €
Guidage	Counterweight guiding	C-SVWT24-1000	4	84,81 €	339,24 €
Belt Tensioner	Roller adjustment	RONAJ15	4	39,58 €	158,32 €
Damper	Counterweight damping	GELSMF30	12	19,36 €	232,32 €
					1.579,52 €

ERIKS

Name of the component	Utility	Ref. Eriks	Quantity	Unit price(€)	Total price:
ERIKS Profilé rainuré	Door sealing	10000347	10 M	5,50 €	55,00 €
					55,00 €

RS-COMPONENT

Name of the component	Utility	Ref. RS-Component	Quantity	Unit price(€)	Total price:
RS PRO ACD Magnet 1000N 240V ac	Magnet counterweight	7393245	1	87,65 €	87,65 €
					87,65 €

Table D.1

Name of the component	Utility	Ref. Lemmens	Quantity	Unit price(€)	Total price:
LEMMENS					
CABLE PVC 03-04MM 7X19	Pulley cable	719DT0304	12m	2,20 €	26,40 €
Manille G210	Link Rings/Cables	MA2100050	2	2,16 €	4,32 €
SERRE-CABLE	Tightening the cable	SCG74103	20	0,30 €	6,00 €
COSSE GALVANISEE	Cable curvature	COCOGB03	3	0,21 €	0,62 €
COSSE GALVANISEE	Cable curvature	COCOGB04	6	0,24 €	1,42 €
ANNEAU DE LEVAGE M08	Rings plate	ANLM08005	2	15,00 €	30,00 €
Frais de port			1	17,50 €	17,50 €
					86,26 €
BRICO					
BRICO	Screws, shackles...			22,09 €	22,09 €
					22,09 €
				PRIX HTVA	**1.830,52** €
				PRIX TVAC	2.214,93 €

Table D.2

E

Design drawings and components features

This page is intentionally left blank.

ECHELLE 1:5

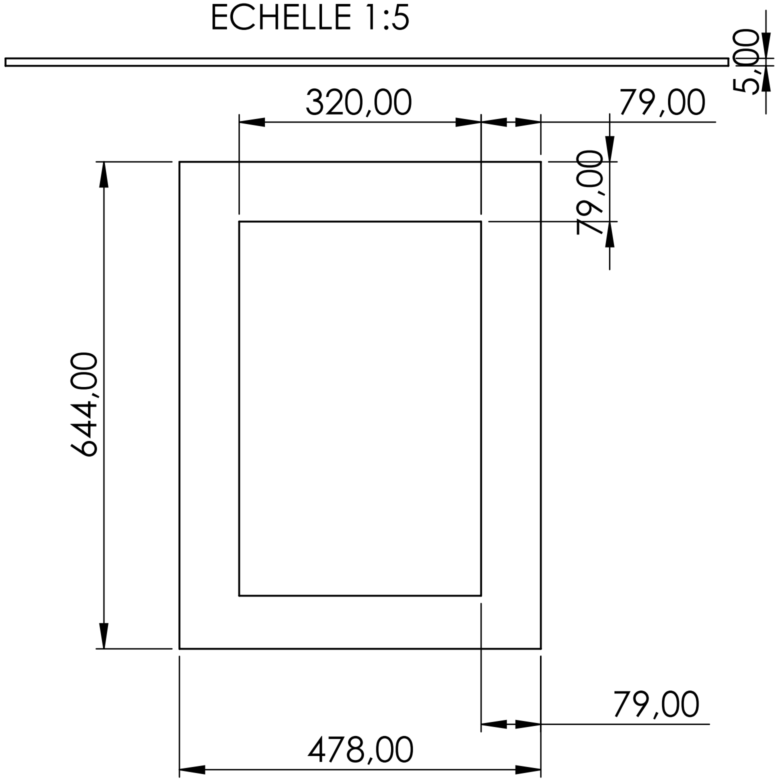

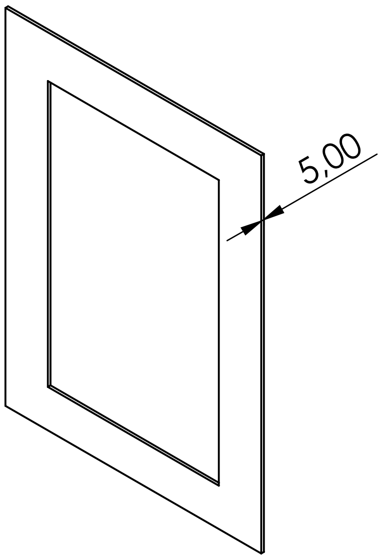

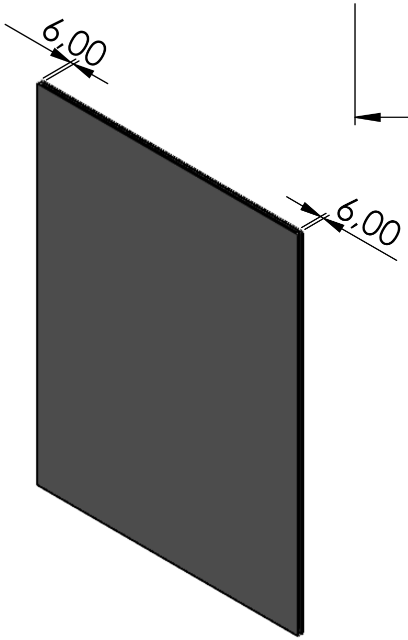

TITRE: Plaque plexi

PROJET :
Canal - Conception d'une porte

iMMC-TFL - Place du Levant, 2
B1348 Louvain-la-Neuve - Belgium
Tel. +32(0)10.47.22.00 -
Fax. +32(0)10.45.26.92
http://www.uclouvain.be/immc

UCLOUVAIN

Designers :
Anciaux Victor
Schoeps Benoît

Date : 16-02-23

Echelle : 1:10

Materials: PLEXIGLASS

A4

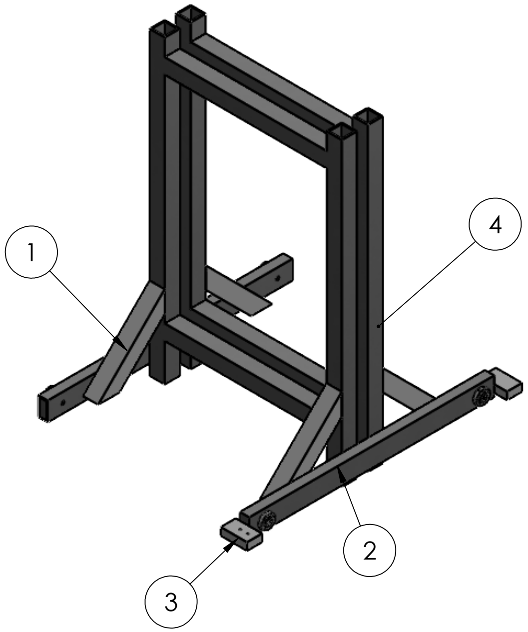

Numéro pièce	Infos	Nombre
1	Voir détail 1	4
2	Pièce manufacturée par Vincent	2
3	Pièce manufacturée par Vincent	2
4	Pièce déjà soudée par Julien	3

PIECE 1

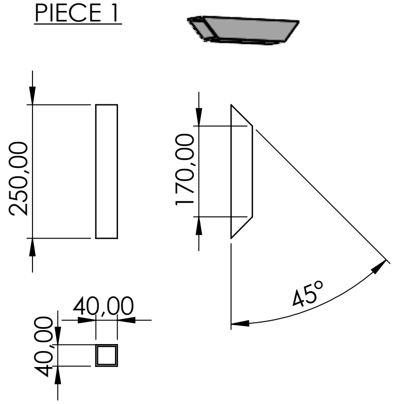

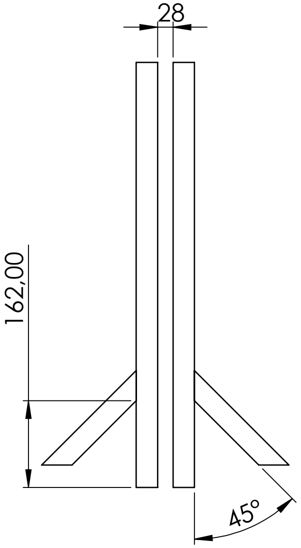

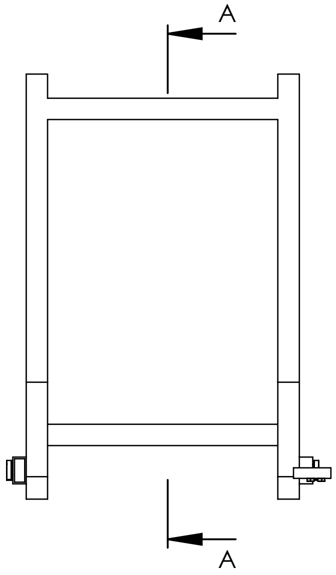

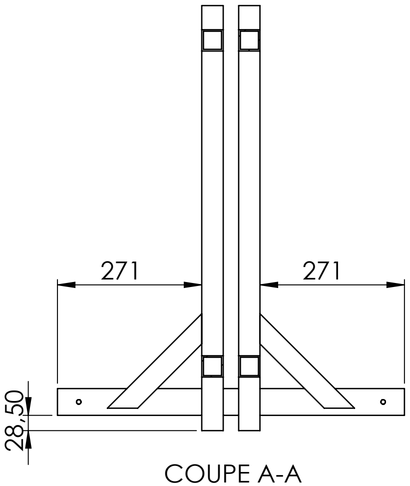

COUPE A-A

SOUDURE PIECE 2/3

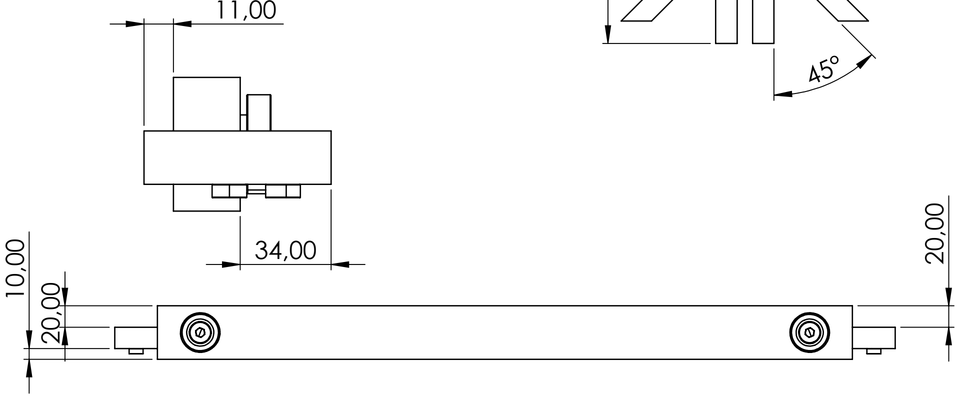

TOUTES LES BARRES EN ACIER SONT
DE DIMENSIONS 40x40x3

TOUTES LES JONCTIONS SONT SOUDEES

TITRE: Structure en "H"

PROJET : Canal - Conception d'une porte

UCLouvain

Designers :
Anciaux Victor
Schoeps Benoît

Date : 01-03-23

Echelle : 1:10

N° : 1

1/1

A3

iMMC-TFL - Place du Levant, 2 - B1348 Louvain-la-Neuve - Belgium
Tel. +32(0)10.47.22.00 - Fax. +32(0)10.45.26.92 - http://www.uclouvain.be/immc

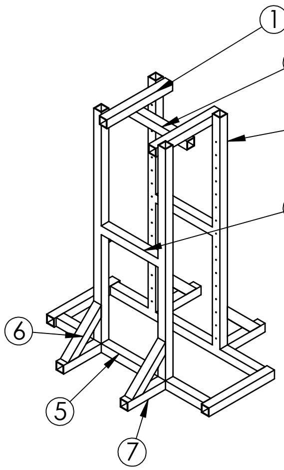

VUE DU HAUT

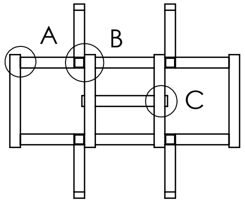

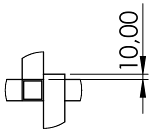

DÉTAIL B
ECHELLE 1 : 10

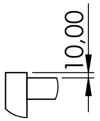

DÉTAIL A
ECHELLE 1 : 10

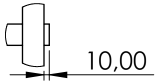

DÉTAIL C
ECHELLE 1 : 10

NUMÉRO DE LA PIÈCE	Longueur [mm]	Nombre
1	348	4
2	320	1
3	1060	4
4	300	2
5	780	2
6	250	4
7	200	4

VUE DE FACE

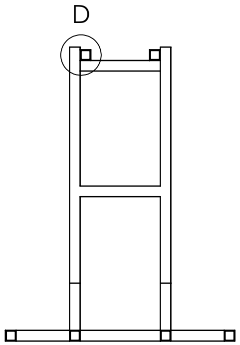

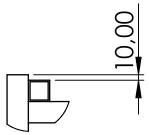

DÉTAIL D
ECHELLE 1 : 10

PIECE 3
DETAIL

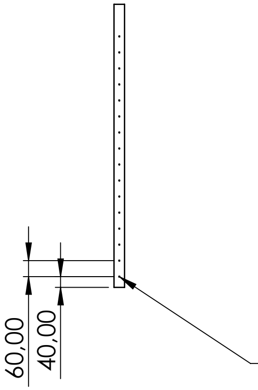

PIECE 6
DETAIL

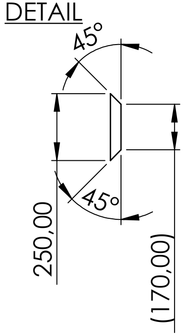

DETAIL SOUDURE

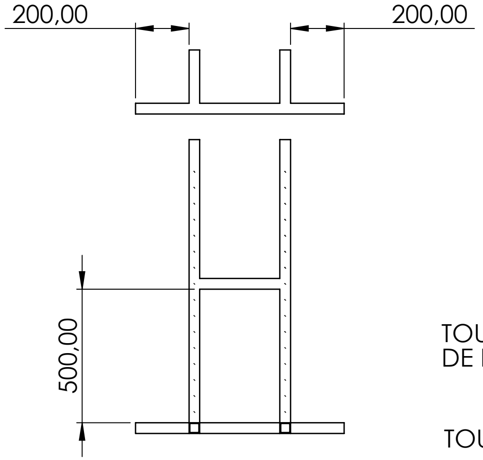

TOUTES LES BARRES EN ACIER SONT
DE DIMENSIONS 40x40x3

TOUTES LES JONCTIONS SONT SOUDEES

UCLouvain

TITRE: STRUCTURE CONTREPOIDS

PROJET : Canal - Conception d'une porte

Designers :
Anciaux Victor
Schoeps Benoît

Date :
01-03-23

Echelle :
1:20

N° :
1

1/1

A3

iMMC-TFL - Place du Levant, 2 - B1348 Louvain-la-Neuve - Belgium
Tel. +32(0)10.47.22.00 - Fax. +32(0)10.45.26.92 - http://www.uclouvain.be/immc

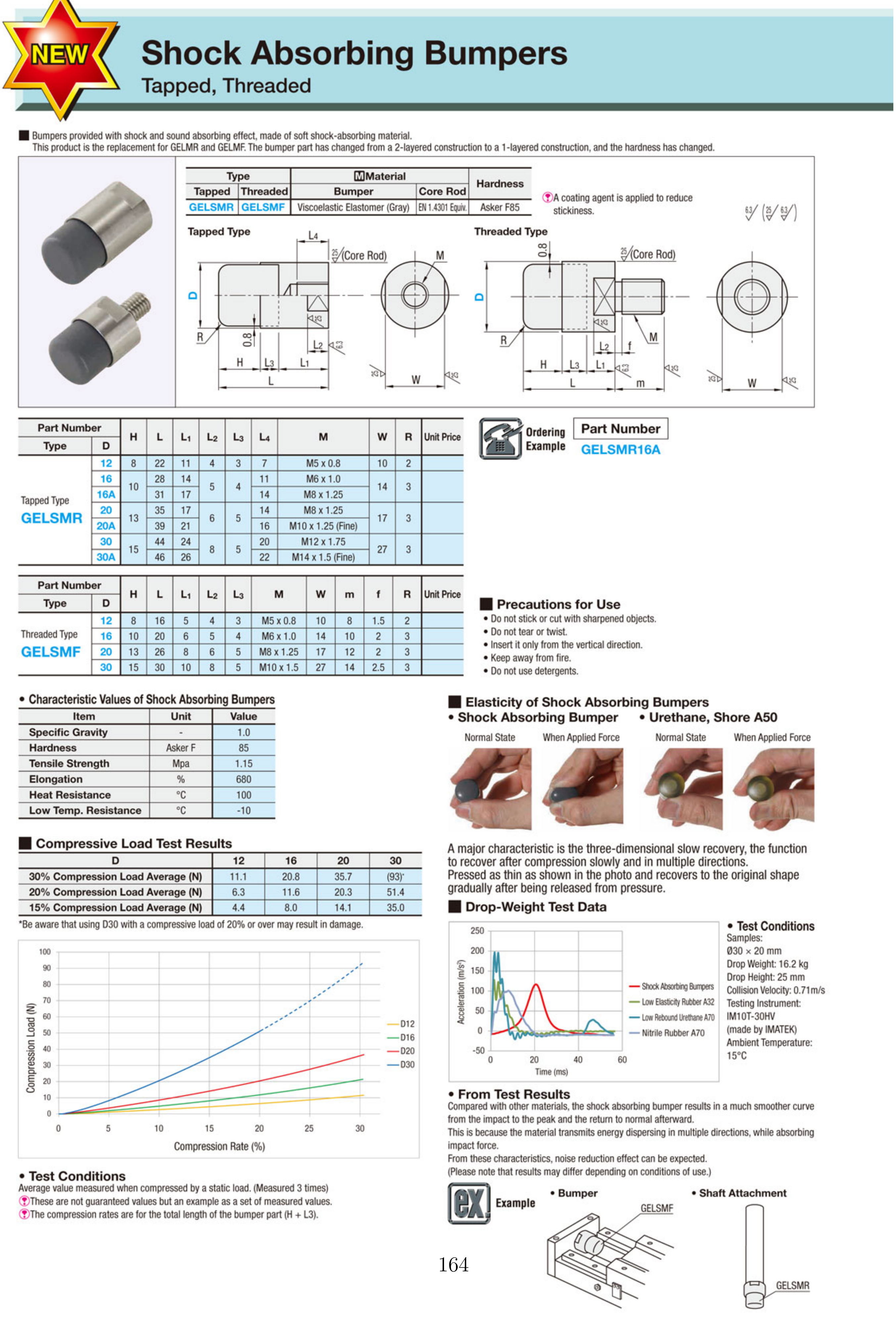

NEW

Shock Absorbing Bumpers

Tapped, Threaded

■ Bumpers provided with shock and sound absorbing effect, made of soft shock-absorbing material.
This product is the replacement for GELMR and GELMF. The bumper part has changed from a 2-layered construction to a 1-layered construction, and the hardness has changed.

Type		Ⓜ Material		Hardness
Tapped	Threaded	Bumper	Core Rod	
GELSMR	GELSMF	Viscoelastic Elastomer (Gray)	EN 1.4301 Equiv.	Asker F85

A coating agent is applied to reduce stickiness.

Tapped Type

Threaded Type

Part Number		H	L	L_1	L_2	L_3	L_4	M	W	R	Unit Price
Type	D										
Tapped Type GELSMR	12	8	22	11	4	3	7	M5 x 0.8	10	2	
	16	10	28	14	5	4	11	M6 x 1.0	14	3	
	16A		31	17			14	M8 x 1.25			
	20	13	35	17	6	5	14	M8 x 1.25	17	3	
	20A		39	21			16	M10 x 1.25 (Fine)			
	30	15	44	24	8	5	20	M12 x 1.75	27	3	
	30A		46	26			22	M14 x 1.5 (Fine)			

Ordering Example

Part Number
GELSMR16A

Part Number		H	L	L_1	L_2	L_3	M	W	m	f	R	Unit Price
Type	D											
Threaded Type GELSMF	12	8	16	5	4	3	M5 x 0.8	10	8	1.5	2	
	16	10	20	6	5	4	M6 x 1.0	14	10	2	3	
	20	13	26	8	6	5	M8 x 1.25	17	12	2	3	
	30	15	30	10	8	5	M10 x 1.5	27	14	2.5	3	

■ Precautions for Use

- Do not stick or cut with sharpened objects.
- Do not tear or twist.
- Insert it only from the vertical direction.
- Keep away from fire.
- Do not use detergents.

• Characteristic Values of Shock Absorbing Bumpers

Item	Unit	Value
Specific Gravity	-	1.0
Hardness	Asker F	85
Tensile Strength	Mpa	1.15
Elongation	%	680
Heat Resistance	°C	100
Low Temp. Resistance	°C	-10

■ Compressive Load Test Results

D	12	16	20	30
30% Compression Load Average (N)	11.1	20.8	35.7	(93)*
20% Compression Load Average (N)	6.3	11.6	20.3	51.4
15% Compression Load Average (N)	4.4	8.0	14.1	35.0

*Be aware that using D30 with a compressive load of 20% or over may result in damage.

• Test Conditions

Average value measured when compressed by a static load. (Measured 3 times)

These are not guaranteed values but an example as a set of measured values.

The compression rates are for the total length of the bumper part (H + L3).

■ Elasticity of Shock Absorbing Bumpers

• Shock Absorbing Bumper **• Urethane, Shore A50**

A major characteristic is the three-dimensional slow recovery, the function to recover after compression slowly and in multiple directions.
Pressed as thin as shown in the photo and recovers to the original shape gradually after being released from pressure.

■ Drop-Weight Test Data

• Test Conditions

Samples:
Ø30 × 20 mm
Drop Weight: 16.2 kg
Drop Height: 25 mm
Collision Velocity: 0.71m/s
Testing Instrument:
IM10T-30HV
(made by IMATEK)
Ambient Temperature:
15°C

• From Test Results

Compared with other materials, the shock absorbing bumper results in a much smoother curve from the impact to the peak and the return to normal afterward.
This is because the material transmits energy dispersing in multiple directions, while absorbing impact force.
From these characteristics, noise reduction effect can be expected.
(Please note that results may differ depending on conditions of use.)

ex Example

• Bumper

• Shaft Attachment

Figure E.1: Data sheet of the bumpers

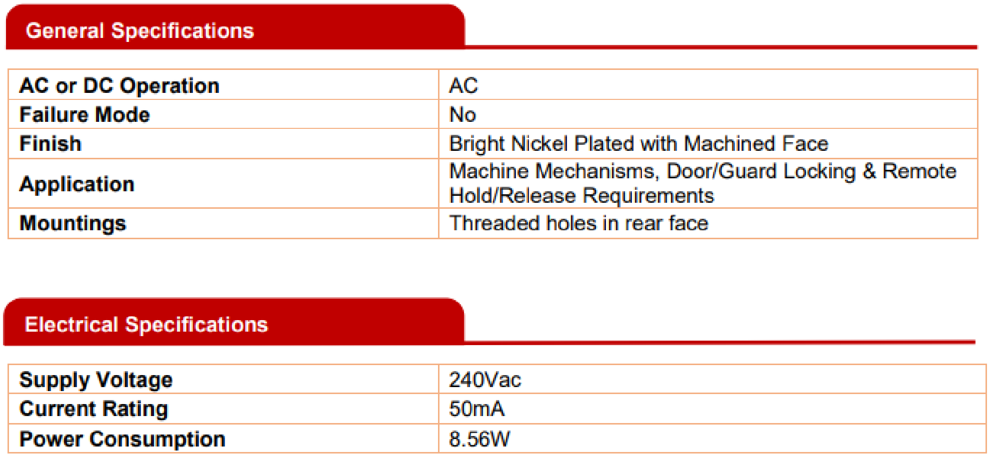

General Specifications

AC or DC Operation	AC
Failure Mode	No
Finish	Bright Nickel Plated with Machined Face
Application	Machine Mechanisms, Door/Guard Locking & Remote Hold/Release Requirements
Mountings	Threaded holes in rear face

Electrical Specifications

Supply Voltage	240Vac
Current Rating	50mA
Power Consumption	8.56W

Figure E.2: Datasheet of the electromagnet (1/2)

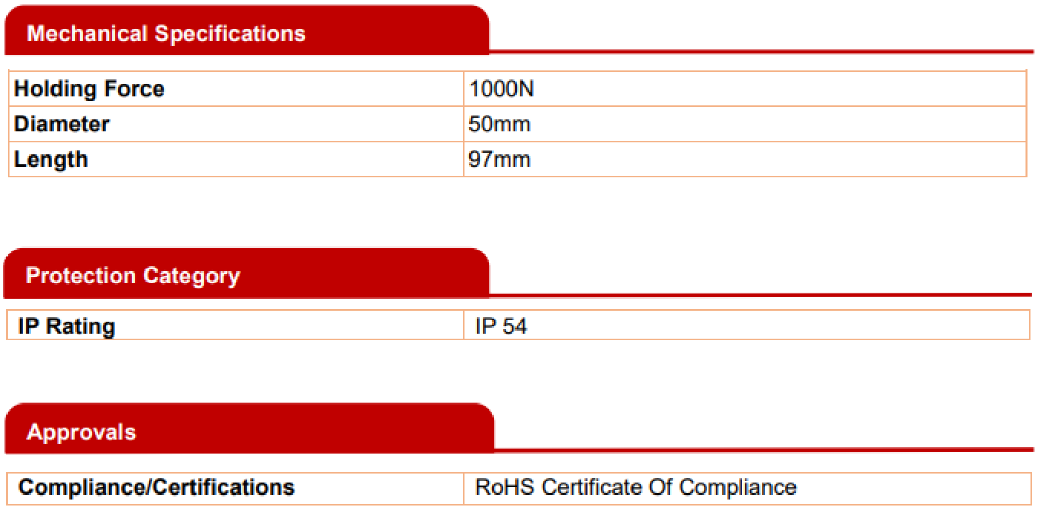

Mechanical Specifications

Holding Force	1000N
Diameter	50mm
Length	97mm

Protection Category

IP Rating	IP 54

Approvals

Compliance/Certifications	RoHS Certificate Of Compliance

Figure E.3: Datasheet of the electromagnet (2/2)

F

Additional illustrations

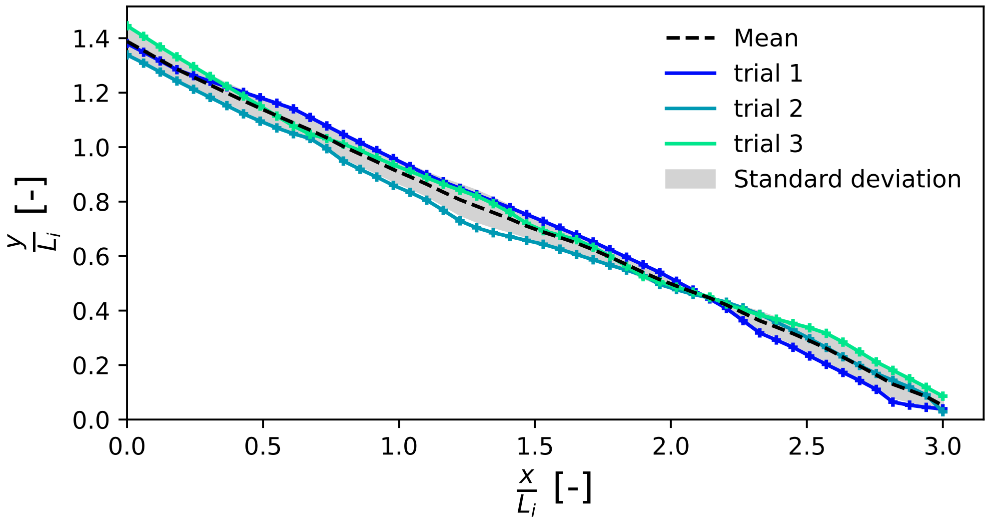

Figure F.1: Plots of the final deposits of the three experiments to illustrate the repeatability of the latter. Initial condition of a = 2, loose column, 0-2mm sand

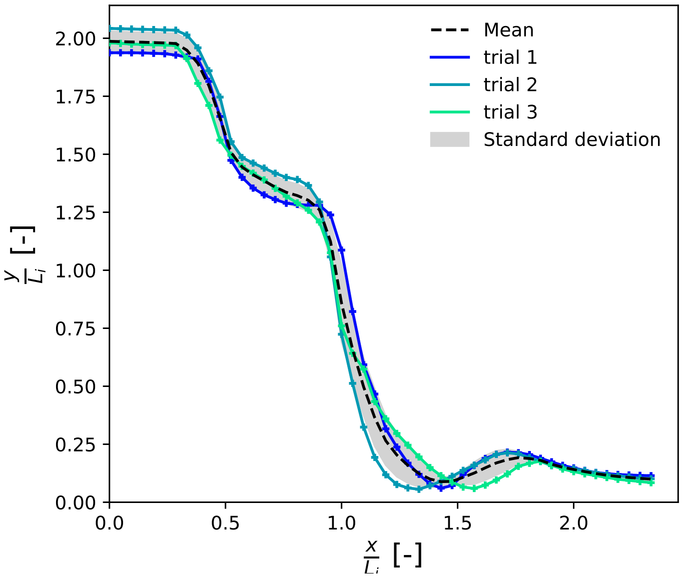

Figure F.2: Plots of the deposits after 3 seconds of the three experiments to illustrate the repeatability of the latter. Initial condition of a = 2, loose column, 0-2mm sand

$$\text{Camera matrix (intrinsic matrix)} = \begin{vmatrix} 1.059\text{e}+04 & 0 & 5.112\text{e}+02 \\ 0 & 1.130\text{e}+04 & 5.146\text{e}+02 \\ 0 & 0 & 1 \end{vmatrix}$$

$$\text{Distortion coefficients} = \begin{vmatrix} -7.957 & 1.500\text{e}+03 & 1.260\text{e-}02 & 5.543\text{e-}02 & 3.825 \end{vmatrix}$$

Table F.1: Camera matrix (intrinsic matrix) and Distortion coefficients obtained with the Calibration method

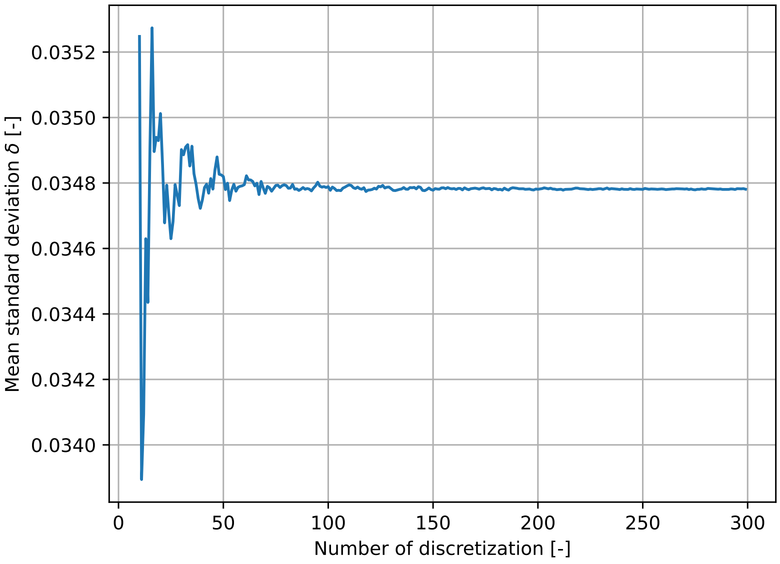

Figure F.3: Study of the convergence of the mean standard deviation of the final deposits to illustrate the repeatability

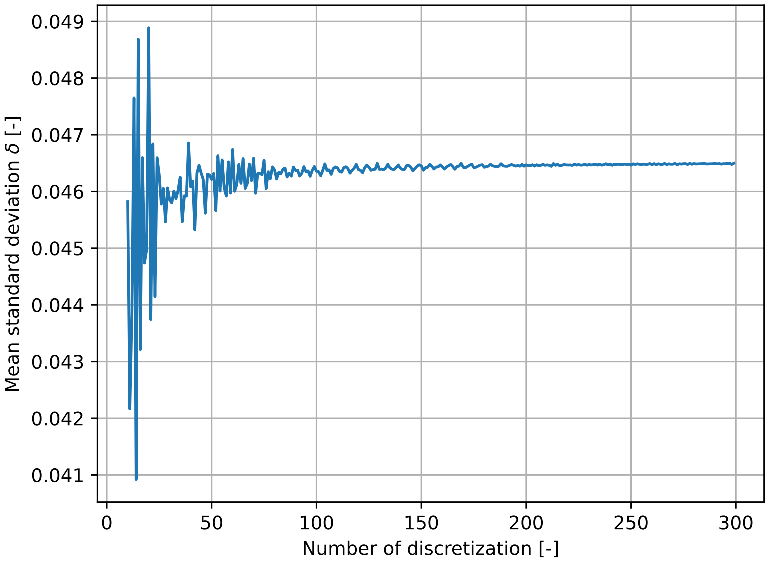

Figure F.4: Study of the convergence of the mean standard deviation o the deposits after 3 seconds to illustrate the repeatability

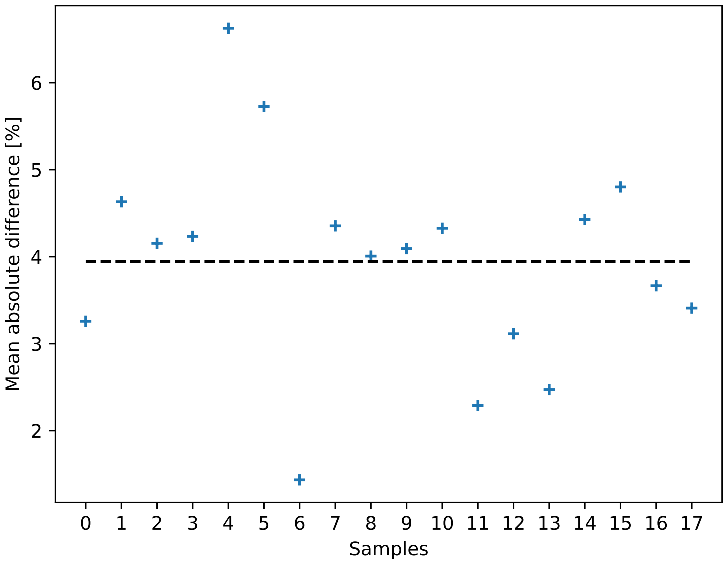

Figure F.5: Study of the mean absolute difference between two images of the calibration with several random samples of images

(a) Global view (b) Roller protection for chip expulsion

Figure F.6: Installation for milling the railway cart bar in the CREDEM laboratory

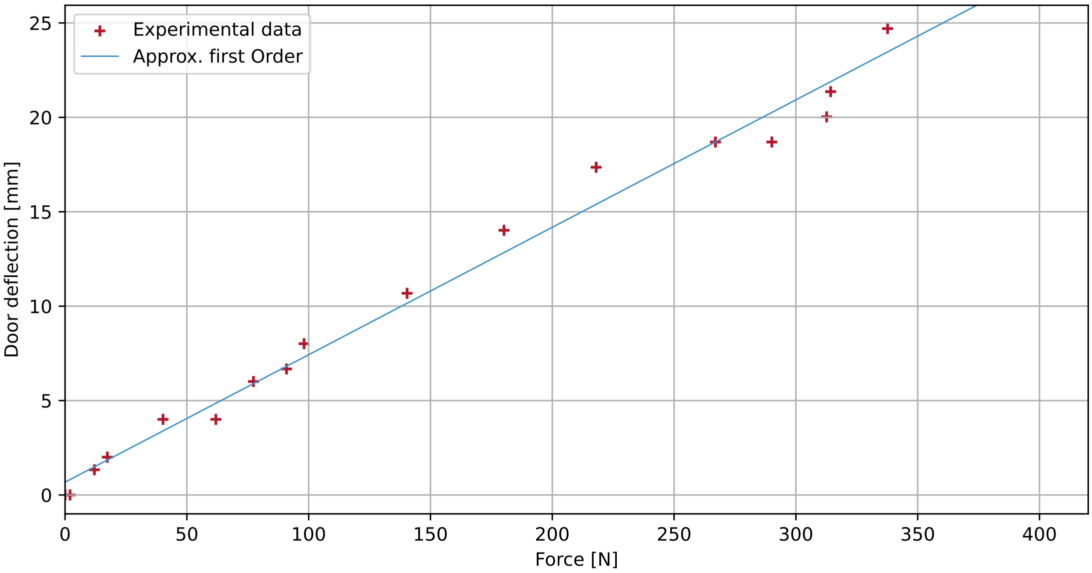

Figure F.7: Experimental observation of the linearly dependence between the force applied on the door and the deflection

G

Detailed experimental procedure

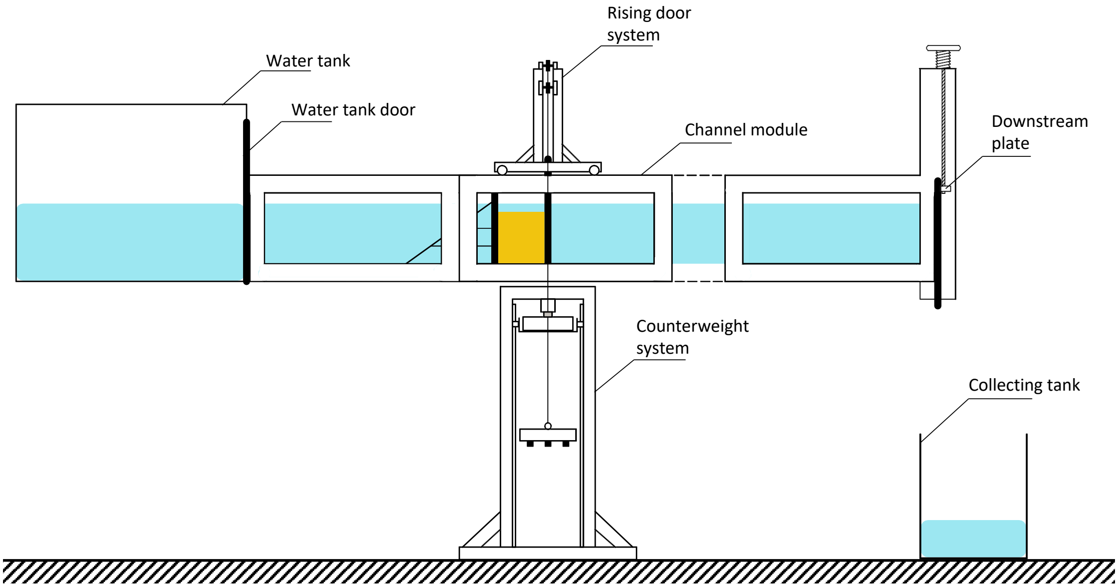

Figure G.1: Experimental setup scheme

1. The downstream plate is raised and rubber strip and waterproof tape are used to seal any leaks.
2. The water tank is filled up using the pump.
3. The water tank door is gently opened to slowly fill up the channel.
4. When the channel is filled up, the water tank door is closed.

5. The sliding door is lowered (To know how the counterweight is re-armed and used see B.4).

6. The back plate is put at the desired sand length L_i and blocked using lead plates and straps.

7. The camera is set in the correct position, facing the channel aligned with the sliding door. It is then plugged and turned on.

8. The sand is poured in the space between the sliding door and the back plate.

9. When the water level is too high, the excess is siphoned. The step 8 is reiterated until the desired sand height H_i is reached.

10. The water level over the sand column is adjusted to have the same as in the rest of the channel.

11. When ready, the recording is started and the sliding door is opened simultaneously by clicking on the software and turning the electromagnet's switch off at the same time.

When the recording is over, the following steps are followed to re-start an experiment :

12. The channel is siphoned.

13. The sand is removed from the channel using a shovel.

14. The back plate is removed.

15. The procedure is re-started at step 3.

H

Digital tools

In an increasingly connected world where digital tools are multiplying by dozen, we felt that it was important to show how we used some of them in the writing methodology of this thesis. Here is an exhaustive list of the digital tools[1] we used with a brief description of how we used them:

- WebPlotDigitilizer (`https://automeris.io/WebPlotDigitizer/`): This web tool allows us to upload images of graphs, often those found in papers. After a few manipulations, it is possible to obtain a list of the exact points on the graphs, making it easier to compare our experimental results with the results of the simulations.

- Research Rabbit (`https://researchrabbitapp.com/home`): It's easy to get lost in the vast number of papers available in the literature. This web tool allows us, by entering the DOI of scientific papers, to discover all the links between the papers by creating a tree structure of their sources. For example, the Figure H.1 shows the tree structure related to 3 papers (in green). This allows us to discover new papers, which have many links between them.

- DeepL (`https://www.deepl.com/fr/translator`): Deepl was the main translator used in this thesis.

- ChatGPT (`https://chat.openai.com/`): English is not our mother tongue, so finding synonyms and various sentence structures was a real challenge. Using it to find synonyms given a particular context is really efficient.

---

[1] excluding software such as Solidworks, Davis 8, PowerPoint, Excel, Jupyter notebook, etc

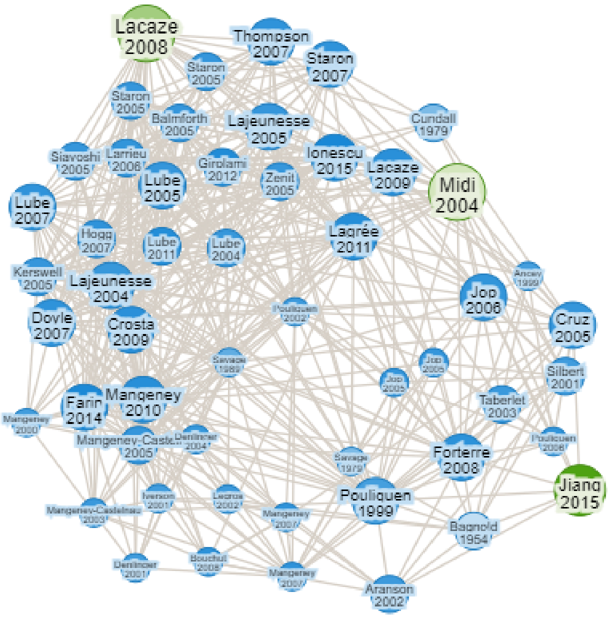

Figure H.1: Example of tree structure obtained through Research Rabbit in order to discover papers

UNIVERSITÉ CATHOLIQUE DE LOUVAIN
École polytechnique de Louvain
Rue Archimède, 1 bte L6.11.01, 1348 Louvain-la-Neuve, Belgique | **www.uclouvain.be/epl**